

Central collisions of Au on Au at 150, 250 and 400 A MeV

W. Reisdorf^a, D. Best^a, A. Gobbi^a, N. Herrmann^{a,j},
 K.D. Hildenbrand^a, B. Hong^a, S.C. Jeong^a, Y. Leifels^a,
 C. Pinkenburg^a, J.L. Ritman^a, D. Schüll^a, U. Sodan^a,
 K. Teh^a, G.S. Wang^a, J.P. Wessels^a, T. Wienold^a, J.P. Alard^b,
 V. Amouroux^b, Z. Basrak^c, N. Bastid^b, I. Belyaev^d,
 L. Berger^b, J. Biegansky^e, M. Bini^f, S. Boussange^b, A. Buta^g,
 R. Čaplar^c, N. Cindro^c, J.P. Coffin^h, P. Crochet^h, R. Dona^h,
 P. Dupieux^b, M. Dželalija^c, J. Eröⁱ, M. Eskef^j, P. Fintz^h,
 Z. Fodorⁱ, L. Fraysse^b, A. Genoux-Lubain^b, G. Goebels^j,
 G. Guillaume^h, Y. Grigorian^k, E. Häfele^j, S. Hölbling^c,
 A. Houari^h, M. Ibnouzahir^b, M. Joriot^b, F. Jundt^h,
 J. Kecskemetiⁱ, M. Kirejczyk^ℓ, P. Konczⁱ, Y. Korchagin^d,
 M. Korolija^c, R. Kotte^e, C. Kuhn^h, D. Lambrecht^b,
 A. Lebedev^d, A. Lebedev^k, I. Legrand^g, C. Maazouzi^h,
 V. Manko^k, T. Matulewicz^ℓ, P.R. Maurenzig^f, H. Merlitz^j,
 G. Mgebrishvili^k, J. Mönsner^e, S. Mohren^j, D. Moisa^g,
 G. Montarou^b, I. Montbel^b, P. Morel^b, W. Neubert^e,
 A. Olmi^f, G. Pasquali^f, D. Pelte^j, M. Petrovici^g, G. Poggi^f,
 P. Pras^b, F. Rami^h, V. Ramillien^b, C. Roy^h, A. Sadchikov^k,
 Z. Seresⁱ, B. Sikora^ℓ, V. Simion^g, K. Siwek-Wilczyńska^ℓ,
 V. Smolyankin^d, N. Taccetti^f, R. Tezkratt^h, L. Tizniti^h,
 M. Trzaska^j, M.A. Vasiliev^k, P. Wagner^h, K. Wisniewski^ℓ
 D. Wohlfarth^e, A. Zhilin^d

FOPI Collaboration

^a*Gesellschaft für Schwerionenforschung, Darmstadt, Germany*

^b*Laboratoire de Physique Corpusculaire, IN2P3/CNRS, and Université Blaise Pascal, Clermont-Ferrand, France*

^c*Rudjer Boskovic Institute, Zagreb, Croatia*

^d*Institute for Theoretical and Experimental Physics, Moscow, Russia*

^e*Forschungszentrum Rossendorf, Dresden, Germany*

^f*I.N.F.N. and University of Florence, Italy*

^g*Institute for Physics and Nuclear Engineering, Bucharest, Romania*

^h*Centre de Recherches Nucléaires and Université Louis Pasteur, Strasbourg,
France*

ⁱ*Central Research Institute for Physics, Budapest, Hungary*

^j*Physikalisches Institut der Universität Heidelberg, Heidelberg, Germany*

^k*Kurchatov Institute, Moscow, Russia*

^l*Institute of Experimental Physics, Warsaw University, Poland*

Abstract

Collisions of Au on Au at incident energies of 150, 250 and 400 A MeV were studied with the FOPI-facility at GSI Darmstadt. Nuclear charge ($Z \leq 15$) and velocity of the products were detected with full azimuthal acceptance at laboratory angles $1^\circ \leq \theta_{lab} \leq 30^\circ$. Isotope separated light charged particles were measured with movable multiple telescopes in an angular range of $6 - 90^\circ$. Central collisions representing about 1% of the reaction cross section were selected by requiring high total transverse energy, but vanishing sideflow. The velocity space distributions and yields of the emitted fragments are reported. The data are analysed in terms of a thermal model including radial flow. A comparison with predictions of the Quantum Molecular Model is presented.

PACS: 25.70.Pq

Key words: NUCLEAR REACTIONS $^{197}\text{Au}(^{197}\text{Au},X)$, $E = 150, 250, 400$ MeV/nucleon; selected central collisions; measured fragment velocity vectors, charges and yields; deduced radial flow, chemical composition; comparison to statistical multifragmentation models, quantum molecular dynamics model

1 Introduction

The properties of hadronic matter under various conditions of density and temperature are of high interest both in their own right and owing to their astrophysical connection: evolution of the early universe and of neutron stars. In earthly laboratories hadronic matter in a state far off its ground state can only be studied in heavy ion collisions at incident energies that are well above the Coulomb barrier. Such studies in the energy regime from about 100 A MeV to 2 A GeV were initiated in the mid 1970's at the Bevalac in Berkeley. It became soon clear that the high multiplicity and diversity of particles emerging from such collisions required sophisticated detection systems covering large angular ranges while having high particle identification power and

high granularity and/or multiple hit capabilities. Due to the large variety of possible event topologies, there was also a need to register and sort a very large number of collisions in order to obtain statistically significant information.

With the advent of 4π particle detectors like the Streamer Chamber [1], the Plastic Ball [2] and, somewhat later, Diogene [3], first dynamic signals of hot expanding nuclear matter were seen in the form of collective flow, i.e. correlated emission patterns involving many particles. Together with studies of the chemical composition of the emitted fragments (single nucleons, clusters, produced mesons) and its possible connection to the entropy of the created hot and compressed matter, and further complemented by space-time evolution studies inferred from two-particle interferometry, great hopes arose that the properties of hadronic matter, namely its equation of state, and possible phase transitions, could be inferred from the data.

The experimental and theoretical situation in the second half of the eighties was summarized in a series of excellent review papers [4–8]. Despite the tremendous progress achieved, it remained clear however that considerable efforts were still needed both experimentally and theoretically to achieve a sufficiently detailed understanding of the highly complex dynamics of these reactions in order to be able to extract the more fundamental issues.

At the beginning of the nineties a new generation of 4π detectors emerged both at the Bevalac and at SIS/ESR, Darmstadt, that had increased particle identification power as well as higher granularity. One of the tasks of these new detector systems is to provide complete triple-differential coverage of the populated momentum space while achieving good particle identification and minimal apparatus distortions.

The detector FOPI, installed at SIS/ESR, is such a system. It was built in two phases: Phase I, covering the forward hemisphere ($1 - 30^\circ$ in the laboratory) and based on time-of-flight plus energy-loss methods to identify and characterize the emerging particles, and Phase II, which extended the detector to 4π geometry and added magnetic analysis. The first major experiment was concerned with Au on Au collisions in the energy range extending from 100 to 800 A MeV. It was performed with the Phase I detectors [9] complemented by movable multiple telescopes [10] that covered also backward angles.

In the present work we show and analyse data on very central collisions limiting ourselves to incident energies of 150, 250 and 400 A MeV. The corresponding center-of-mass (c.o.m.) energies of 37-95 A MeV extend from energies comparable to the nucleonic Fermi energy in ground state nuclei to well above it. As we shall see, cluster formation in this regime is still the rule, rather than the exception. While 'hard' nucleon-nucleon collisions play an increasing role, in addition to the mean field that seems to dominate reactions at lower energies,

by far most of these collisions on a 'microscopic' level are expected to be elastic: The internal nucleon degrees of freedom are still essentially dormant and in particular pion production, although well above measuring sensitivity, does not play an important part in the general balance of energy.

Under these conditions the fact that Phase I was still 'pion-blind' does not represent a serious problem in a study aimed at obtaining a general overview of the triple-differential momentum-space population and the composition of the most abundant particles. The lower energy limitation was governed by the necessity to have sufficient coverage of the mid-rapidity part of phase-space in view of threshold limitations affecting heavier clusters.

Indeed, one of the perhaps surprising outcomes of this investigation of *central* collisions was the still copious production of intermediate-mass fragments that we shall define to be fragments with nuclear charge $Z \geq 3$ and abbreviate as IMF in accordance to established practice in the literature. Processes involving the 'simultaneous' emission of many IMF's have been termed 'multifragmentation' and have found widespread interest, see for instance [11–14].

Older exclusive information on heavy cluster formation from Bevalac times was limited to an experiment at 200 A MeV [15] concentrating on sideflow: a remarkable result of this study was the demonstrated higher sensitivity of the IMF's to flow, a fact that had been anticipated in the framework of hydrodynamical model calculations [16]. Since then, new information from central or semicentral collisions at energies beyond 100 A MeV has emerged from work done both at Berkeley and Darmstadt [17–31].

One of the important new observations, favoured by the sensitivity of IMF's to flow, was the overwhelming and unambiguous evidence of a new kind of axially *symmetric* or 'radial' flow [20–22,26,28] as a signature of highly exclusive central collisions. This flow was far more important in magnitude than the sideflow predicted [32] and discovered [33,34] earlier and was characteristic of *participant* matter, in contrast to the sideflow phenomenon which was primarily interpreted as a spectator phenomenon.

The development of an isotropic 'blast' in energetic collisions had been explicitly proposed by Bondorf *et al.* [35] in the framework of an adiabatic expansion of a hot ideal-gas. This provided one possible mechanism of local cooling that seemed necessary to account for the formation of clusters. A year later, Siemens and Rasmussen [36] first proposed that the data then available gave evidence for a 'blast wave'. Much later, evidence came from emulsion studies [37,38] in which it was first shown that in events with a high degree of sphericity, fragments were emitted that were characterized by an approximately *linear rise of the average kinetic energy with size*. This phenomenon clearly went beyond the expectations of a thermal model [39] based on an equilibrated system

enclosed in a box.

Our collaboration, taking advantage of combined high multiplicity and low directivity event selection, first showed that the heavy clusters indeed were emitted from essentially one source located at midrapidity [17]. Soon after, we came to the conclusion, with use of statistical models, that the occurrence of so many IMF's had to be associated with a surprisingly low entropy [18,23]. The new radial flow phenomenon was then quantized [20] and a first attempt using the model of ref. [35] was made [22] to trace back the initial conditions of compression and temperature from the measured momentum distributions and an approximate account for the chemical composition of the fireball could be done. It also became clear that radial flow was going to have an essential influence on the quantitative interpretation of small relative-momentum correlations between IMF's [24] aimed at determining the size of the fireball at freeze out.

Further work concentrated on the isotope-separated light charged particles ($Z = 1, 2$) [26] and it became evident that the simultaneous understanding of both the chemical composition (light *and* heavy clusters) of the fireball *and* the momentum space distributions of all the observed particles was going to be a special challenge.

The present work concentrates on both of these aspects, presenting the data in more complete detail than before. After a brief reminder of the major features of the Phase I apparatus [9] in section 2 we outline and discuss in section 3 our method for obtaining a highly central sample of events. The aim is to isolate a maximal-size piece of hot nuclear matter with a minimum of contamination by spectator matter. The isolation of these highly central events will then allow us to take a , still qualitative, look at the general topology in momentum space concentrating, among others, on the gradual evolution with incident energy.

Then we explore in sections 4 and 5 the possibility of accounting for the data (momentum space distribution and chemical composition) in the framework of a thermal model, which however, accounts for the presence of radial flow. A preliminary extraction of the radial flow values was reported in refs. [40,41]. This flow considerably diminishes the available chaotic part of the energy. The presence of IMF's allows us to determine the flow profile with higher accuracy than before. An important point will be that the analysis keeps track of the energy and charge balance. After subtraction of the collective, or flow, energy, the remaining chaotic energy is interpreted as thermal energy that is then used in section 5 as input into statistical models to see if chemical composition can be understood in terms of a quasihomogenous population of the locally available phase space. Statistical model descriptions of the data that are *not* constrained by a fixed available thermal energy have been remarkably successful [18] even at much higher energies [42].

The results of these efforts will then bring us to consider the dynamical alternative (section 6) in the framework of the Quantum Molecular Dynamics (QMD) model [43]. In particular we will explore with this model to what degree the generation of transverse momentum results in quasi-isotropic topologies of central events, and we will consider the amount of scaling of radial flow and of sideflow and their possible connection. We will also take a look at the capability of such microscopic models to predict the probability of clusterization and the possible interconnection of the latter with the time scale of the explosion.

A summary of the data and conclusions, together with a brief outlook (section 7) will close this work.

2 Experimental procedure

Au on Au collisions at incident energies ranging from 100 to 800 A MeV were studied with the Phase I of the FOPI detector [9] at the SIS/ESR accelerator facility, GSI Darmstadt. Only the data obtained at 150, 250 and 400 A MeV will be presented here. The beam intensities were typically 10^5 ions/s. Targets of 0.5% (for lower energies) up to 2% (for higher energies) interaction length (i.e. 200 mg/cm²) were used. Most events were registered under 'central trigger' conditions, some under 'minimum bias' conditions. The central trigger consisted in a high multiplicity threshold on the External Wall (PM>16, 17, 21, respectively, at 150, 250 and 400 A MeV) which selected an impact parameter range up to 8.5 ± 0.5 fm in a sharp cutoff model. An average of 10^6 events was collected at each energy under central trigger conditions. Unless otherwise stated only these events will be analysed in the following.

Phase I of the detector covered the laboratory polar angles from 1.2° to 30°. It consists of a Forward Wall of scintillators with a granularity exceeding that of the earlier Plastic Ball experiments [2,8] by roughly a factor three. The Inner Wall consisting of 252 trapezoidal scintillator paddles extends from 1.2° to 7.5°, and the External Wall (512 scintillator bars) covers the angles from 7° to 30°. Each scintillator provides an energy loss and a time-of-flight signal allowing to determine the element number Z and the velocity vector of the charged particles. In order to achieve lower detection thresholds a shell of 188 thin energy loss detectors (cluster detectors) is mounted in front of the Wall. It consists of an ensemble of gas-filled ionization chambers (Parabola) in front of the External Wall and thin plastic scintillator paddles (Rosace) in front of the Inner Wall. A helium bag is placed between the target and the Forward Wall. With this setup charge identification up to $Z=15$ is obtained, with thresholds in the external part of the detector increasing from 14 A MeV for $Z=1$ fragments to 50 A MeV for $Z=15$ fragments. The energy thresholds are slightly higher in the inner part due to larger flight path and larger thickness

of the Rosace paddles in comparison to the Parabola ionization chambers.

In some of the runs the FOPI detector was complemented by 8 multiple Si-CsI(Tl) telescopes [10] which could be moved in the horizontal plane over an angular range from 6° up to 90° . These detectors, operated in coincidence with the FOPI detector, allowed isotope separation for $Z=1$ to 2 and had lower thresholds of 8 A MeV or less. The telescope data have been discussed in an earlier publication [26], but will be included here again in a combined analysis.

The nominal beam energies indicated are understood to be mid-target energies taking into account all energy losses upstream. Likewise, in the following, all momentum space distributions of the observed fragments are corrected for their path and charge dependent energy losses on the way to the detectors. The systematic errors of the measured velocities are estimated to be 1.5 % or 3β %, whichever is larger (β is the velocity in units of the light velocity).

3 Centrality selection and event topologies

3.1 Choosing central events

Using effective sharp radii [44] for Au one can estimate a 'geometrical' cross section of 5850 mb corresponding to a maximal impact parameter $b=13.6$ fm. Ideally, in a central collision, one would like to minimize the contribution of non-overlapping matter. In a clean-cut straight-trajectory model the 'spectator' fraction can be estimated to reach the level of 10% at an impact parameter of 1.4 fm or a cross section of 60 mb which is just about 1% of the total cross section. Because of the very high 'background' of non-central collisions it is clear that global event-observables that are used for the selection of central collisions should not only have a unique *average* correlation with the impact parameter, but also a small *fluctuation* around this average value.

In finite systems such fluctuations are unavoidable. Also, in the present energy regime Fermi velocities remain comparable to the c.o.m. velocity in the incident channel making a clean separation of 'spectators' and 'participants' difficult as we shall see.

Traditionally, high particle multiplicities have been associated with central collisions. Fig. 1 shows charged-particle multiplicity ('PM') distributions measured with the External Wall. In the figure the distributions are cut off at a total cross section level of about 1500 mb (7 fm). With the depicted multiplicity range contamination from non-target background is estimated (from

target-free runs) to be below the 10% level in the worst case and altogether negligible around and beyond the plateau edge (see Fig. 1). Future detailed comparisons with event-simulating models should of course take into account the granularity (see section 2) of the External Wall and the resulting multiple-hit probabilities .

The presence of a plateau (on a logarithmic scale) in these PM distributions allows to define a limiting value at the upper edge of the distribution that is characterized by a yield equal to half the plateau value [8]. In our case the summed cross section beyond this limiting value turns out to be about 250 mb (it varies somewhat with energy) corresponding to 'geometric' cuts of about 3 fm. This still relatively large cross section makes one suspect that the multiplicity fluctuation seen in the tailend of the distribution is rather large limiting the 'resolution' of the associated impact parameter. The other drawback of the selection of events with large multiplicities is the bias this implies concerning the chemical composition of the hot object one wants to study: by requiring high average multiplicities $\langle M \rangle$ one obviously fixes the average size of the emitted clusters which is just $A / \langle M \rangle$ (A is the total mass).

Another alternative to select the most central collisions is to look for events with a maximal transverse energy of the emitted fragments. If one assumes that transverse energy is created predominantly via nucleon-nucleon collisions, the picture is that the number of such collisions is maximal when there is optimal overlap between target and projectile. Since in the present energy regime particle production is modest, the sum of total longitudinal, E_ℓ , and transversal, E_t , kinetic energies is constant by energy conservation and hence in a perfect 4π apparatus any function of E_t and/or E_ℓ is essentially equivalent. Simulations with the Quantum Molecular Dynamics (QMD) model [43] model showed that in our Phase I geometry the ratio, dubbed ERAT, defined by

$$ERAT \equiv \frac{E_t}{E_\ell} \equiv \frac{\sum_i p_{ti}^2 / (m_i + E_i)}{\sum_i p_{\ell i}^2 / (m_i + E_i)} ; \quad (1)$$

is particularly suitable for event sorting [46]. In this definition [45] p_t , p_ℓ are transverse and longitudinal momenta, m is the rest mass, E the total energy (including the rest mass) of a fragment. As we are not measuring masses in Phase I, we replace m_i by $2Z_i m_N$ (Z the nuclear charge, m_N the nucleon mass) when calculating ERAT. The sums are limited to the forward hemisphere in the c.o.m., as the backward hemisphere was not well covered by the Phase I setup. One other advantage of this choice of a dimensionless observable is that it is 'scale invariant' in the sense that it will not vary with incident energy if the event shapes are scale invariant. In a naive physics interpretation and for central collisions one may expect three possible outcomes for ERAT: $ERAT \approx 2$, may be associated with an approximately thermalized fireball.

Values significantly below two tend to indicate transparency, while values well above two signal squeeze out of nuclear matter at 90° due perhaps to shock-like effects as predicted long ago in the framework of hydrodynamical calculations [47,48].

Measured distributions of ERAT (for values larger than 0.3) are shown in Fig. 2. Apparatus limits (see section 2) roughly cut in half the true ERAT value (see also section 6). For these distributions an additional cut on the External Wall multiplicity PM ($> 16, 17, 21$, respectively for $E/A = 150, 250, 400$ MeV) was done. With these thresholds on multiplicity background contributions are virtually eliminated provided $\text{ERAT} > 0.3$. We found that the applied multiplicity cut had no consequence for $\text{ERAT} > 0.5$.

The approximate scaling properties for the ERAT distributions can be judged from the Figure. The statistical errors are smaller than the symbol sizes. We are reluctant to attach physics meaning to the small variations with incident energy as the systematic errors (0.07 units along the ERAT axis beyond the 100 mb level) are estimated to be only slightly smaller than the differences visible in the Figure. We shall come back to ERAT distributions in section 6.

Since our prime aim was to select the most central events, it was desirable to obtain model independent information on how well centrality is achieved when applying various cuts on global observables such as PM or ERAT. In the limit of zero impact parameter the event shapes ought to be axially symmetric on the average.

Using the method of Danielewicz and Odyniec [49] we have determined azimuthal distributions of the IMF. Due to side-flow [33,34] these distributions in general are peaked at an azimuth $\phi = 0$ in the reaction plane if only fragments in the forward hemisphere are considered. The particular sensitivity of heavier fragments to flow phenomena has been anticipated theoretically, see for instance ref. [16,50], and was first observed experimentally in ref. [15]. IMF's are therefore a rather sensitive probe of deviations from centrality. Figure 3 shows azimuthal distributions (limited to forward rapidities and $E/A = 250$ MeV) under various cut thresholds on PM and ERAT. Comparable integrated cross sections (corresponding to effective impact parameters $b=1$ or $2.5\text{-}2.7$ fm), were taken as indicated in the Figure. The data were least-squares fitted using

$$dM/d\phi = a_0(1 + a_1 \cos \phi + a_2 \cos 2\phi) \quad (2)$$

where the parameters are a_0 , a_1 and a_2 and the azimuthal angle is ϕ . With a PM selection one finds quite sizeable azimuthal asymmetries with ratios $R_\phi(0^\circ/180^\circ)$ in excess of five, almost independent on the PM threshold (as long as it is sufficiently high). The R_ϕ ratios are considerably smaller when

an ERAT selection is done and keep decreasing as the ERAT threshold is increased to the statistical limit (see also [51]). These trends remain even when a midrapidity cut is applied in addition, as can be seen in Fig. 4: R_ϕ is saturated at a value of two for all $PM > 43$ while it reaches gradually the nominal value for isotropy when $ERAT \geq 1.0$. In the range shown the integrated cross section varies from 350 mb (3.3 fm) down to 20 mb (0.8 fm). Thus, 'perfect' isotropy is reached only for ERAT selections and at the cost of very severe cuts.

As it is our aim to study the momentum space distribution as well as the chemical composition of the central fireball, a compromise has to be made between the need for good centrality and the minimum number of events required for adequate statistics. Because of finite number fluctuations there is also the worry about statistical noise causing one to look at 'atypical' events. We shall come back later to the severe autocorrelation effects that occur in extreme-cut situations. From the above study we concluded that while ERAT was a better choice than PM to achieve centrality, there was a need for another selection criterion that would allow to 'open up' the severe ERAT cut necessary to achieve azimuthal isotropy. The idea followed was to define global observables that would be a measure of sideflow and to request *small sideflows while maintaining high transverse energies*.

Introducing the scaled four-velocity $u \equiv (\vec{u}, u_4)$ with $\vec{u} = \vec{\beta}\gamma/\beta_p\gamma_p$, where $\vec{\beta}$ is the velocity in units of c , $\gamma = (1 - \beta^2)^{-1/2}$, $u_4 = \gamma/\gamma_p$ and the index p refers to the incident projectile in the c.o.m., we define the directivity [17,52]

$$D = |\sum_i Z_i \vec{u}_{ti}| / \sum_i Z_i |\vec{u}_{ti}| \quad (3)$$

and [49,53]

$$F_{DO} = \sum_{j,i \neq j} Z_i \vec{u}_{ti} Z_j \vec{u}_{tj} / \sum_{j,i \neq j} Z_i Z_j \quad (4)$$

$$p_x^{\text{dir}} = \sum_i Z_i u_{xi} / \sum_i Z_i \quad (5)$$

where \vec{u}_t is the transverse component of \vec{u} and u_{xi} is given by

$$u_{xi} = \vec{u}_{ti} \cdot \vec{Q}_i / |Q_i| \quad (6)$$

with

$$\vec{Q}_i = \sum_{j \neq i} Z_j \vec{u}_{tj} \quad (7)$$

Owing to the Phase I limitations all sums in eqs. 3 to 7 are limited to fragments emitted into the forward hemisphere in the c.o.m. and we use nuclear charges instead of the more commonly used masses. Note that $j \neq i$ in the sums for F_{DO} and \vec{Q}_i . The observable p_x^{dir} is called *mean transverse momentum per nucleon in the reaction plane*, although it is dimensionless in the scaled units used here and, due to the condition $j \neq i$, the vector \vec{Q}_i varies with i . The variables D and F_{DO} do not refer to a reaction plane explicitly. In the absence of side-flow F_{DO} and p_x^{dir} tend to be small and negative due to momentum conservation constraints. The same is true for the *reduced directivity* $D^{(0)} = D - D_{\text{rnd}}$ where the 'random' directivity D_{rnd} is the value of D averaged for the same subset of events but after randomization of the azimuthal emission angles. Typical distributions of D , D_{rnd} and p_x^{dir} for an ERAT-selected event sample corresponding to the most central 200 mb (ERAT200) are shown in the upper panels of Fig. 5. The evolution of the first moments of these distributions with the average value of ERAT or PM within narrow intervals is shown in the lower panels where the abscissa has been converted to the effective impact parameters. One sees that both measures of axial asymmetry (as well as F_{DO} [53], which is not shown) have completely analogue trends: for PM binning they never reach the value of zero, while for ERAT binning a clean maximum is resolved showing that below an effective impact parameter of 4 fm collisions are reached that have increasing axial symmetry as the ERAT value is *raised* and hence are interpreted as being more central.

As all measures of sideflow were seen to be largely equivalent for our purpose, we opted to combine ERAT with the D cut. Note that D , again, is a scale invariant quantity in particular when the multiplicity dependent average random value is subtracted. The threshold value of D was determined empirically, see Fig. 6, by taking the ERAT200 sample and gradually lowering the upper limit of accepted events while controlling the azimuthal ratio R_ϕ of the IMF. These event samples will be dubbed ERAT200D in the following. In order to assess the dependence of the results on the selection scheme an alternate sample ERAT50 with approximately 50 mb, but without directivity selection, was also considered in the analyses to be described in the sequel. Occasionally we shall compare also with PM selected samples. A summary of the specifications of all these event selections is given in table 1. While the indicated cross sections are quite accurate on a relative basis, they share an estimated common systematic uncertainty of about 10%.

Before presenting data under specific selection criteria it is useful to make a few remarks on the possibility of bias when choosing events in the tails of distributions of global observables. Even such a heavy system as Au on Au is subjected to trivial finite-number fluctuations that sit on top of potentially interesting 'physics' fluctuations. An idea of the magnitude of such fluctuations for the observable ERAT, obtained only from charged particles, but in 4π geometry, is given in fig. 7 which shows the result of central event simulations

with three different models. Only two of the models will be discussed here, the third one will be picked up in section 6. The histogram in the figure is an isotropic blast model simulation (that will be described in detail in section 4.1), which by definition predicts an average ERAT value of two. In each event the model conserves energy, momentum, mass and charge. Except for this constraint it is assumed that the multiplicities of the different species (taken from experiment) fluctuate in an uncorrelated way. Similar assumptions have been used with success in ref. [54].

The resulting, *purely statistical*, fluctuation of ERAT around the value of two is considerable. As this fluctuation is unavoidable in finite systems, it should not come as a surprise that a simulation with a Quantum Molecular Dynamics [43] code IQMD, [55,56], to be described in section 6, comes out to be indistinguishable (see fig. 7). Here we choose an energy (250 A MeV) and parameterization that happens to give also an average ERAT value of two. In principle QMD also allows for non-trivial fluctuations, but the finite-number fluctuations are dominating.

If one were to put an event selection cut in figure 7 at very low (or very high) ERAT values, that are significantly different from the average value, one would sample events that are *not* isotropic, but fluctuate between prolate and oblate shapes. High ERAT values for example indicate a surplus of transverse momenta and hence preferred emission perpendicular to the beam axis. By far the simplest way to distinguish if the high ERAT values represent a *collective*, i.e. correlated fluctuation, or a trivial, uncorrelated one, is to always exclude the so-called Particle Of Interest (POI) from the trigger condition. Loosely speaking: if out of 50 particles, 49 are going left, then if the move is *collective*, the last particle, our POI, will do so also with a large probability. If the move was an uncorrelated fluctuation, the POI will be uninfluenced by the random fluctuation of the other particles.

From an extensive series of test simulations we learned that failure to use this simple recipe will, in the tails of global distributions, lead to severe autocorrelation effects, that distort the true distributions. We found, as intuitively obvious, that such autocorrelation effects were rising with the deviation of the sampled events from the average event and with $Z_{\text{POI}}/Z_{\text{sum}}$, i.e. the ratio of the charge of the POI to the sum of charges contributing to the global observable. Therefore, in the sequel, we have always excluded the POI from the cut condition.

In many ways the procedure is the same as the well accepted procedure of eliminating the POI from the reaction plane determination, see our eq. 7. The removal of *one* particle from a global observable (which in practice is not measured with *all* particles anyhow) does not significantly change the binning property of this observable. If out of n particles of interest in a given event

$m \leq n$ have been selected, the event is accepted with a probability m/n . This still allows to determine cross sections for certain cuts. The deviation from the yes/no logic of sharp cuts is not considered a serious problem.

3.2 Topologies of central events

Resuming now our investigation of highly central events, it is revealing to take a look at the variation of the event topology in the two-dimensional space of transverse 4-velocity and rapidity. In the following we shall make use of scaled quantities: in particular rapidities, y , are defined in the c.o.m. system and divided by the beam rapidity, and we recall that the transverse four-velocities, u_t are scaled with the $\beta\gamma$ value of the projectile in the c.o.m.. In this system of units target (projectile) rapidity is at -1 ($+1$). Scaling properties expected in the hydrodynamics context will be discussed briefly in section 6.2.

We start with Fig. 8 which shows contour plots for the invariant cross sections $d^2\sigma/u_t du_t dy$ of $Z=4$ fragments under the cuts PM200, ERAT200 and ERAT200D. In the non-relativistic limit, and with the scaling just mentioned, events which are isotropic on the average, should lead to circular contours. A remarkable variation of the topology is revealed: The sizeable 'spectator' contributions in the PM200 sample have disappeared when ERAT selections are made, the directivity cut leads to manifestly more compact configurations on the rapidity axis [17]. For the selection ERAT200D there is no question that these fragments are predominantly emitted from a source centered at midrapidity confirming our earlier findings [17]. Although near-isotropy in the *polar* angles is reached (see also section 4, the ERAT200D *azimuthal* distributions are isotropic by selection), the contours reveal remarkable structural deviations that one could associate to 'bounced-off' particles [50]. It is clear that finite number fluctuations, corona effects, and the need for a finite sample to achieve statistical significance, are preventing the isolation of a 'pure' fireball even if it exists.

Is the near-isotropy reached for all energies? For the cuts, ERAT200D, we compare the topologies for $Z=3$ fragments at the three studied energies in Fig. 9: for this particular charge one sees an evolution towards more prolate distributions as the incident energy is lowered, indicating either more 'transparency' at these lower energies or a higher difficulty, despite the same selection procedure, to isolate 'truly central' collisions. This sort of ambiguity is difficult to remove in a convincing way. Naively, one expects that Pauli blocking might severely limit the stopping power at energies increasingly close to nucleonic Fermi energies. On the other hand, one might also expect a highly increased 'cross-talk' between initially overlapping parts and 'spectator' parts of the two nuclei since the Fermi velocity is comparable to the incident-beam velocity.

The increasing 'spectator'-'participant' separation is shown in Fig. 10, where the topologies are compared using the selection PM200. At the lower energy, besides the obvious lack of separation of 'sources' the reader should also notice more subtle effects, such as the shift of the 'spectator' parts away from their 'nominal' positions at $y = \pm 1$. This could be a faint remnant of dissipative effects known from many studies of deep-inelastic heavy-ion collisions [57] at near barrier energies all the way up to 30 A MeV [58,59]. In this case important fractions of the dinuclear system are *collectively* decelerated. Special one-body dynamics [60,61], valid when two-body scatterings are Pauli-blocked, has been made responsible for such phenomena.

4 Velocity distributions and the blast model

It is our stated aim to explore to what degree a thermal model is able to account for the data, taking into account the presence of flow. We shall proceed in two steps:

- a) extract the collective part of the available energy by a flow-analysis of the measured momentum-space distributions and interpret the remaining energy as thermal energy;
- b) use this thermal energy as input to statistical model assumptions. Task a) will be accomplished in the present section, task b) is reserved to section 5. In accomplishing task a) we shall make three important simplifying assumptions:

- (1) we shall assume the flow is isotropic,
- (2) we shall allow for only a single local temperature T
- (3) we shall assume the whole system (i.e. two Au nuclei) can be described in this way

Let us briefly comment on these 'naive' assumptions:

- 1) clearly the ERAT200D topologies shown in fig. 9 do not represent a perfectly isotropic fireball. The introduction of more complex ideas, namely the introduction of anisotropic flow patterns, would introduce additional parameters. As we shall see the deviations of the model fits to the data are typically on the 20% level, a modest inaccuracy in the framework of a phase-space model and our present ambitions.
- 2) The introduction of a single local temperature is of importance if one wants to extract flow *phenomenologically* from the data. This assumption leads to the key equation for isotropic blasts (neglecting relativistic corrections)

$$\langle E_{\text{kin}} \rangle = a + b \cdot A_f \quad (8)$$

which states that the average kinetic energies of fragments with mass A_f grows linearly with mass, in contrast to purely thermal models where it would

be constant. Equation (8) holds for *any* flow profile, as long as this profile is common to all fragments. The constant b is the flow per nucleon, which is thus seen to be determined unambiguously (within the model, of course) provided $\langle E_{\text{kin}} \rangle$ has been measured for a sufficiently large range of fragment masses with sufficient accuracy. The mass lever is the only lever that can determine radial flow. Of course flow profiles can influence the *shapes* of the spectra which therefore can be used as testing ground providing additional information on the flow mechanism. The limitation to one local temperature makes sense only if the freeze-out of multinucleon clusters, which are our prime interest here, is fast on the typical expansion time scale. As we shall see, in the central event samples considered here there is no compelling reason to introduce complex temperature profiles. Also, our analysis in the framework of a self-similar adiabatic expansion of a hot and initially compressed ideal gas, with parameters constrained by our data, ended up with modest local variations of the final temperature of the clusterized matter in the bulk region [22]. If the basic one-temperature assumption should prove untenable from *experimental* observations, then we share the caveats expressed in [62] on the possibility to determine flow and temperature in a model-independent way just from the particle spectra.

3) The assumption that the whole system is participant removes any excuses to neglect energy and mass balance and is therefore a powerful constraint. Such an assumption is meaningful only if surface losses on the way to 'equilibrium freeze-out' are sufficiently small, say 20% or less. Experimentally, one can investigate this possibility by varying the volume/surface ratio, i.e. by varying the size of the heavy ion system. Such experiments are on the way. The thermal model would be inadequate if 'preequilibrium' losses were to be a large fraction of the system.

Here we shall mention that an alternative treatment of our data in ref. [63,64] in the framework of a hybrid model, combining a transport theoretical model with a statistical model came to the conclusion that two thirds of the nucleons (in a collision at 250 A MeV) had escaped prior to equilibrium removing more than their share of the available energy and leaving a relatively cold remnant. The decay of this small remnant was then treated with the statistical model. The authors were able to reproduce the *slope* of the measured nuclear charge distribution, but were off by a factor of three in the overall absolute yields (our data were misrepresented by a factor three in ref. [63], see erratum [64]). The fate of the two thirds of preequilibrium nucleons was left open.

Tractable ways to handle preequilibrium are being explored [66]. In section 6 we will use a model [43] that does not require (even local) equilibrium.

4.1 The blast model implementation

As outlined before, we shall assume that at times close to freeze-out (i.e. free streaming) the dynamics has evolved to a situation which can be described approximately by an isotropically expanding system with a local temperature T . Following Cooper and Frye [65] we write for the invariant single particle distribution in momentum space

$$E \frac{d^3 N}{d^3 p} = \int_{\sigma} f(x, p) p^{\mu} d\sigma_{\mu} \quad (9)$$

where p^{μ} is the four-momentum, E the energy including the rest mass, $d\sigma_{\mu}$ is an element of the 3-surface σ and $f(x, p)$ is a Lorentz-invariant distribution-function. For a fixed time t_l ($dt_l = 0$) in the local, comoving frame we can write $d\sigma_{\mu} \equiv (d^3 x_l, \vec{0})$ and

$$E \frac{d^3 N}{d^3 p} = \int_{\sigma} f_l(x_l, p_l) E_l d^3 x_l \quad (10)$$

where the index l holds for the local frame and where we can switch to the center-of-mass (c.o.m.) frame by Lorentz-boost

$$E_l = \gamma_f (E - \vec{\beta}_f \vec{p}) \quad (11)$$

$$d^3 x_l = d^3 x / \gamma_f \quad (12)$$

β_f is the flow velocity which in general will depend on the location, $\gamma^{-2} = 1 - \beta^2$, and \vec{p} is the 3-momentum. Equation (12) follows from the fixed-time condition [65].

In the thermal limit an invariant particle number density $n_l(x_l) = n(x)$ can be defined. Using the approximation of classical statistics we write

$$f_l(x_l, p_l) = N_o \frac{g}{(2\pi)^3} e^{\mu/T} n(r) e^{-E_l/T} \quad (13)$$

where N_o is a normalization constant, g the spin degeneracy and μ the chemical potential. We allow the particle number density to vary with the radial distance r from the center-of-mass of the total system. If we assume that there is a unique flow-velocity versus position correlation $\beta_f(r)$ at any fixed time, then we can take r to be the inverted function $r(\beta_f)$ of $\beta_f(r)$ and hence define a flow density $n_f(\beta_f)$ by the condition

$$n(r) r^2 dr \equiv n_f(\beta_f) \beta_f^2 d\beta_f \quad (14)$$

Assuming that freeze out is fast on the typical expansion time scale, then passing from the local frames to the c.o.m. frame and integrating over angles one obtains for the velocity distribution ($u \equiv \beta\gamma$)

$$\frac{dN}{d\beta} = \frac{4\pi m}{TK_2(m/T)} \gamma^3 u^2 \int \exp^{-\frac{\gamma_f E}{T}} \left[\left(\frac{T}{E} + \gamma_f \right) \frac{\sinh \alpha}{\alpha} - \frac{T}{E} \cosh \alpha \right] n_f(\beta_f) \beta_f^2 d\beta_f / \gamma_f \quad (15)$$

K_2 is the modified Bessel function of order 2 and $\alpha = muu_f/T$, ($u_f = \gamma_f \beta_f$). As we will be using $dN/d\beta$ as a probability distribution for the *shapes* of spectra (see later) we have also given the proper normalization constants, which imply that the integration of eq. (14) over r , resp. β_f , gives unity as well, i.e. $n(r)$ and $n(\beta_f)$ are also redefined as probability densities. (We recall that *absolute* yields are analysed in section 5.)

Eq. (15) can be converted to dN/dE_k by considering that the kinetic energy E_k is given by $E_k = m(\gamma - 1)$ and $dE_k = dE = m\beta\gamma^3 d\beta$. For the limit case where all particles are on a shell sharing a single flow velocity one finds

$$dN/dE_k = \frac{pE}{m^2 TK_2(m/T)} \exp\left(-\frac{\gamma_f E}{T}\right) \left[\left(\frac{T}{E} + \gamma_f \right) \frac{\sinh \alpha}{\alpha} - \frac{T}{E} \cosh \alpha \right] \quad (16)$$

This Ansatz was used in ref. [36] and also by the EOS Collaboration [28] to analyse their data. We shall call this 'Shell' or 'Bubble' scenario in the following.

In our attempts to reproduce the data we have used besides this single-velocity formula the following options:

- $n_f(\beta_f) = n_o$ for $\beta_f \leq \beta_{fo}$ and zero otherwise, giving a box-shaped profile and hence called 'Box' scenario (this Ansatz was used in [26,45]).
- $n_f(\beta_f)$ is a Woods-Saxon distribution with size parameter β_{fo} , relative diffuseness $a_f = 0.1$ and a cutoff at $\beta_f = \beta_{fo}(1 + 2a_f)$ (called scenario WS1)
- as before but with double the diffuseness $a_f = 0.2$ (scenario WS2).

Although we want to put constraints on the flow density profile from our data, no attempt was made to find the 'best possible' profile, as the neglect of evaporative influences on the spectral shapes (see later) make such an attempt premature at the current stage of our analysis. As we shall see, there is also a fundamental limitation to the 'resolution' of such profile shapes due to the thermal convolution.

In general there is no simple relation between the particle number density and the flow profile densities as this must depend on the details of the dynamic

evolution. The formulation eq.(15) has the advantage of expressing final velocity distributions in a form that is amenable for analysis of experimental distributions. It is tempting however to interpret the shape of the flow profile *at freeze out* with the help of the scaling relation

$$\beta_f = rH \quad (17)$$

where H is a 'nuclear Hubble constant'. The analogy (and also the differences) of this 'red-shift' scenario with the expansion of the universe in the Big Bang model has been discussed by Mekjian [39]. It is interesting to note that microscopic transport model calculations in the present energy domain [45,62] also lead to almost linear dependence of the flow velocity on the distance towards the end of the evolution. Trivially, for sufficiently long times of 'free-streaming', relation (17) will always be valid asymptotically as the expanding system has moved to distances large compared to radii at which frequent hard collisions are still taking place. A linear relation between velocity and position *at all times* in the dynamic evolution (not just at or after freeze-out) is the characteristic of a class of 'self-similar' solutions to the ideal-gas hydrodynamics [67] which were introduced into the nuclear context in [35] and applied to some of our data in an earlier publication [22]. Finally, it should be mentioned that such scaling can also be justified in *collisionless* (repulsive) mean-field expansions.

It should be clear, however, that the validity of equation (17) is not essential for our present analysis. In particular, we are not trying here to backtrace from the freeze-out configuration to earlier times of maximum compression and minimal or zero flow. We refer the reader to [22] for instructive results obtained from an analysis of our data at 250 A MeV in terms of self-similar expansion dynamics.

Our object was to determine the collective (flow) energy $\mathcal{E}_{\text{coll}}$ from the measured charge-separated spectra. Energy conservation requires that

$$\mathcal{E}_{\text{coll}} + \mathcal{E}_{\text{th}} = E_{\text{cm}} + Q_{\text{val}} \quad (18)$$

where E_{cm} is the center-of-mass energy in the incident channel, Q_{val} is the Q-value of the reaction and \mathcal{E}_{th} is the thermal energy.

Once the velocity profile (Shell, Box, WS1, WS2) is fixed, the collective part of the spectra is determined by a single scaling parameter β_{fo} . Because of Eq. (18) the thermal part is then fixed as well. For the calculation of the spectral shapes using Eq. (15) we then still need the temperature T . However, T is fixed if we use classical statistics: T is determined by the multiplicity M of all emitted particles (finite-number fluctuations are discussed later). In the

non-relativistic limit we have

$$\mathcal{E}_{\text{th}} = \frac{3}{2}MT \quad (19)$$

Here we have ignored the internal excitation energies of the final observed fragments. The temperature from eq. (19) is 'effective' in the sense that it is not the temperature at freeze-out time, since the observed multiplicity has been raised due to late particle decays. Eq. (19) has however the virtue of being compatible with energy conservation and will only be used for the 'chaotic' part of the spectral shapes. Later in section 5 we fix the thermal *energy* not the temperature to calculate fragment yields. Statistical evaporation does not change on the average the local flow velocity as it must obey momentum conservation in the c.o.m. of the decaying particle, hence the separation into a flow term and a specific local term is not affected. Or expressed more simply: *statistical particle emission does not create flow*. However the resulting spectra, although still 'chaotic' (in the sense that the details of the evaporative processes are not resolved) are no longer thermal in the strict sense. They could have some structural mass dependences, in contrast to true thermal spectra. It is assumed here that this dependence is unsystematic and hence can be ignored in a first approximation. Close inspection of the actual particle spectra (section 4.2.3) will help to assess this simplification.

The multiplicity M in eq. (19) is obtained as follows: Neglecting pion production the neutron multiplicity M_n is calculated using

$$M_n = 236 - (M_d + M_h) - 2(M_t + M_\alpha) - \sum_{Z=3}^{12} ZM_z \quad (20)$$

where 236 is the total number of neutrons available in the double-gold system and where one uses the measured multiplicities M_z (for fragments with nuclear charge Z), M_t (for tritons), M_d (for deuterons), M_α (for ^4He) and M_h (for ^3He). Eq. 20 implies that each IMF ($Z=3-12$, yields with $Z > 12$ are negligible for central collisions at these energies), carries as many neutrons as protons. The yields of H and He isotopes were measured [26] only at 150 and 250 A MeV. For the 400 A MeV data, where the charges but not the isotopes were separated, we assumed that the H isotope ratios were the same as at 250 A MeV, while the $^3\text{He}/^4\text{He}$ ratio was extrapolated to be 0.78 from a linear fit of the measured energy dependence at 100-250 A MeV.

We have determined the ratio $\mathcal{E}_{\text{coll}}/\mathcal{E}_{\text{th}}$ with the constraints of eqs. (18) and (19) by use of a maximum-likelihood method which was applied either to single events or to groups of N events assembled together to form one 'macro'event. N could be any number, usually between 1 and 400. Geometrical and threshold

limits, which could cause a bias, were taken into account in the following way: we maximize the logarithm of the likelihood $\mathcal{L}(\beta_{f0})$ defined by

$$\mathcal{L} = \prod_i f_i/N_i \quad (21)$$

where the product is over all, or alternatively a subset of, the registered particles i in a single, resp. a macroevent and

$$\begin{aligned} f_i &= (dN/d\beta)_i && \text{within detector acceptance} \\ &= 0 && \text{outside detector acceptance} \end{aligned}$$

N_i is given by the normalization condition

$$\int f_i/N_i d\beta = 1 \quad (22)$$

$(dN/d\beta)_i$ is given by eq. (15) and is different for each mass, but averages over dependencies on polar angle. Since we resolved the charges, rather than the masses, we assumed $A = 2Z$.

As the detector acceptance depends on nuclear charge (thresholds) and laboratory angle θ_{lab} (angular cuts, shadows) we have the dependence $N_i = N_i(Z, \theta_{\text{lab}})$. In order to ease the calculation of the normalization constants, we have applied to the data a 'clean-cut' filter consisting of three types of cuts:

- (1) angular cuts: only fragments between $\theta_{\text{lab}} = 1.2^\circ - 30^\circ$, but not within the partially shadowed angles $5^\circ - 7.5^\circ$ and $19^\circ - 21.5^\circ$ were accepted for the fit.
- (2) For the External Wall ($\theta_{\text{lab}} > 7.5^\circ$) the thresholds and other efficiency cuts were replaced by (conservative) c.o.m. angle cuts, $\theta_{\text{cm}} > \theta_{\text{cm}}^{\text{EW}}$, given in Table 2
- (3) For the Internal Wall Z-dependent rapidity cuts were done, $y_{\text{lab}}(Z) > y_{\text{lab}}^{\text{IW}}$, that are also given in the table.

This clean-cut filter is more restrictive than the usual PHASE I filter [68] adopted by our Collaboration for filtering theoretical data prior to comparison with our results.

Technically, the collectivity is varied in steps of 10% using pre-stored functions and calculating $N_i(Z_i, \theta_i)$ numerically. For the final result a quadratic interpolation is done. To check the procedure, 'theoretical' blast events, after filtering, were also fed into the analysis instead of the experimental events and it was found that the original blast parameters were recovered despite the apparatus influences. Under the condition that most events have a sufficient

number of particles with different mass, the fitting procedure converges very fast: event-wise fluctuations of apparent collectivity were about 25% and the fluctuation in a 'macro'event diminished roughly with the square-root of the assembled number of events. The method therefore allows in principle to be extremely selective in the choice of the event sample. As a curiosity let us add: in a perfect 4π detector that would measure and correctly identify all particles, including neutrons, just ten events would be sufficient to fit the radial flow with an accuracy of 5% in the energy regime considered here.

Instead of equation (19) which implies a mass-independent thermal energy of $3/2T$ for each emitted fragment, we actually use the relativistically correct (but still classical) formula

$$\mathcal{E}_{\text{th}} = \sum_i 3T + m_i(K_1(x_i) - K_2(x_i))/K_2(x_i) \quad (23)$$

where K_n are modified Bessel functions of argument $x_i = m_i/T$. For a fixed value of the total thermal energy \mathcal{E}_{th} one has to determine T selfconsistently by using the mass-dependent multiplicities extrapolated to 4π . As the extrapolation depends in turn on the fitted scenario, the procedure requires iterations. Only one iteration was necessary as the relativistic corrections on the thermal energies remain modest in the present energy range.

As the velocity profile is 'folded' with the temperature its precise shape is not resolved, however the 'resolving power' increases with the mass of the observed fragment. This resolving power is demonstrated in Fig. 11. The panels show 'blast' spectra for a scenario at 250 A MeV with an assumed 50/50 ratio of $\mathcal{E}_{\text{coll}}/\mathcal{E}_{\text{th}}$ in scaled units. The mass distribution was taken from experiment. The panels demonstrate three major points:

- while the fully integrated rapidity spectra for mass $A = 8$ shows noticeably flatter tops for the single-velocity scenario 'Shell' than the more complex velocity profiles 'Box' and 'WS2', the difference turns dramatic when one applies in addition a cut on the scaled transverse four-velocity ($u_t < 0.6$) : the upper left panel shows how a 'bubble' ('Shell' scenario) configuration is influencing the rapidity spectrum;
- the same drawing for mass $A = 1$ shows practically no difference between the various scenarios: extracting details of the blast profile is therefore close to impossible with single nucleons (and a fortiori kaons or pions);
- a very large sensitivity is also found in the transverse four-velocity spectra if a rapidity cut ($|y| < 0.5$) is performed; our Phase I apparatus limit ($u_t < 0.6$ at 90° in the c.o.m.) is high enough to judge if the 'Bubble' hole of the 'Shell' scenario exists. Since the blast scenario is isotropic the approximate equivalence between panels a and d in Fig. 11 is expected, but real data may not have this symmetry.

4.2 *Experimental data and the blast model*

A summary of the flow characteristics deduced from the blast model analysis is given in Table 3. One of the main results is that $(62 \pm 8)\%$ of the available energy is stored into radial flow. This value is significantly larger than the values recently published by the EOS collaboration [28], but not too far from our earlier, more preliminary analyses [40,41] and in line with, although somewhat larger than values from analyses reported in [20–22]. The associated average flow velocity $\langle \beta_f \rangle$ is also given in the Table.

In the following we shall present a sample of our data and use the blast model fits as reference. We recall that once the velocity profile is fixed the fit has only one free parameter for the description of the spectral shapes of all the fragments. The absolute yields will be treated in section 5. It is clear that we cannot present the full richness of the data and we point out that other sectors of the data can be made available on request. If not otherwise specified, we compare with the data obtained using the ERAT plus directivity selection, ERAT200D, defined in section 3 and use scaled units. Since FOPI was not a full 4π detector at the time of this experiment, we have chosen some cuts in phase space (outlined in the following sections) which we believe to be minimally distorted by apparatus effects, aside of course for the well defined geometrical limits. Further theoretical efforts to understand these data in more fundamental detail as we claim here should therefore be minimally plagued by obscure ‘apparatus effects’. We remind that the ‘third dimension’ is averaged out in these data, but as discussed earlier, due to the high centrality selection, and in particular the directivity cut, azimuthal variations are reasonably small.

As the (unmeasured) mass fluctuation of the hydrogen fragments is, relatively speaking, large, these fragments are not very useful in our special fitting context. Excluding the hydrogen fragments from the fit generally lead to a better description of the other spectra and increased the deduced collectivity at 150 and 250 A MeV by about 10 %. This is due to the fact that the average mass of $Z=1$ isotopes is somewhat lower [26] than the value $A = 2$ assumed to estimate the likelihood. This effect is stronger at 400 A MeV where the average mass of hydrogen particles is expected to be significantly less than 2. In order to treat the data for the three incident energies on the same basis we opted to exclude the hydrogen isotopes from the fit at all three energies. We shall however compare the fit prediction also to the measured hydrogen spectra with and without isotope separation in order to assess the deviations from the blast model reference.

We shall start with rapidity spectra, then switch to average kinetic energies as function of mass, kinetic energy spectra, transverse-four-velocity spectra and, finally, polar angle distributions.

4.2.1 Rapidity spectra

In the following we shall show rapidity distributions with a cut, u_t on the transverse four-velocity. From the previous section we have learned that the rapidity spectrum with a cut on the transverse four-velocity could discriminate between various blast profiles if sufficiently heavy clusters are available. In a simultaneous fit to all data (both in terms of various cluster sizes and in terms of the full measured phase space) it is however not obvious *a priori* on what the fit will eventually compromise. In Fig. 12 we show from the data at 250 A MeV the rapidity distributions for clusters of nuclear charge $Z = 4$ and $Z = 5, 6$ together with the blast model fits using the 'Shell', 'Box', and 'WS2' velocity profiles defined in section 4.1. Apart from the obvious peaking of the data at midrapidity, which confirms once more the central-source origin of these clusters, one can also see that the 'Bubble' or 'Shell' scenario is evidently in conflict with the data (lower panels). Although the 'Box' scenario (middle panels) avoids the two-humped feature of the 'Bubble' scenario, it is still seen to be too flat. Only the Woods-Saxon profile 'WS2' gives a reasonable account (note the *linear* scale) of the data. While there is a clear need for a finite diffuseness, we found the difference to a scenario with half the diffuseness, 'WS1', (not shown), to be too small to make a definite choice. We finally opted for the large diffuseness because it yields a somewhat smaller thermal energy \mathcal{E}_{th} . The reasons why we want to minimize the latter (while preserving a good description of the velocity space distribution) will become clear in section 5. So in the following we shall show only fits with the scenario 'WS2'. With this scenario fixed, the blast fits are a *one-parameter* optimization: the ratio $\mathcal{E}_{\text{coll}}/\mathcal{E}_{\text{th}}$. Quantitative results are summarized in Table 3. The leading error estimate (in the frame of the model, of course) can be found in row two, $\mathcal{E}_{\text{coll}}$, and stems from the uncertainty of the details of the flow density profile and small differences between the ERAT200D and ERAT50 cuts.

In Figures 13 and 14 we show rapidity distributions for various fragments observed at 150, resp. 400 A MeV and compare with scenario 'WS2'. Several remarks can be made. The blast model describes the rapidity distributions of the IMF ($Z > 2$) with an accuracy of about 10% or better. The width of the distributions of the lighter particles tend to be larger, the deviation from the overall fit is most pronounced for the hydrogen fragments, especially at the lower energy.

4.2.2 Average kinetic energies

Fig. 15 shows the measured average kinetic energies as a function of mass in the c.o.m. polar angle range $25 - 45^\circ$. In this angular range apparatus cuts are negligible at 400 A MeV and small ($< 2\%$ for $Z < 6$, 5% for $Z = 8$) at 150 A MeV. It should be noted that we measure velocities and nuclear charges. In

the figure we have primed both the mass and the kinetic energy because the actually plotted quantities are $2Z < E_{\text{kin}}/A >$ versus $2Z$. This representation evidences the approximately linear dependence on mass ($\approx 2Z$) and stresses once more the fundamental deviation from a thermodynamically equilibrated system that is enclosed in a box rather than exploding into the vacuum. In principle, as stressed before, in a blast model description of the data with *one* global temperature, the slope $d < E_{\text{kin}} > /dA$ fixes the collective energy *independently on the profile*. However, as we shall see, this is not the case for fitting strategies that require a good reproduction of the full momentum space population, rather than reproducing the more limited information contained in the slopes $d < E_{\text{kin}} > /dA$. The results of the blast model fits with our preferred scenario, 'WS2', are shown as solid lines for all three incident energies. On the panel for the 250 A MeV data we have also shown the curves obtained with use of the scenario's 'Shell' (dotted) and 'Box' (dashed). As for the rapidity distributions we see a gradual improvement of the data reproduction when going to increasingly complex profiles with, however, a tendency to 'saturate': eventually the slope does not change much any more when going from 'Box' to 'WS2' (the 'WS1' profile which is not shown is of course intermediate between the latter two). This saturation in the mass dependence and hence the collectivity is also shown in Fig. 16 for the 150 A MeV data and turned out to be very similar for all three studied energies. A priori it may seem surprising that a fit such as 'Shell' would completely miss the measured mass dependence. We recall that the fit has to make a compromise in order to reproduce the data in the full measured phase space with the additional constraint of energy conservation: had the 'Shell' slope in panel (a) of Fig. 15 come out steeper, and hence closer to the average kinetic energy data, then the double-hump in the rapidity distributions for the 'Shell' scenario, see Fig. 12 would have come out even more dramatic, in total disagreement with this sector of phase space.

We have explored how robust the deduced collectivity was against ignoring all fragments emitted forward of 45° . We found only insignificant variations of the deduced collectivities, if at all flow was *increasing* by a few %: 62.7 ± 2.2 , 63.3 ± 1.8 , $67.6 \pm 2.3\%$ for the three energies, respectively and for the WS2 scenario. These values can be compared with row 2 of table 3. The main difference of the data between 25° and 45° and the full set of data is visible in Fig. 15 as an overall offset of the curves representing the globally fitted energies which is most pronounced for the 400 A MeV data and seems to be limited to nuclear charges $Z \leq 5$ (mass' ≤ 10).

In Fig. 17 we show on a blown-up scale the average kinetic energies of the hydrogen and helium isotopes at $\theta_{\text{cm}} = (60 - 90)^\circ$ which have been discussed in an earlier publication [26] and compare with the global trend of the blast model fit. These data, obtained with separate telescopes, but during the same runs, were triggered by a selection on ERAT corresponding to approximately 250 mb and were not part of the fit procedure which used only data from

the Plastic Wall. The global trend of the blast, which is identical to the one shown in Fig. 15, represents a fair compromise in view of the fact that the model used here is confined to a linear mass dependence and that hydrogen fragments were excluded altogether from the fit. It is obvious however that there is an important scatter of the data points away from the smooth trend. This scatter is larger at the lower energy, where in particular the alpha energy is quite low and the proton energy rather high. From the data [26] at 100, 150 and 250 A MeV one finds that the average kinetic energies of the protons emitted close to 90° is equal to the incident center of mass energy per nucleon plus an additional energy of (26.5 ± 2) MeV which is slightly higher than the average kinetic Fermi-energy of ground-state nuclei. This is remarkable as this is an *average* energy of single nucleons emitted at rather large angles in *central* collisions. Relatively speaking Fig. 17 shows that the 'surplus' proton energy over the blast model prediction increases with decreasing incident energy if one scales the energies.

Another striking observation from these light-particle data is the fact that ^3He fragments have higher kinetic energies than the ^4He fragments, a trend opposite to flow considerations. This ' ^3He puzzle' has now been seen by three groups [26,28,69].

It is not obvious from looking at the five data points in both panels of fig. 17 which of the points is really 'anomalous', but it is clear that analyses that use only these light particles to extract radial flow values [26,28] can come to different conclusions concerning flow.

The analysis of the EOS group [28] has overlap with our present analysis at 250 and 400 A MeV. Since the error bar for the 400 A MeV data given in ref. [28] is large we shall discuss only the 250 A MeV results here. Using the single-velocity formula [36] and concentrating on *all light charged particles* the EOS group extracts a radial flow of 17 ± 5 A MeV at this energy which is only 50% of ours. Their blast-model 'flow-line' (i.e. E_{kin} versus A) runs through their p,d,t and α data and is well below the ^3He point. A more detailed comparison of [28] with [26] is difficult as there are some discrepancies: the EOS average energies for the H isotopes are about 20 MeV lower, the ^4He energy is about 30 MeV lower, but the ^3He values agree with [26]. These differences are disturbing.

The flow analysis presented in [26] used *only the hydrogen isotopes*, i.e. the slope in fig. 17 given by the average kinetic energies of H, ^2H and ^3H which came out to be 20 A MeV at an incident energy of 250 A MeV. This procedure *does not include the Coulomb part* of the flow (which essentially acts as an energy offset when the mass is changed but not the charge Z), which we estimate to be 5 MeV per nucleon (see shortly) giving a total of 25 A MeV or 74% of our present value deduced from all fragments, *excluding the hydrogen isotopes*.

When passing from ^3H to ^3He , in a naive picture, only the Coulomb part of the flow should change, since the charge, but not the mass was changed. In ref. [26] the energy of ^3He was found to exceed that of ^3H by 21.5 ± 3 MeV for incident energies in the range 100-250 A MeV. Several independent estimates concur to say that Coulomb effects at best could explain half this energy difference. A simulation, done in ref.[26] using the statistical model code WIX [70] and starting from a rather condensed spherical configuration with nucleonic density $\rho = 0.8\rho_0$ ($\rho_0 = 0.17 \text{ fm}^{-3}$) taking into account Coulomb fields, predicts a 'Coulomb flow' of about 12 MeV per unit charge. A transport model simulation [45,71], also shown in [26], came to a similar energy difference of about 10 MeV and, finally, a measurement for Au on Au at 35 A MeV showed [72], for central collisions, kinetic energies slightly below 5 MeV *per nucleon*, i.e. roughly again 10 MeV *per charge*.

There are several possible reasons for the 'irregularities' in light-particle energies that make them subtle to use for flow energy determinations in the present energy range. The most obvious one is the occurrence of late evaporative decay, a more subtle one are reorganisation processes during clusterization [73]. The former would involve alpha particles much more than the ^3He fragments, which would tend to look more 'primordial'[74]. Indeed, the low alpha energies could be accounted for in a simulation including evaporative contributions [26]. One could also speculate that tritons would in general have higher contributions from decays than the Coulomb-inhibited ^3He 's. However, the $t/^3\text{He}$ difference could not be explained in ref. [26]. As the statistical model has other difficulties, as we shall see in section 5, a firm conclusion is not yet possible.

The reorganization processes, or self-organization alluded to in ref. [73], concern the processes of amalgamation of nucleons to clusters. Energy and momentum conservation in such local processes demand that the condensation energy be taken up by the surroundings, that do not clusterize, i.e. by single nucleons. This could explain the high energies of single protons even at 90° in the c.o.m..

Characteristic structural influences of the mean kinetic energies are also visible from Fig. 15, for example the S-like shape particularly visible with the 400 A MeV data.

4.2.3 Kinetic energy spectra

How well does the blast model reproduce the *shape* of the kinetic energy spectra? This is shown in Fig. 18 for charge separated fragments at $(25 - 45)^\circ$ and Fig. 19 for the light-particle data at $(60 - 90)^\circ$. The reproduction of the data by the WS2 blast is rather good. The $Z=1$ theoretical spectrum around

35° was constructed assuming that the d/p and t/p ratios are the same than at 90° [26], but then substituting for the conversion from velocities to energies the assumption $A = 2Z$ used in the experimental evaluation. The resulting rather steeply sloped spectrum represents the most serious deviation of the model from the data.

In Fig. 19 the model calculation used again the known isotopic ratios, but not the *absolute* values which were fixed from the 4π extrapolated Z-distribution resulting from the fit to the Plastic Wall data. In view of this, the reproduction of the data also on an absolute scale is satisfactory and shows the internal consistency of the analysis. There are some subtle deviations of the model from the data. The most striking ones concern protons and ^4He . Relative to the blast model the data show a lack of low-momentum yields for the protons and a lack of high-momentum yields for the ^4He fragments. Both of these observations tend to support our speculations made in the previous section.

4.2.4 *Transverse four-velocity spectra*

Another aspect of the data, the transverse momentum distributions, is shown in Fig. 20 for the 150 and 400 A MeV data for two cuts on rapidity. The 30° laboratory cut starts influencing the data at $u_t > 0.6$ ($y < 0.5$) and $u_t > 1.0$ ($y > 0.5$). There is an excellent description of the midrapidity part, even for $Z=1$. None of the spectra shows a trace of a bubble (or hollow cylinder) depression. The high rapidity part is generally underestimated, revealing the deviations from the assumed isotropy (more prolate event shapes) at larger rapidities. This trend is larger for the $Z=1$ and 2 fragments than for the heavier fragments and for the latter it is larger at 150 A MeV than at 400 A MeV showing once more the higher conversion to isotropy at the higher energy that was visible already in the topology plots in section 3.

4.2.5 *Polar angular distributions*

In the limit of very central collisions flow effects with directional preference can no longer be quantized with respect to a 'reaction plane' [49] since the high degree of axial symmetry achieved in such collisions, together with finite-number fluctuations, precludes an accurate reconstruction of this plane. In that case one expects *polar* angular distributions to exhibit possible signatures of anisotropic flow.

In particular the 'squeeze-out' effect [75–77,31], if dominated by compressional, possibly shock-like effects, as implied by the name [50], should then become maximal and lead to a pronounced peaking around 90° in the c.o.m.. Such predictions were made long ago [47] in the framework of classical hydrodynamics and were also made recently by microscopic calculations [45,71,78]. The other

important cause of the preferential 'out-of-plane' emission of high-momentum ($u > 1$, in scaled units) fragments (if done in the proper flow frame that avoids 'spectator' contaminations [77]), namely shadowing effects caused by absorption or at least 'cooling down' in relatively cold non-participant matter, should be minimal in the case of truly central events in symmetric systems.

We expect that data obtained with the completed FOPI detector will elucidate this important question in the near future. With our Phase I limitation momentum spectra at 90° are cut off at scaled momenta $p > 0.6$. Nevertheless it is useful to take this exploratory look at polar angle distributions in highly central collisions for at least two reasons: a) since we have used an isotropic blast model as reference for comparison with the data, it is important to assess how well isotropy is fulfilled at least to the degree to which this is possible at present; b) the high sensitivity of the heaviest observed fragments to flow in general, demonstrated earlier, might lower the limit of p above which directional flow effects become measurable as compared to observing single nucleons [79]. Indeed, for less central events we have seen clear squeeze-out signals even in this limited geometry when looking at IMF's [80].

In the following we shall concentrate on the 400 AMeV data as compressional effects are likely to be stronger at this energy than at 150 or 250 AMeV and because threshold effects are less important. A more detailed investigation of the 150 AMeV data will be published separately [51]. We recall (see section 3.1) that here we have attempted to minimize autocorrelation (which distorts the distributions severely, in particular for heavy fragments) by excluding the particle of interest from the calculation of the selecting global quantity (PM, ERAT, Directivity).

Figure 21 shows for fragments of different size the degree of compatibility of the data (cut ERAT200D) with the isotropic scenario. Deviations from isotropy (taking into account the geometric cuts) are on the 20% level or less. In particular the yields of charge-one fragments show a surplus at angles forward of 50° which increases with decreasing angle. Due to the $1/\sin\theta$ weighting this surplus is actually less than 10% in terms of count rates and general balances in charge and energy. The overshoot at angles below 45° (necessarily balanced by a slight undershoot at higher angles) is higher at 150 AMeV where it reaches 30% and extends to all fragment sizes. The more prolate topology at this lower energy, when using the present selection methods, has been displayed already in section 3.

If one makes a cut $u \leq 0.5$ on the scaled four-velocities, one can check, at 400 AMeV, the isotropy from 10° to 160° . This is shown in Fig. 22 for different global event selections. Isotropy holds within 20% or better for all these selections. A few finer points can be noted: for the 200 mb selection on PM a faint remnant of side peaking near 25° is visible; after application of the directiv-

ity cut, PM200D, the cross section drops to 20 mb and statistical limitations prevent one from observing deviations from isotropy below the 20% level. The selections ERAT200 (≈ 200 mb) and ERAT200D (≈ 80 mb) are very similar, but tend to show a forward/backward asymmetry on the order of 10% despite the removal of the autocorrelation. Although we cannot exclude completely double-hit distortions, there are at least two other 'true physics' reasons why one would see asymmetries of this order of magnitude when using our selection methods. First, we define ERAT, Eq. (1), using only particles emitted in the forward hemisphere, i.e. our selection criterion is not symmetric with respect to the c.o.m.. Applying the same technique (and filtering) to our blast model simulation, we were able to reproduce such asymmetries and interpret them as forward-backward fluctuations due to finite number effects. A second effect, that was not incorporated in our simulation (at the present stage) is the fact that the autocorrelation might not be completely removed, if many IMF's were to be accompanied by a splitting partner at the late evaporative stage (so that the 'primary' correlation is not completely removed as the splitting partner is not identified).

When using again the u cut, the data at 250 A MeV and 150 A MeV look very similar, even in detail, and are therefore not shown here.

To assess the importance of the isotropy in this 'inner' part (momentum space) of the fireball, one should be aware that the $u < 0.5$ cut is rather severe and represents only 20 – 25% of the full spectra at 45° (c.o.m.). It should also be remembered that only the ERAT200D and PM200D selections are *azimuthally* symmetric (by construction), while the ERAT200 and the PM200 selections, even with a mid-rapidity cut $0 < y < 0.5$, are not (see Fig. 4).

Our general conclusion concerning polar angular distributions is that they do not show convincing evidence for *dramatic* shock effects (i.e. 90° *polar* squeeze out) as predicted semi-quantitatively in the early days [47,50]. Since out-of-plane yield enhancement *has* been seen [80] under similarly restrictive cut conditions, especially for collisions with rather large impact parameters (7 fm), one is also tempted to conclude that the presence of non-participant matter is required for the mechanism of 'squeeze-out'. Full phase space coverage in future data should further qualify these statements.

5 Chemical composition

Besides the velocity-space distributions the second topic of high interest in these central collisions is the distribution of the yields for the various fragment species. In Fig. 23 we show as example the measured fragment charge distributions at 250 A MeV incident energy. Various centrality cuts were ap-

plied (see Table 1): PM200, ERAT200, ERAT200D, ERAT50. In addition to the clean-cut filter specified in Table 2 and section 4.1 the data were restricted to polar angles $\theta_{cm} > 20^\circ$. It is evident from the figure that the nuclear charge distribution is much more robust to the cut than the velocity-space topologies discussed earlier (see also [18]). This fulfills a necessary, although not sufficient, condition for the application of a one temperature concept as used in the present analysis.

Such clean-cut distributions formed the basis for extrapolating the data to 4π . Specifically, a blast-model event-generator with the mass-dependent velocity-space parameterization determined earlier, was fed with the measured filtered Z-distribution and the missing parts were numerically calculated as function of Z and θ_{cm} . The resulting 4π integrated yields are given in Table 4 and plotted in Fig. 24. As an important consistency check the 4π integrated total charge obtained in this way should be 158 for the Au on Au reaction. Table 3 shows the % deviations we found from the adopted WS2 scenario. Except for the 150 A MeV data, where a 13% deviation was obtained, the total charge is reproduced within 5% or better. This shows that the isotropic blast scenario is not dramatically different from the data and in particular that the missing high-momentum parts near 90° , that will be measured in future runs with the full detector, are unlikely to change this conclusion qualitatively. The higher deviation for the 150 A MeV data was to be expected in view of the somewhat prolate topologies at this energy and for the selections chosen here. As a zero-order correction and neglecting pionic contributions, the yields in Table 4 were renormalized to 158. The errors given in the Table are statistical only. The uncertainty from the cut-dependence is 10% at the most till about $Z=6$ and increases up to 30% at the end of the shown distributions. The uncertainty from the extrapolation is of the order of the normalization deviations just discussed and concern primarily the ratio of the hydrogen fragments to the rest, as the phase-space distributions of the former are not described so well, especially away from mid-rapidity. As we shall see all these uncertainties are well below the uncertainties of theoretical models.

Fig. 24 shows also the exponential curves $N \exp(-\lambda Z)$, that were least-squares fitted to the data excluding the light particles and the $Z = 4$ point (which is low because ^8Be decays before it reaches the detectors). The resulting slopes λ were 0.625 ± 0.010 , 0.908 ± 0.012 and 1.170 ± 0.018 for 150, 250 and 400 A MeV, respectively. The resulting average cluster masses are 3.20 ± 0.05 , 2.20 ± 0.03 and 1.71 ± 0.03 , respectively (the errors imply a χ^2 per degree of freedom equal to one). These fits serve to enhance the special role played by hydrogen and helium fragments and also reveal some odd-even structures: the fragment yields for $Z = 9$ (F) and 11 (Na) are presumably somewhat low because ^{18}F and ^{22}Na are less stable isotopes. All of this suggests the influence of evaporative decays. As a matter of fact, if one were to speculate that *all* the surplus of hydrogen and helium nuclei above the exponential extrapolation

is due to evaporation, then less than half of the light charged particles are 'primordial' in this energy regime.

With the aid of the light-particle data of ref. [26] and the neutron emission estimate presented in section 4.1, it is possible to complete the picture with various other multiplicities given in Table 5. In using Table 5 it should be kept in mind that the isotopic composition of the $Z=1$ and 2 fragments at 400 A MeV has been extrapolated from [26] (section 4.1) and that neutron yields were estimated using eq.(20). The error in the latter was estimated by replacing the assumption $A = 2Z$ by $A = 2Z + 1$ for $Z > 2$. An idea of how 'clusterized' the hot nuclear matter is at freeze out is given in Table 6 which shows the percentage of protons and nucleons bound into clusters. These numbers are also plotted in Fig. 25 together with the deduced IMF multiplicities, an observable that finds great attention in the multifragmentation literature. The 'degree of clusterization' of protons is high (about 80%) and hardly varies with incident energy. What is changing with energy is the *size* of the clusters.

Another point of interest are the event-by-event fluctuations of some of these multiplicities within this tightly selected central-collisions sample. This is shown in Fig. 26 together with distributions obtained with our blast-model simulation, duly filtered to allow a direct comparison. It is useful to note that the simulation uses a simple Monte Carlo procedure to generate events from the multiplicity distributions given in Table 4 and with the velocity-space parameters of our WS2 scenario. Only events that strictly conserve mass, charge, energy and momentum are allowed. No other correlation of any kind is assumed. The simulation does extremely well in reproducing the External Wall multiplicity distribution (panel a in Fig. 26), the IMF multiplicity distribution (panel b) and the anticorrelation of the average IMF multiplicity with the light-particle ($Z < 3$) multiplicity. This latter plot (panel c) illustrates the sort of bias one introduces on IMF multiplicities if one selects events by making cuts on the light-particle multiplicity, as is sometimes done in the literature. The major conclusion is that we find no evidence for fluctuations other than those expected from finite number fluctuations under the constraints of conservation laws.

Does the apparent purely statistical nature of the fluctuations, together with the exponential behaviour of the nuclear charge distributions beyond $Z=2$, suggest a thermal mechanism? Since we have determined the 'thermal' part of the available energy (see Table 3) we can use existing statistical multifragmentation models to check this idea. The only parameter left was the bulk freeze-out density which we fixed to the value $0.4\rho_0$, where ρ_0 is the equilibrium density of nuclear matter in its ground state. This value is derived from the IMF-IMF correlations analysed in [24].

We have done calculations with three codes: QSM or 'Quantum Statistical

Model' [81,82], WIX [70] an extension of an older code FREESCO [83], and SMM or 'Statistical Multifragmentation Model' [14]. The results of these calculations are shown in Fig. 27 together with our data. As these models are well documented we shall only recall here the general idea: following statistical principles all possible final states are sorted out and their relative probabilities are calculated. The probability of a certain final state of the decaying system is proportional to its statistical weight, i.e. to the number of microscopic states leading to this final state. In all three implementations an initial 'fast' multifragmentation is followed by a 'slow' evaporation from the 'primordial' fragments. While QSM gives 'exact' ensemble averaged results, WIX and SMM generate individual events and hence also contain fluctuations.

Coming back to our data, what we find is that all calculations underestimate the formation of heavy clusters. For QSM the degree of underestimation at the oxygen level is also shown in one of the panels. At 400 A MeV the oxygen rate exceeds the values calculated with QSM by four orders of magnitude. In order to give an idea on what is changed if one increases the collective energy (and hence decreases the thermal energy) by the maximum amount that seems tolerable from our analysis (see Table 3), we show the corresponding results as dotted line in the same panel. We note also that switching to the lower freeze-out densities usually used in the literature (and contributions from the tails of the density distribution implied by our diffuse flow density profile), increases the discrepancy between theory and data. The same is true to an even higher degree, if we were to use the lower collective flows deduced from the light-particle data [26,28].

A very old problem in applying statistical models to the calculation of yields is the number of very high lying, usually unresolved, levels that are included: these are either ignored (QSM) or a level density formula with a cutoff function (SMM, WIX) is used. In particular WIX [70] uses as cutoff function

$$F = \exp \left[-\frac{1}{2} \left(\frac{\epsilon - B}{\epsilon_{\text{cut}}} \right)^2 \right] \quad (24)$$

where B is the barrier against the most favourable light-particle emission mode and the width is given by $\epsilon_{\text{cut}} = C_{\text{cut}}(\sqrt{A-3} - 1)$, where C_{cut} is a parameter. Fig. 28 illustrates the change in the WIX prediction if one modifies the cut-off energy. The oxygen yield (none within a statistics of 6000 events in the case $C_{\text{cut}} = 2$ rises considerably (to 16 fragments) when $C_{\text{cut}} = 8$ is chosen. The right panel in Fig. 28 shows the distribution of the ^{16}O levels [84] and compares it to the corresponding predicted average excitation energies E^* of oxygen in the two cases. For $C_{\text{cut}} = 8$, the 'standard' value in WIX, one finds $E^* \approx 60$ MeV, well outside the region of known levels. The $C_{\text{cut}} = 2$ parameterization (which we also used for Fig. 27) leads to $E^* \approx 20$ MeV. (In ref. [85] QSM and FREESCO were shown to be equivalent, but there only

light-particle predictions were compared).

As an aside, we present in fig. 28 also a standard calculation for the 250 A MeV data that does not include evaporation (open-circle symbols). This approximation was used in [22]. The quality of data description achieved here is comparable to that obtained in ref. [22].

Coming back to the cut-off problem, one may suspect that one is doing some double counting if one is including many high lying broad resonances, as these must, in virtue of Levinson's theorem [86] have a negative echo in the undisturbed continuum spectrum, an effect that is not usually taken into account. As these uncertainties affect the predictions and prevent a definite conclusion concerning the more fundamental issue, namely the adequacy of the statistical approach, it will be necessary in the future to set the treatment of, largely unknown, high lying levels on a better foundation.

One consideration that could save the statistical model (although its practical implementation would have to be rethought) would be to postulate a higher density at which fragment sizes are 'frozen out'. IMF-IMF correlation radii [24] are not necessarily 'cluster-size freezeout' radii, as such correlations are primarily sensitive to the last Coulomb-interaction when sizes are fixed already.

Interpreting naively the probability of oxygen (^{16}O) formation as P_c^{16} where P_c is the clusterization probability, one could account for the oxygen yields by raising P_c by a factor of 1.7-1.8. This could be done by switching to about twice the density assumed in our calculations, or about $0.8*\rho_0$. At this density, of course, the present implementations of statistical models [11,14,81,87] are not valid. Three considerations make this speculation interesting however, and perhaps worth pursuing:

- (1) It seems reasonable that clusters heavier than hydrogen would form at a time where the average density is still comparable (although somewhat lower) than the densities of the clusters that are about to form, which presumably are not too far from 'normal' density. This would also provide a fast mechanism as at high density rearrangements are more frequent. It is interesting in this connection that new algorithms to detect clusters in simulations are now able to discern clusters at a very early stage [88,89].
- (2) This could bring out-of-conflict the very low apparent chemical temperatures needed to explain the data with low freeze-out densities. At higher density clusters statistically 'survive' at higher temperature (see also fig. 5 in ref. [18]). The combined high-density and temperature would put cluster formation in these central collisions well outside the spinodal regime [90]. The almost perfectly exponential yield-distribution and the absence of non-trivial multiplicity fluctuations also favour this viewpoint.

- (3) The measured radial flow for heavy clusters would now be a signature of *compression* as it could not have developed in the low density phase. It is also interesting to note that the QMD model with Pauli-potential [91] predicts multifragmentation only if compression is present ('mechanically excited'). In this connection we also refer to section 6.3 where we found, using QMD, a mean-field dependence of clusterization.

6 Experimental data and molecular dynamics

It is attractive to use transport models because they do not rely on a priori assumptions of global or even local equilibration. Such models, which are able to simulate collisions event-by-event, are more ambitious, but in order to be usable they need to introduce many approximations that must stand the test of time. One such model is Quantum Molecular Dynamics (QMD) [43] and more specifically one of its variants the Isospin (I)QMD [55,56].

In the context of this work we were primarily interested in checking what such models have to say about the general topology of central events: can we at all expect a 'radially exploding fireball' in such collisions with a maximum of 'nuclear material' (in earthly laboratories) and a minimum of 'spectator' material? In particular is the observable ERAT, eq. (1), anywhere close to the reference value of two, expected from a global thermalization scenario? Are our methods of selecting central collisions by maximizing ERAT and minimizing side flow supported by such simulations? Because of the claim of QMD to handle non-trivial fluctuations, what does it have to say to the degree of clusterization (in the structureless 'liquid-drop' kind of sense) and its possible connection to the phenomenon of radial flow extracted in the previous sections?

The general idea of QMD [43] is to use the wide spread method of molecular dynamics with some quantum modifications specific to the nuclear context. For a derivation of the theory from a variational principle we refer to [92]. As in molecular dynamics one solves the classical (non-relativistic) hamiltonian equations of motion for a system of A nucleons (and in the case of IQMD more explicitly a system of Z protons and N neutrons) that evolve under the influence of nucleon-nucleon interactions. These involve in the case of IQMD [55] Skyrme-type (density dependent) interactions, a Yukawa term with a range parameter $\mu = 0.4$ fm, a symmetry potential between protons and neutrons corresponding to the Bethe-Weizsaecker mass formula, a Coulomb interaction between charged particles and, finally, a momentum dependent term. An important decision taken within the model is to adjust the parameters of these phenomenological interactions to properties of cold, i.e. highly degenerate nuclei: binding energy per nucleon, asymmetry energy, saturation density and

the real part of the nucleon-nucleus optical-model potential. One important difference to conventional molecular dynamics is the following: for the calculation of the potential gradient that is driving each individual nucleon, these are not treated as point particles, but are given a finite, but fixed spread around their classical phase-space location. This density spread is Gaussian with a variance $2L$ in coordinate space and an associated uncertainty-principle-conserving spread $\hbar^2/2L$ in momentum space. This finite spread introduces de facto a finite range into the Skyrme-(δ -function)-like interactions and hence influences the finite-system dynamics and in particular also the establishment of correlations such as clusterization. There is some freedom in the choice of L : in the IQMD model the canonical value is $L = 2.165 \text{ fm}^2$ for Au on Au simulations. The freedom in the other parameters of the phenomenological interactions allows to tailor them in such a way that they imply a fixed compressibility K when applied to homogeneous nuclear matter. It has been customary to allow for a so-called 'hard' (H) version of the equation of state (EOS) corresponding to $K \approx 400 \text{ MeV}$ (388 MeV to be exact) and a 'soft' (S) version, corresponding to $K = 200 \text{ MeV}$. The present status from 'low-energy' nuclear physics is a value $K = 215 \text{ MeV}$ from a theoretical analysis [93] of the 'breathing modes' of nuclei, i.e. the giant monopole resonances (GMR) as excited typically by high-energy alpha scattering. (A very recent search for still missing strength in the GMR [94] came to the conclusion that K values as high as 300 MeV could not be excluded from the GMR data).

Another important difference to molecular dynamics, but a point in common with BUU-type approaches [95] is the treatment of so-called 'hard' collisions by a Boltzmann-like binary-collision integral, borrowed from classical transport theory for dilute systems, and supplemented by a Nordheim-Uehling-Uhlenbeck term to account for Pauli-blocking at least on the local level. In this model it acts as an entropy-producing non-deterministic term as in practice collisions are dialed with Monte-Carlo methods whenever two nucleons approach within the radius corresponding to the total 'hard' cross section. Again, an important decision within the model is to use free scattering nucleon-nucleon cross sections, i.e. this part of the model (in contrast to the 'soft' collisions) is adjusted to the properties of infinitely dilute nuclear matter. IQMD distinguishes neutrons, n , and protons, p , i.e. it uses the relevant cross sections σ_{np} , σ_{pp} and σ_{nn} . Pions and Δ 's are included, but elastic scattering is dominant, still, in the present energy range.

Finally it seems worthwhile to mention also details of the initialization of each nucleus-nucleus collision, since they seem to have a surprisingly large influence on the final outcome [96]: in IQMD the centroids of the Gaussians in a nucleus are randomly distributed in a sharp phase-space sphere ($r \leq R$ and $p \leq p_F$), with the radius $R = 1.12 \cdot A^{1/3} \text{ fm}$ and the Fermi-momentum $p_F = 268 \text{ MeV}/c$. One of our prime encouragements to use IQMD was its reasonable stability against the variation of the initial distance between the two nuclear surfaces

[96]. For the present calculations, starting from a zero initialization distance, we followed the evolution for 200 fm/c (i.e. a width of 1 MeV in terms of final levels) at which time clusters were formed with the minimum spanning tree method using a clusterization radius of 3 fm [43]. Decay past this time was not taken into account. For reasons of economy we took a randomly sampled unweighted impact parameter b distribution from $b = 0$ to b_{max} , where b_{max} was mostly 14 fm and sometimes 7 fm. Experimental observables were then constructed weighting them eventwise with the factor b . In general both the hard and soft variants of the EOS were explored and some 300-1000 events per fm interval were generated.

6.1 Transverse energy (ERAT)

We shall start with the observable ERAT i.e. eq.(1) since it played a key role in our event selection. IQMD in its standard implementation just described, predicts average values that are close to two in the energy range 150-400 A MeV and for central collisions ($b = 0 - 1$ fm). The results are shown in figure 29 for both the hard and soft equations of state with momentum dependence included (HM and SM). No apparatus filtering was done here, except that neutrons were excluded. We have already mentioned the fluctuations to which ERAT is subjected (fig. 7). The filtering effect in the Phase I apparatus is considerable: the ERAT values are lowered and the relative fluctuations are increased. For unfiltered ERAT values in the range 1.5 – 2.5 we found however that the filtered value was lowered to a relatively constant fraction of $46 \pm 2\%$, so that differences between different parameterizations are preserved. Therefore we can roughly say that a modification of the unfiltered average ERAT value by 0.2 units will give rise, after filtering, to a shift along the abscissa of about 0.1 units in the tail of the distribution (at the 20-60 mb level in fig. 30). Also, we observed in all model simulations that parameterizations that lead to higher values of ERAT for $b < 1$ showed increased 'transversality' at other impact parameters as well. As the value for the hard EOS happens to be almost exactly two for central collisions at 250 A MeV, we compare the ERAT distribution ($b = 0 - 7$ fm), after filtering with the corresponding FOPI data in fig. 30 and find that it follows the data rather well. As a curiosity we have also plotted in the same figure the (filtered) blast-model prediction using the chemical composition and momentum space distribution as fitted to the data (but not to the ERAT distribution). Of course the unfiltered average value for the blast-model is exactly two. We have already shown in section 3 that the blast model fluctuations which are purely statistical, but obey constraints of mass, charge, energy and momentum conservation, come out identical to those of IQMD (fig. 7). Since the blast-model is conceived only for central collisions, its normalisation is dependent on what is defined to be 'central'. We see from the figure that a central component of the innermost 1 fm (or 30 mb) seems

to hug the tail of the measured distribution.

The top panel of fig. 30 shows the b -dependence of (unfiltered) ERAT values predicted by the HM and SM versions of IQMD. In the same figure we have also plotted the values predicted by a Vlasov-Uehling-Uhlenbeck (VUU) calculation using a different code [71]. This model was used earlier in our Collaboration [26] for comparison with light-particle data since it includes formation of clusters up to mass three. This feature seems to lead, in the model, to very high ERAT values. Since VUU by principle does not allow to study fluctuations, we have constructed by randomly mixing the 'test' particles [95] 'events' which have the correct total mass and charge. These 'events' then have the same relative, finite number, fluctuations as both the blast model and IQMD (fig. 7). With these trivial (but unavoidable) fluctuations added on top of the model, we can then again compare with the data. As can be seen in fig. 30 (this calculation is limited to $b = 0 - 5$ fm), models with such copious transverse momentum generation are incompatible with the data. This particular model predicts substantially lower ERAT values however, if composite particle formation is not included [97].

There are other, more subtle deviations between simulation and data. From fig. 29 we see that IQMD predicts for central collisions a rise of ERAT of approximately 30% (0.4-0.5 units) within the analysed energy range which, after filtering, should lead to a positive shift by about 0.2 units of the tail of the distribution when going from 150 to 400 A MeV. In contrast, the data, fig. 2, reveal, if at all, a trend to *smaller* ERAT values at the higher energy. (The measured ERAT distribution for 150 A MeV lies almost exactly on top of the distribution for 400 A MeV if it is shifted *down* by 0.1 units). Despite the estimated uncertainty of the data (maximally 0.1 units) one can therefore say that ERAT, in the experiment, does *not* increase with the incident energy.

If the naive concept of global thermalization were to be fulfilled in nature, ERAT would be 'dynamically inert' in the sense that its value for central collisions would not depend sensitively on details of the calculation, but always have the value of two. Instead, however, all the simulations that we have done ourselves, or became aware of, show that ERAT seems to 'react' to many parameter variations. Besides the disturbing dependence on the more 'technical' parameters [96] such as the spread parameter L described earlier, and even the details of the initialization (sharp spheres versus Woods-Saxon profiles, choice of Fermi-energy [96]), there are the more fundamental dependences on the EOS (according to IQMD a 20 – 30% effect, see fig. 29) and above all on the implemented nucleon-nucleon cross sections that enter the 'hard' collision term.

From a recent paper by Botvina et al. [98] it was shown that the predicted final event shape in momentum space could vary from strongly oblate shapes

(high ERAT values), obtained if constant cross sections $\sigma_{np} = \sigma_{pp} = 40$ mb were assumed (see also [78,51]), to slightly prolate shapes if the 'in-medium' nucleon-nucleon cross sections were lowered. ERAT values higher than two for highly central collisions ($b < 2$ fm) should lead to polar angular distributions peaked at 90° in the c.o.m. [71,78]. This important cross connection and the possibility to draw conclusions on the magnitude of in-medium cross sections will be discussed more quantitatively in a separate paper [51].

Our general conclusion is that measured ERAT distributions are an important constraint to models.

6.2 Sideflow and centrality

In the lower panel of fig. 31 we use IQMD to study the evolution of sideflow with the true impact parameter b (solid curve). Sideflow is quantized in terms of p_x^{dir} , eq.(5), in scaled units. The soft (momentum dependent) EOS was used and the apparatus filter applied. Notice the enlarged abscissa scale: of the approximately 14 fm range of impact parameters only the innermost half is shown. When using ERAT binning instead of the true impact parameter we find that the curve follows the original b -dependence amazingly well down to the 1 fm level (where the 'true' p_x^{dir} becomes negative). When using multiplicity binning there is a lack of b -resolution below 3 fm resulting in an almost flat dependence, much the same as in the data, fig. 5. This supports our method of picking central events: low side-flow plus high transverse momenta. The efficiency of this method should depend on the scaled strength of the sideflow at intermediate (3 – 5 fm) impact parameters where it is peaking.

How does this strength evolve with incident energy? In the figure 2 we have seen that the ERAT distributions vary rather modestly with incident energy. One of our main results from the blast-model analysis, table 3, was that the radial flow takes up a nearly constant amount of the available energy. A more detailed look back at the varying topologies, even in the most central collisions, see Fig. 9, shows that 'scaling' is approximate at best, however. Scaling of observables in heavy ion collisions has been considered in refs. [99,100]. In analogy to Reynold's famous laws governing viscous flow, one can expect [99] in the hydrodynamics framework that scaling might exist under certain conditions. Scaling would reduce many systems of different size and incident energy into one. Deviations from scaling could then isolate interesting phenomena known to violate scaling: the most obvious ones are the influence of the EOS, and connected with it, possible phase transitions.

IQMD predicts that sideflow *does not* scale in this energy range, see fig. 31. As shown in the upper two panels, this agrees almost quantitatively with

experiment. The conclusion does not depend on the specific choice of the sideflow observable: using F_{DO} , eq.(4), which does not involve the so called reaction plane explicitly, leads to very similar results. There is relatively less sideflow at the lower energy and hence the method of using 'absence of sideflow' to increase centrality will be less efficient as the energy is lowered even further. We note in this context that the observables p_x^{dir} and F_{DO} are expected to be 'coalescence-invariant' and hence better suited for scaling studies than the slope of dp_x/dy taken at midrapidity which is steeper for clusters [15,29,105] than for nucleons.

Is the EOS responsible for this lack of scaling? We found only very modest differences in the calculations using the hard instead of the soft version of the EOS. (Momentum dependence in this model seems to affect primarily the high impact parameter side of the peaks in fig. 31 leading to a broadening of the peak and a slight shift to higher b). 'Disappearance of sideflow' [101–104] in the energy range 50 – 150 A MeV has been primarily associated with the transition from predominantly attractive to repulsive forces, i.e. to the EOS. In view of our IQMD results and our observations of the evolution of phase space with energy (fig. 9) another cause for non-scaling is suggested: the variation of the time-scale with incident energy versus the fixed time-scale typical of Fermi-motion. Sideflow, quantized with the observables p_x^{dir} or F_{DO} , is primarily a 'spectator' phenomenon (a more detailed study of relevant FOPI data will be published separately [105]): it develops into 'full bloom' only when there is a clearcut spectator-participant separation. This separation, as we have qualitatively observed, is less pronounced at lower energy (see for example fig. 10). In this picture the 'spectators' are seen to be recoiling under the explosive power of the fireball. Although this push from the fireball scales in ultracentral collisions, there is, at energies still comparable with the Fermi-energy, sufficient time for some 'cross-talk' possibly via a different, one-body mechanism known from the theory of deep-inelastic heavy-ion collisions [60,61] to mitigate the recoil. The 'spectators' are cooling the fireball and the fireball is heating the spectators, i.e. there is some start towards a more global equilibration that weakens sideflows at freeze-out. In this picture, at some high energy, when the above globalization seizes to work because of a lack of time, sideflow at sufficiently small b might become just a reflection of (scale with) the radial flow. At very high energy (CERN SPS energies?) another time scale might come in: the spectators pass by with essentially light velocity, but see an increasingly contracted participant. If the explosion time scale is too long, again, there will be little scaled sideflow seen.

Another aspect of participant-spectator geometries, enhanced flow out of the 'reaction plane' or 'squeeze-out' [50] might also be governed by such time scale comparisons. Eventually, this may turn out to be an important clue to setting scales for the fireball explosion (see also [45]). *Quantitative* assessments will definitely require the use of highly refined transport theories. It will be

interesting to establish the low as well as the high energy connection by using the same type of analyses and ideas.

6.3 Clusterization

We were only semi-successful in understanding the degree of clusterization using statistical concepts. Is a full-blown transport theory more successful? Presumably a theory of clusterization in heavy-ion collisions will have to contain 'the right amount of quantum mechanics'. Antisymmetrization of fermionic matter, which has *nonlocal* consequences, is a key ingredient in understanding 'the making of nuclei', one of the fascinating subjects of 'hot nuclear matter'. So far, fully antisymmetrized approaches to heavy-ion collisions [106,107] could not be extended to heavy systems such as Au on Au owing to exorbitant needs for central processor time. *Locally*, some requirements of antisymmetrization are taken into account in QMD as well as BUU/VUU by the introduction of a Pauli blocking term into the collision integral. Some QMD approaches have also introduced Pauli-potentials [91] to prevent Pauli-forbidden local overlap in phase space. It is still an open question whether this sufficiently mimics the needs for antisymmetrization. The momentum dependence introduced by Pauli potentials has a profound influence on the local kinetics [108]. Basically, the clusters in QMD remain classical objects and for example do not have the correct heat capacity at low temperatures [91,108]. Of course shell effects that might come in at freeze out time, namely preferred alpha formation [107,109] are completely missing in (I)QMD. At best one can hope to obtain 'macroscopic' kinds of clusterizations in a spirit similar to macroscopic mass formulas (which are known to be successful in explaining global trends).

We have added in Fig. 27 the charge yield predictions of IQMD to be compared to the statistical model calculations. IQMD is doing well on a logarithmic scale, but does not include decays after 200 fm/c. As IQMD is a dynamic model, it is worthwhile looking at clusterization in more detail. There are different ways of quantifying the probability of clusterization. In order to allow a direct comparison with 4π extrapolated data, we have plotted in fig. 25 for the momentum dependent versions (SM and HM) the IQMD predictions for the multiplicities of the IMF's and for the degree of proton clusterization (in a cluster of any size). It is obvious that the probability to clusterize is underestimated by the present implementation of IQMD. We recall that no decay after 200 fm/c is included: such sequential decays (see section 5) would increase the discrepancy.

The failure of the model is most dramatic at the highest energy and, there, is specifically associated to *central* collisions. This is illustrated in fig. 32 where a combined ERAT (low b) PM (intermediate b) binning was used to take

advantage of the better 'resolution' of b (suggested by the simulation) when a combined method is used. Experimental 'impact parameter' dependences of IMF multiplicities in Au on Au collisions have been shown earlier by the MSU/ALADIN collaboration [19], where however charged particle multiplicity was used for the entire range of cross sections, which may represent a bias for such observables in the tails of the distributions (see our fig. 26). A direct comparison with [19] is not straightforward as both apparatus have different filtering properties. It seems however that there is a real discrepancy for the most central collisions, namely at 400 A MeV, as our 4π extrapolated IMF multiplicities (see table 4) are higher by at least a factor two.

The failure to predict sufficient clusterization was also reported in [19]. It is known [96] that the clusterization probability is influenced by the width parameter L . Varying L does however have also complex influences on other observables [96]. We stress that the failure to clusterize with sufficient probability is not limited to large clusters (IMF's) but holds also, and even more so, for the so-called light charged particles (LCP's). Using the soft EOS, which seems to be more favourable to clusterization than the hard EOS (see later), the He/H ratio is underpredicted by a factor 5 at 150 A MeV and of 6 at 400 A MeV.

Despite this problem, we show a very interesting effect: in IQMD the potential interaction seems to influence *dynamically* the probability of clusterization, see Fig. 33. In general, more clusters are made using the soft EOS, and at high impact parameters the momentum dependence seems to favour clusterization as well. In a different context the breaking apart in explosions has been connected to the speed of the expansion [110] : loosely speaking, the faster the explosive moves apart the smaller the pieces. If fragments are not formed by density fluctuations in a quasi-equilibrium situation but in an out-of-equilibrium regime, what is at stake is an energy balance between the kinetic energy of expansion and the potential energy of broken surface bonds [110,111]. In the nuclear context the time scale could be partially set by the EOS. A harder EOS, intuitively, could drive a faster expansion, leading to smaller pieces. Under certain conditions, following [110], it is predicted that the average cluster size should vary linearly with the inverse flow energy per nucleon. Among the restrictions are a fixed freeze-out density and the assumption that the later evaporation does not modify the linear relationship. For the average cluster masses determined at three incident energies (see section 5 and Fig. 24) and the collective flows extracted from the spectra (see Table 3) we find that the linear relationship mentioned above is fulfilled with an accuracy better than 1%. It will be highly interesting to see if these speculations stand the test of time as the current transport codes are further refined.

6.4 Radial flow

The collective flow energies per nucleon listed in Table 3 ($\mathcal{E}_{\text{coll}}/A$, row 6) are in amazing agreement with the theoretical simulations in [45] where values of 21, 35 and 55 A MeV were predicted for the three energies. In [45] it was argued that these values vary only slowly with impact parameter. However the splitting into longitudinal and transverse degrees of freedom *does* vary with the impact parameter. Our discussion in section 6.1 already suggested that the simulation in [45] predicts too much 'transversality'.

Our method of extracting the radial flow, which does not need many events, was also applied to IQMD events. The main results of our analysis are reflected in a series of numbers for the fraction of the final total kinetic energy caught in collective flow that can be found in Table 7. Rows 1 and 2 in the Table show the incident energy and EOS (HM vs SM) dependence of the radial flow for impact parameters $b < 1$ fm and for charged particles emitted under large polar angles ($45^\circ - 135^\circ$). The method used, called *slope* in the Table, is based on the relation (8) (see also Fig. 34) which implies a linear dependence of the average kinetic energy as a function of mass. The flow determined in this way (using the spectra for masses $A = 1 - 10$) is not necessarily identical to the 'theoretical' flow as determined from a careful cell-analysis using the full information of momentum and position as a function of time. This method is not available to experiment however.

Judging from the numbers (row 1 and 2) in the table, there is a weak increase of the flow fraction with energy which is more pronounced at the low energy end, and there is a small bracket between the hard and the soft EOS which gets larger as the energy is lowered. This higher sensitivity to the *cold* EOS at lower energies was suggested in ref. [112] where it was actually recommended at that time (1981) that the 'best' incident energy for this purpose was around 100 A MeV! Intuitively, however, it is rather puzzling that the hard version of the cold EOS should give *less* radial flow in the IQMD simulation. The work of ref. [112] suggested that a better than 10% accuracy would be needed to solve the question of the stiffness of the EOS. The argumentation stemmed from solving the one-dimensional Rankine-Hugoniot shock equations (implying validity of hydrodynamics) to obtain the maximum density and pressure in the shocked zone. Such considerations usually indicate that the maximum pressure (which is a sum of two terms from the cold and the thermal EOS, respectively, the latter being smaller than the former only at sufficiently low incident energies) rises relatively modestly with the stiffness of the cold EOS due to a compensatory effect: the soft EOS leads to larger densities. However there is no inversion as to which EOS leads to higher pressure as implied in Table 7!

Rows 3-8 in Table 7 serve the purpose to test and defend the likelihood method as applied to the (less complete and less perfect) experimental data. Most importantly, we have checked that all the numbers listed in the table, which were obtained without experimental filtering, could be recovered with a typical deviation of 2% of the available total kinetic energy if we applied the threshold and angular cuts of the Phase I FOPI apparatus.

It is seen by comparing rows 2 and 3 in the table that the likelihood method with our preferred profile WS2 gives virtually identical results to the 'slope' method if applied to the same data with the same restrictions on impact parameter and polar angles. Enlarging the angular range to include more forward (backward) angles tends to increase the average flow, a faint remnant of the initial purely longitudinal 'flow'. In the IQMD simulation the effect is significant only at the lowest energy (row 3 versus row 4 in the table). The likelihood method, in contrast to the slope method, also tests the shapes of the spectra; rows 4, 5 and 6 compare the results for the Woods-Saxon (WS2), the 'Box' and the 'Shell' scenario's. As in the experimental analysis (Fig.16) the Shell scenario underestimates the flow, while differences between the 'Box' and the WS2 profiles are less significant than in the experiment. We also checked what was the influence of mixing-in higher impact parameters (rows 7 and 8 to be compared with rows 3 and 4, respectively). For reasons of simplicity a flat impact parameter population between 0 and 3 fm was taken to approximate the 'experimental' distribution [46]. While one finds for the larger angular range a general rise of the apparent flow as compared to the values for the more central impact parameters (rows 8 and 4), there is virtually no change if the angular range is restricted to angles closer to 90° .

This observation is our main argument for concluding that our extracted experimental flow values (Table 3) , which hold for both angular ranges, should be representative of very central collisions and are significantly larger than the theoretical values.

It is tempting to relate this smaller radial flow in the model to the failure to predict sufficient clusterization. Again, future investigations, will have to clarify if the problem is technical or if it indicates a need for a refinement of the physics of the model. On the experimental side, there is a need to fill the gap visible in the topology plots figs. 8 and 9.

Finally, a note on the flow of very heavy clusters ($A > 10$ or $Z > 5$): comparing the two panels in Fig. 34 it is seen that IQMD predicts a saturation of the mass dependence of average kinetic energies that can however be seen clearly only at the lower incident energies for obvious statistical reasons. Such a trend is weakly present also in the experimental data at more forward angles (Fig.15) and was seen more clearly at lower energies [21,27]. A possible interpretation of this effect might be of geometric origin if one assumes that there is a positive

position-momentum correlation at freeze-out. a) Since heavy clusters have central densities close to saturation density, they must coagulate further inside the expanding fireball rather than at the less dense surface. b) Because of the larger sizes the flow velocity gradients 'inside' the potential cluster may disrupt cells in the surface region [27,110]. c) A more subtle effect might be that already in the high compression phase the innermost cells of the fireball had smaller entropies per nucleon which then were conserved in the subsequent adiabatic expansion [22].

7 Summary and outlook

We have presented a rather complete account of the momentum space distributions in central collisions of Au on Au at three different incident energies, 150, 250 and 400 A MeV located around or well above the Fermi energy. These data should represent a challenge to future theoretical analyses.

The strong sensitivity to flow of heavy clusters emitted copiously in these collisions allowed us to select very central collisions by combining high total transverse energies with the absence of sideflow which could be shown to be maximal for impact parameters of 3-5 fm. This method is supported by IQMD simulations which showed, in excellent agreement with the data, that the scaled sideflow was increasing with incident energy in the present regime. The total transverse energy in the data scales however better with energy than predicted by IQMD and its magnitude excludes models that predict strongly oblate event shapes for impact parameters below 2 fm.

Autocorrelation effects which are severe in these rare events (1% of the reaction cross section), were avoided by always excluding the particle of interest from the selection condition. For these central collisions we could show that invariant cross section topologies for the IMF's in the twodimensional space of scaled transverse velocity vs rapidity varied in a subtle way when raising the energy. All topologies are basically centered around midrapidity, but tend to be somewhat prolate, becoming more compact however along the rapidity axis at the higher energy. Isotropy is reached only approximately. From somewhat less central events selected with high multiplicity window, we were able to expose the increasing participant-spectator separation with rising energy; some faintly dissipative features, known from lower energies were still evident at the lowest energy measured by us.

In a phenomenological data analysis we explored how well a thermal model that includes radial flow could reproduce the data. An isotropic blast scenario that allowed for a complex flow profile was adjusted to the data under the constraint of energy and charge conservation, yielding the subdivision of

the available energy into a collective energy, found to take up $62 \pm 8\%$, and a rest energy interpreted as thermal and used later as input into statistical model calculations. It could be shown that the heavier clusters were sensitive to the assumed flow profile and a Woods-Saxon profile with a large diffuseness was able to describe the measured rapidity distributions (applying a low transverse-velocity cut) and the transverse-velocity distributions (applying a mid-rapidity cut). In contrast, the velocity distributions of single nucleons were found to be insensitive to the assumed profiles.

The model, fitted to the full measured phase space, reproduces the size dependence of the average kinetic energies of the fragments around 35° , however there is an offset indicating that the fragments are somewhat more energetic at these angles than at more backward angles, another indication of deviations from perfect isotropy. The spectral shapes of the IMF kinetic energies are rather well rendered by the model. A close comparison with the light particle data suggest that their spectra and average energies are influenced by late decays and reorganization effects accompanying the local amalgamations.

The polar angular distributions in these highly central collisions do not support a dramatic 90° squeezeout. It seems that the presence of spectator matter is necessary for the squeezeout pattern.

The blast-model fits were used to extrapolate the fragment yields to 4π . Although the average size of the clusters decreases with increasing incident energy we found that only about 20% of the protons were emitted as single nucleons even at the highest energy (400 A MeV). The thermal energy determined from the flow analysis was used as input to statistical calculations. Using a freeze-out density of $0.4\rho_0$ suggested by the IMF-IMF correlation studies, it was found that such calculations underestimate the oxygen yields by up to 4 orders of magnitude in two of the models used [14,81]. Large uncertainties in these calculations subsist however, because of the difficulty to assess the contributions from unknown very high lying levels avoiding double-counting.

We have suggested that higher cluster yields could still be explained in the quasi-statistical framework if size-freeze-out densities around $0.8\rho_0$ were postulated. Such a possibility would also suggest that most of the observed radial flow actually already developed in the high density phase making this kind of flow a potentially very interesting observable. The relatively high apparent temperatures concurrent with this density would put cluster formation in these central collisions well outside the spinodal region. The almost perfect 'primordial' exponential yield curves that are suggested after consideration of late decay processes and the lack of nontrivial fluctuations in multiplicities and other observables, like ERAT, also favour a fast cluster formation mechanism that is only possible at high densities.

The multifragmentation could be favoured by the explosive high velocity expansion [110] and the related 'mechanical instability' [91]. This is also in line with QMD calculations which suggested that cluster formation was sensitive to the EOS. The present implementation (IQMD) of the QMD model however underestimates the degree of clusterization and does not seem to generate sufficient radial flow.

Looking forward to new experiments, besides the obvious extension of this kind of data and analysis both to higher *and* lower energy, it is clear that one should aim at resolving some of the ambiguities left in the present understanding of the data. The role of losses on the way to equilibrium could be elucidated by studying the system-size dependence of yields and momentum distributions. The freedom about the correct fragment-size freezeout density should be further constrained by determining and comparing correlation radii also with other particles than IMF's, for instance $p-p$, ${}^3\text{He}-{}^3\text{He}$ (that seem to be more primordial) and, perhaps starting from 400 A MeV, $\pi-\pi$ correlations. Close comparisons of the momentum space distributions of equal-mass particle pairs, ${}^3\text{He}/t$, π^+/π^- , would also give useful clues. In general correlation studies could give the information necessary to try to reconstruct primordial yields allowing to extract primordial clusterization probabilities, one of the clues to setting up the EOS. The degree to which complete mixing of projectile matter and target matter takes place (a necessary condition for the application of statistical considerations) could be checked by studying collisions between nuclei with different neutron to proton ratio.

On the theoretical side a *simultaneous* account of momentum space distributions *and* yields of all the emitted particles and clusters remains a challenge, a convincing mechanism accounting for the large observed radial flow must be found. Statistical fragmentation models appropriate for weakly sub-saturation densities ought to be developed and the role of high lying continuum levels explored. Refined transport models, in addition to statistical models, will be needed as supporting tools to try to extract the time scales of the explosions, perhaps by studying the scaling properties of the participant/spectator interplay in the form of sideflow and squeezeout phenomena. The future 'microscopic' theory will probably have to include the momentum dependent mean field on a relativistic basis [113–115], even at low energies, and have to treat the 'soft' collisions (mean field) and the 'hard' collisions (nucleon-nucleon scatterings) on a more consistent basis [116,117].

Acknowledgements

This work was supported in part by the Bundesministerium für Forschung und Technologie under contract 06 HD 525 I(3) and Gesellschaft für Schwer-

ionenforschung under contract HD Pel K.

References

- [1] A. Sandoval, R. Bock, R. Brockmann, A. Dacal, J. W. Harris, M. Maier, M. E. Ortiz, H. G. Pugh, W. Rauch, R. E. Renfordt, F. Riess, L. S. Schroeder, R. Stock, H. Ströbele and K. L. Wolf, Nucl. Phys. A 400 (1983) 365c.
- [2] A. Baden, H.H. Gutbrod, H. Löhner, M.R. Maier, A.M. Poskanzer, T. Renner, H. Riedesel, H.G. Ritter, H. Spieler, A. Warwick, F. Weik, and H. Wieman, Nucl. Instr. and Meth. A 203 (1982) 189.
- [3] J.P. Alard et al., Nucl. Instr. and Meth. A 261 (1987) 379.
- [4] L.P. Csernai and J.I. Kapusta, Phys. Reports 131 (1986) 225.
- [5] H. Stöcker, W. Greiner, Phys. Reports 137 (1986) 277.
- [6] R. Stock, Phys. Reports 135 (1986) 261.
- [7] R.B. Clare and D. Strottman, Phys. Reports 141 (1986) 179.
- [8] H.H. Gutbrod, A.M. Poskanzer, H.G. Ritter, Rep. Prog. Phys. 52 (1989) 1267.
- [9] A. Gobbi, FOPI Collaboration, Nucl. Instr. and Meth. A 324 (1993) 156.
- [10] G. Poggi, G. Pasquali, M. Bini, P.R. Maurenzig, A. Olmi, B. Taccetti, Nucl. Instr. and Meth. A 324 (1993) 177.
- [11] D. H. E. Gross, Rep. Prog. Phys. 53 (1990) 605.
- [12] L.G. Moretto and G.J. Wozniak, Annu. Rev. Nucl. Part. Sci. 43 (1993) 379.
- [13] Proc. of the XXII Int. Workshop on Gross Properties of Nuclei and Nuclear Excitations, Hirschegg, Austria, 1994, ed. H. Feldmeier (GSI, Darmstadt, 1994).
- [14] J.P. Bondorf, A.S. Botvina, A.S. Iljinov, I.N. Mishustin, K. Sneppen, Phys. Rep. 257 (1995) 133; we thank A. Botvina for making the code SMM available to us.
- [15] K.G.R. Doss, H.-A. Gustafsson, H. Gutbrod, J.W. Harris, B.V. Jacak, K.-H. Kampert, B. Kolb, A.M. Poskanzer, H.-G. Ritter, H.R. Schmidt, L. Teitelbaum, M. Tincknell, S. Weiss and H. Wieman, Phys. Rev. Lett. 59 (1987) 2720.
- [16] L.P. Csernai, H. Stöcker, P.R. Subramanian, G. Graebner, A. Rosenhauer, G. Buchwald, J.A. Maruhn and W. Greiner, Phys. Rev. C 28 (1983) 2001.
- [17] J.P. Alard, FOPI Collaboration, Phys. Rev. Lett. 69 (1992) 889.
- [18] C. Kuhn, FOPI Collaboration, Phys. Rev. C 48 (1993) 1232.
- [19] M.B. Tsang et al., Phys. Rev. Lett. 71 (1993) 1502.
- [20] S.C. Jeong, FOPI Collaboration, Phys. Rev. Lett. 72 (1994) 3468.
- [21] W.C.Hsi *et al.*, Phys. Rev. Lett. 73 (1994) 3367.

- [22] M. Petrovici, FOPI Collaboration, Phys. Rev. Lett. 74 (1995) 5001.
- [23] M. Dželalija, FOPI Collaboration, Phys. Rev. C 52 (1995) 346.
- [24] R. Kotte, FOPI Collaboration, Phys. Rev. C 51 (1995) 2686.
- [25] V. Ramillien, FOPI Collaboration, Nucl. Phys. A 587 (1995) 802.
- [26] G. Poggi, FOPI Collaboration, Nucl. Phys. A 586 (1995) 755.
- [27] G. J. Kunde *et al.*, Phys. Rev. Lett. 74 (1995) 38.
- [28] M.A. Lisa, EOS Collaboration, Phys. Rev. Lett. 75 (1995) 2662.
- [29] M.D. Partlan, EOS Collaboration, Phys. Rev. Lett. 75 (1995) 2100.
- [30] S. Wang, EOS Collaboration, Phys. Rev. Lett. 74 (1995) 2646.
- [31] S. Wang, EOS Collaboration, Phys. Rev. Lett. 76 (1996) 3911.
- [32] H. Stöcker, J.A. Maruhn, W. Greiner, Phys. Rev. Lett. 44 (1980) 725.
- [33] H.Å. Gustafsson, H.H. Gutbrod, B. Kolb, H. Löhner, B. Ludewigt, A. M. Poskanzer, T. Renner, H. Riedesel, H.G. Ritter, A. Warwick, F. Weik, and H. Wieman, Phys. Rev. Lett. 52 (1984) 1590.
- [34] R.E. Renfordt, D. Schall, R. Bock, R. Brockmann, J.W. Harris, A. Sandoval, R. Stock, H. Ströbele, D. Bangert, W. Rauch, G. Odyniec, H.G. Pugh, and L.S. Schroeder, Phys. Rev. Lett. 53 (1984) 763.
- [35] J. P. Bondorf, S.I.A. Garpman, J. Zimanyi, Nucl. Phys. A 296 (1978) 320.
- [36] P.J. Siemens and J.O. Rasmussen, Phys. Rev. Lett. 42 (1979) 880.
- [37] H.W. Barz, J.P. Bondorf, R. Donangelo, R. Elmer, F.S. Hansen, B. Jakobsson, L. Karlsson, H. Nifenecker, H. Schulz, F. Schussler, K. Sneppen and K. Söderström, Nucl. Phys. A 531 (1991) 453.
- [38] W. Bauer, J.P. Bondorf, R. Donangelo, R. Elmer, B. Jakobsson, H. Schulz, F. Schussler and K. Sneppen, Phys. Rev. C 47 (1993) R1838.
- [39] A.Z. Mekjian, Phys. Rev. C 17 (1978) 1051.
- [40] W. Reisdorf, in Proc. of the XXII Int. Workshop on Gross Properties of Nuclei and Nuclear Excitations, Hirschegg, Austria, 1994, ed. H. Feldmeier and W. Nörenberg (GSI, Darmstadt, 1994) p.93.
- [41] W. Reisdorf, Acta Phys. Pol. B 25 (1994) 443.
- [42] P. Braun-Munzinger, J. Stachel, J.P. Wessels, N. Xu, Phys. Lett. B 344 (1995) 43; Phys. Lett. B 365 (1996) 1.
- [43] J. Aichelin and H. Stöcker, Phys. Lett. B 176 (1986) 14; J. Aichelin, Phys. Rep. 202 (1991) 233.
- [44] J. Blocki, J. Randrup, W.J. Swiatecki, C.F. Tsang, Ann. Phys. 104 (1977) 427.

- [45] P. Danielewicz, Phys. Rev. C 51 (1995) 716.
- [46] W. Reisdorf, in Proc. of the XX Int. Workshop on Gross Properties of Nuclei and Nuclear Excitations, Hirschegg, Austria, 1992, ed. H. Feldmeier (GSI, Darmstadt, 1992) p.38.
- [47] W. Scheid, H. Müller, and W. Greiner, Phys. Rev. Lett. 32 (1974) 741.
- [48] M.I. Sobel, P.J. Siemens, J.P. Bondorf, H.A. Bethe, Nucl. Phys. A 251 (1975) 502.
- [49] P. Danielewicz and G. Odyniec, Phys. Lett. B 157 (1985) 146.
- [50] H. Stöcker, L.P. Csernai, G. Graebner, G. Buchwald, H. Kruse, R.Y. Cusson, J.A. Maruhn, W. Greiner, Phys. Rev. 25 (1982) 1873.
- [51] C. Roy, FOPI Collaboration, to be published (1996).
- [52] P. Beckmann, H.A. Gustafsson, H.H. Gutbrod, K.-H. Kampert, B. Kolb, H. Loehner, A.M. Poskanzer, H.G. Ritter, H.R. Schmidt and T. Siemiarczuk, Mod. Phys. Lett. A 2 (1987) 163; R. Bock et al., Mod. Phys. Lett. A 2 (1987) 721.
- [53] Th. Wienold, Ph. D. thesis, University Heidelberg, GSI Report no. 93-28 (1993); Th. Wienold, FOPI Collaboration, GSI, preprint GSI-94-74 (1994).
- [54] A. Del Zoppo, R. Alba, C. Agodi, G. Bellia, R. Coniglione, P. Finocchiaro, K. Loukachine, C. Maiolino, E. Migneco, A. Peghaire, P. Piattelli, D. Santonocito, P. Sapienza, Phys. Rev. Lett. 75 (1995) 2288.
- [55] C. Hartnack, Ph. D. thesis, University Frankfurt, GSI Report no. 93-5 (1993).
- [56] S.A. Bass, C. Hartnack, H. Stöcker, W. Greiner, Phys. Rev. C 51 (1995) 3343.
- [57] W.U. Schroeder, J.R. Huizenga, Treatise on Heavy Ion Science, ed. D. A. Bromley, Vol. 2 (Plenum New York, 1984) p. 115.
- [58] R. Bougault et al., Nucl. Phys. A 587 (1995) 499.
- [59] B. M. Quednau, S. P. Baldwin, B. Lott, W. U. Schroeder, B. M. Szabo, J. Töke, D. Hilscher, U. Jahnke, H. Rossner, S. Bresson, J. Galin, D. Guerreau, M. Morjean, D. Jacquet, Phys. Lett. B 309 (1993) 10.
- [60] W.J. Swiatecki, Phys. Scr. 24 (1981) 113; Nucl. Phys. A 376 (1982) 275.
- [61] H. Feldmeier, Rep. Prog. Phys. 50 (1987) 915.
- [62] J. Konopka, Ph. D. thesis, University Frankfurt, (1995); J. Konopka, H. Stöcker, and W. Greiner, GSI Scientific Report 1994, GSI 94-1 (1995) 63.
- [63] B. Heide and H.W. Barz, Nucl. Phys. A 588 (1995) 918.
- [64] B. Heide and H.W. Barz, Nucl. Phys. A 591 (1995) 755.
- [65] F. Cooper and G. Frye, Phys. Rev. D 10 (1974) 186.
- [66] W. Neubert, A. V. Botvina, FOPI Collaboration, in preparation.

- [67] L.I.Sedov, *Similarity and Dimensional Methods in Mechanics*, (Gostekhizdat, Moscow, 1957), 4th. ed., English translation edited by M. Holt (Academic Press, New York, 1959).
- [68] S. Hölbling for the FOPI Collaboration; program F1F1F1, available on request.
- [69] K.G.R. Doss, et al., *Mod. Phys. Lett. A* 3 (1988) 849.
- [70] J. Randrup, *Comp. Phys. Comm.* 77 (1993) 153.
- [71] P. Danielewicz and Q. Pan, *Phys. Rev. C* 46 (1992) 2002.
- [72] M. D’Agostino, Multics/Miniball Collaboration, *Phys. Lett. B* 368 (1996) 259.
- [73] J.P. Bondorf, D. Idier, I.N. Mishustin, *Phys. Lett. B* 359 (1995) 261.
- [74] H. H. Gutbrod, A.I. Warwick, H. Wieman, *Nucl. Phys. A* 387 (1982) 177c.
- [75] D. L’Hôte, talk at 5th Gull Lake Nuclear Physics Conf., MI, 1988; J.Gosset et al., *The Nuclear Equation of State*, ed. W. Greiner and H. Stöcker, NATO-ASI Vol. B 216 part A (Plenum, New York 1989) p. 87.
- [76] H.H. Gutbrod, K.H. Kampert, B.Kolb, A.M. Poskanzer, H.G. Ritter, R. Schicker and H.R. Schmidt, *Phys. Lett. B* 216 (1989) 267.
- [77] H.H. Gutbrod, K.H. Kampert, B. Kolb, A.M. Poskanzer, H.G. Ritter, R. Schicker and H.R. Schmidt, *Phys. Rev. C* 42 (1990) 640.
- [78] J. Konopka, H. Stöcker, W. Greiner, in *Proc. of the XXII Int.Workshop on Gross Properties of Nuclei and Nuclear Excitations*, Hirschegg, Austria, 1994, ed. H. Feldmeier (GSI, Darmstadt, 1994) p.218.
- [79] D. Lambrecht, LAND Collaboration, *Z. Phys. A* 350 (1994) 115.
- [80] N. Bastid, FOPI Collaboration, to be published
- [81] D. Hahn, H. Stöcker, *Phys. Rev. C* 37 (1988) 1048.
- [82] J. Konopka, H. Graf, H. Stöcker, W. Greiner, *Phys. Rev. C* 50 (1994) 2085; we thank J.Konopka for making the results of QSM available to us.
- [83] G. Fai, J. Randrup, *Comp. Phys. Comm.* 42 (1986) 385.
- [84] D.R. Tilley, H.R. Weller, C.M. Cheves, *Nucl. Phys. A* 565 (1993) 1.
- [85] L.P. Csernai, J.I. Kapusta, G. Fai, D. Hahn, J. Randrup, H. Stöcker, *Phys. Rev. C* 35 (1987) 1297.
- [86] N. Levinson, K. Dan. Vidensk. Scisk, *Mat.-Fys. Medd.* 25 (1949) No. 9.
- [87] G. Fai, J. Randrup, *Nucl. Phys. A* 381 (1982) 557.
- [88] C. Dorso, J. Randrup, *Phys. Lett. B* 301 (1993) 328.
- [89] R. K. Puri, C. Hartnack, J. Aichelin, *Phys. Rev. C* 54 (1996) 1.

- [90] H. Müller and B.D. Serot, Phys. Rev. C 52 (1995) 2073.
- [91] G. Peilert, J. Konopka, M. Blann, M.G. Mustafa, H. Stöcker and W. Greiner, Phys. Rev. C 46 (1992) 1457.
- [92] C. Hartnack, J. Jaenicke, L. Sehn, H. Stöcker, J. Aichelin, Nucl. Phys. A 580 (1994) 643.
- [93] J.P. Blaizot, J.P. Berger, J. Dechargé, M. Girod, Nucl. Phys. A 591 (1995) 435.
- [94] D.H. Youngblood, H.L. Clark, Y.-W. Lui, Phys. Rev. Lett. 76 (1996) 1429.
- [95] G.F. Bertsch and S. Das Gupta, Phys. Rep. 160 (1988) 189.
- [96] C. Hartnack, R.K. Puri, J. Aichelin, S.A. Bass, J. Konopka, G. Peilert, H. Stöcker, W. Greiner, private communication, and to be published (1996).
- [97] P. Danielewicz, private communication (1996).
- [98] A.S. Botvina, A.B. Larionov, I.N. Mishustin, Yad. Fiz. 58(1995) 1703.
- [99] N.L. Balazs, B. Schürmann, K. Dietrich, L.P. Csernai, Nucl. Phys. A 424 (1984) 605.
- [100] A. Bonasera, L.P. Csernai, Phys. Rev. Lett. 59 (1987) 630; A. Bonasera, L.P. Csernai, B. Schürmann, Nucl. Phys. A 476 (1988) 159.
- [101] D. Krofcheck, W. Bauer, G.M. Crawley, C. Djalali, S. Howden, C.A. Ogilvie, A. Vander Molen, G.D. Westfall, W.K. Wilson, R.S. Tickle and C. Gale, Phys. Rev. Lett. 63 (1989) 2028.
- [102] C.A. Ogilvie, W. Bauer, D.A. Cebra, J. Clayton, S. Howden, J. Karn, A. Nadasen, A. Vander Molen, G.D. Westfall, W.K. Wilson and J.S. Winfield, Phys. Rev. C 42 (1990) R10.
- [103] S. Soff, S. Bass, Ch. Hartnack, H. Stöcker, W. Greiner, Phys. Rev. C 51 (1995) 3320.
- [104] W. M. Zhang, R. Madey, M. Elaasar, J. Schambach, D. Keane, B. D. Anderson, A.R. Baldwin, J. Cogar, J.W. Watson, G.D. Westfall, G. Krebs, H. Wieman, Phys. Rev. C 42 (1990) R491.
- [105] R. Donà, FOPI Collaboration, to be published (1996).
- [106] H. Feldmeier, Nucl. Phys. A 514 (1990) 322.
- [107] A. Ono, H. Horiuchi, T. Maruyama, A. Ohnishi, Phys. Rev. Lett. 68 (1992) 2898; Prog. Theor. Phys. 87 (1992) 1185.
- [108] R. Donangelo, H. Schulz, K. Sneppen, and S.R. Souza, Phys. Rev. C 50 (1994) R563.
- [109] A. Ono, H. Horiuchi, T. Maruyama, A. Ohnishi, Phys. Rev. C 47 (1993) 2652; A. Ono, H. Horiuchi, T. Maruyama, Phys. Rev. C 48 (1993) 2946.

- [110] D.E. Grady, J. Appl. Phys. 53 (1982) 322; J.A. Blink, W.G. Hoover, Phys. Rev. A 32 (1985) 1027; B.L. Holian and D.E. Grady, Phys. Rev. Lett. 60 (1988) 1355.
- [111] We thank B.Remaud for suggesting this possibility and directing our attention to the relevant literature.
- [112] H. Stöcker, M. Gyulassy and J. Boguta, Phys. Lett. B 103 (1981) 269.
- [113] H. Sorge, H. Stöcker and W. Greiner, Ann. Phys. 192 (1989) 266.
- [114] W. Cassing and U. Mosel, Prog. Part. Nucl. Phys. 25 (1990) 235.
- [115] Q. Li, J.Q. Wu and C.M. Ko, Phys. Rev. C 39 (1989) 849.
- [116] D.T. Khoa, N. Ohtsuka, M.A. Martin, A. Faessler, S.W. Huang, E. Lehmann and R.K.Puri, Nucl. Phys. A 548 (1992) 102.
- [117] C. Fuchs, E. Lehmann, R.K. Puri, L. Sehn, A. Faessler and H.H. Wolter, J. Phys. G. 22 (1996) 131.

Table 1
Summary of event samples

energy (MeV/A)	name	PM cut	ERAT cut	D cut	σ (mb)
150	PM200	PM > 36			215
	ERAT200		ERAT > 0.69		217
	ERAT200D		ERAT > 0.69	D < 0.24	82
	ERAT50		ERAT > 0.92		54
250	PM200	PM > 44			186
	ERAT200		ERAT > 0.68		197
	ERAT200D		ERAT > 0.68	D < 0.20	47
	ERAT50		ERAT > 0.93		49
400	PM200	PM > 53			191
	PM200D	PM > 53		D < 0.19	22
	ERAT200		ERAT > 0.66		188
	ERAT200D		ERAT > 0.66	D < 0.19	42
	ERAT50		ERAT > 0.88		47

Table 2
Limits imposed on the likelihood fits

Z	$y_{\text{lab}}^{\text{IW}}$	$\theta_{\text{cm}}^{\text{EW}}$	$\theta_{\text{cm}}^{\text{EW}}$	$\theta_{\text{cm}}^{\text{EW}}$
		150 A MeV	250 A MeV	400 A MeV
1	0.238	90	120	130
2	0.238	90	110	120
3	0.252	145	150	150
4	0.280	140	150	150
5	0.300	130	140	150
6	0.322	125	140	150
7	0.331	115	140	150
8	0.342	110	130	140
9	0.350	100	130	140
10	0.359	90	120	140

Table 3

Results from blast model fit

E/A	150	250	400	MeV/A (incident)
$\mathcal{E}_{\text{coll}}$	61.3 ± 7.0	61.3 ± 7.0	63.4 ± 7.0	% of TKE
E_{cm}/A	36.8	60.5	95.1	MeV/A
Q_{val}/A	-4.3	-5.0	-5.5	MeV/A
$\langle \beta_f \rangle$	0.204 ± 0.011	0.263 ± 0.014	0.334 ± 0.017	units of c
$\mathcal{E}_{\text{coll}}/A$	19.9 ± 2.3	34.0 ± 3.9	56.8 ± 6.3	MeV
$\mathcal{E}_{\text{th}}/A$	12.6 ± 2.3	21.5 ± 3.9	32.8 ± 6.3	MeV
T	17.2 ± 3.4	26.2 ± 5.1	36.7 ± 7.5	MeV
M	191 ± 11	208 ± 9	223 ± 6	includes neutrons
Z_{sum} error	-14%	-2%	+5%	extrapol. to 4π

Table 4

Multiplicities as function of the nuclear charge

Z	multiplicity			multiplicity			multiplicity		
	150 A MeV			250 A MeV			400 A MeV		
1	61.84	\pm	0.58	75.82	\pm	0.62	92.04	\pm	0.62
2	26.76	\pm	0.36	27.27	\pm	0.36	24.16	\pm	0.30
3	5.39	\pm	0.041	4.89	\pm	0.034	3.75	\pm	0.03
4	1.789	\pm	0.024	1.358	\pm	0.178	0.909	\pm	0.014
5	1.438	\pm	0.022	0.772	\pm	0.014	0.335	\pm	0.009
6	0.868	\pm	0.017	0.355	\pm	0.009	0.110	\pm	0.005
7	0.447	\pm	0.012	0.127	\pm	0.006	0.0397	\pm	0.0029
8	0.223	\pm	0.0087	0.0497	\pm	0.0035	0.0156	\pm	0.0018
9	0.0898	\pm	0.0057	0.0132	\pm	0.0018	0.0029	\pm	0.0008
10	0.0644	\pm	0.0049	0.0097	\pm	0.0015			
11	0.0231	\pm	0.0031	0.0025	\pm	0.0008			
12	0.0245	\pm	0.0033	0.0012	\pm	0.0006			

Table 5
Various multiplicities

	150 A MeV			250 A MeV			400 A MeV		
proton	26.1	±	1.4	31.9	±	1.6	38.7	±	2.0
deuteron	18.6	±	1.0	23.0	±	1.2	27.9	±	1.4
triton	17.2	±	0.9	21.0	±	1.1	25.5	±	1.3
^3He	5.7	±	0.3	9.1	±	0.5	10.6	±	0.6
^4He	21.0	±	1.1	18.2	±	1.0	13.6	±	0.7
neutron	92.6	±	10.8	97.9	±	8.2	101.7	±	6.2
charged p.	99.0	±	0.7	110.7	±	0.8	121.4	±	0.7
IMF	10.4	±	0.1	7.6	±	0.1	5.2	±	0.1

Table 6
Degrees of clusterization (%)

	150 A MeV			250 A MeV			400 A MeV		
protons in IMF	27.0	±	0.2	17.5	±	0.1	11.2	±	0.1
protons in clusters	83.5	±	1.5	79.8	±	1.8	75.5	±	2.0
nucleons in IMF	21.6	±	2.7	14.0	±	2.0	9.0	±	1.4
nucleons in clusters	69.9	±	11.8	67.1	±	9.5	64.4	±	7.8

Table 7
Collective energy from the IQMD model in percent of the total kinetic energy of emitted nucleons and clusters.

Row	specification				150 A MeV	250 A MeV	400 A MeV
1	$b < 1$	45° - 135°	HM	slope	21.6 ± 2.8	33.9 ± 1.7	42.1 ± 1.1
2	$b < 1$	45° - 135°	SM	slope	32.4 ± 2.6	38.9 ± 2.4	41.2 ± 1.7
3	$b < 1$	45° - 135°	SM	WS2	31.5 ± 0.9	38.3 ± 0.9	41.2 ± 0.7
4	$b < 1$	20° - 160°	SM	WS2	37.6 ± 0.6	40.1 ± 0.7	41.9 ± 0.4
5	$b < 1$	20° - 160°	SM	Box	36.9 ± 0.7	40.3 ± 0.8	43.8 ± 0.8
6	$b < 1$	20° - 160°	SM	Shell	30.2 ± 0.5	32.5 ± 0.5	35.5 ± 0.7
7	$b < 3$	45° - 135°	SM	WS2	31.1 ± 1.1	38.8 ± 1.2	42.4 ± 0.9
8	$b < 3$	20° - 160°	SM	WS2	40.9 ± 0.8	44.7 ± 0.6	46.1 ± 0.8

Fig. 1. Measured External Wall multiplicity (PM) distributions for Au on Au at three indicated energies.

Fig. 2. Measured distributions of the ratio of transverse to longitudinal kinetic energies (ERAT) for Au on Au at three indicated energies.

Fig. 3. Azimuthal angle distributions of intermediate mass fragments for multiplicity (PM) and transverse energy (ERAT) selections corresponding to the indicated geometrical cuts. The intensity ratios $R_\phi(0^\circ/180^\circ)$ obtained by least square fits (see text) are also indicated.

Fig. 4. Azimuthal asymmetry variation of intermediate mass fragments with multiplicity (upper abscissa) and with ERAT (lower abscissa, open squares). An additional constraint on the scaled rapidity, indicated in the figure, was applied.

Fig. 5. Directivity and in-plane flow for Au on Au at 250 A MeV. The upper panels show the directivity distribution (left) and the distribution of average in-plane transverse momenta for a cross section sample of 200 mb cut off from the tail of the ERAT distribution. An azimuthally randomized directivity distribution (open symbols) is also shown for comparison in the left panel. The lower panels show the corresponding variation of the first moments with the cross section interval (reduced to an effective impact parameter) obtained by binning with the multiplicity PM (open symbols) or with the ERAT (full symbols).

Fig. 6. Azimuthal asymmetry as function of the directivity cut for Au+Au events (250 A MeV) from the ERAT 200 mb sample.

Fig. 7. ERAT distributions (charged particles only) for central Au on Au collisions in 4π geometry at 250 A MeV. Histogram: isotropic blast model. Open square symbols: IQMD [55,56] prediction for the hard momentum-dependent equation of state. Full triangles: VUU calculation [71] with finite-number fluctuations added and with abscissa rescaled to give an average value of two.

Fig. 8. Invariant cross section $d^2\sigma/u_t du_t dy$ contour plots (scaled units) for Be ($Z=4$) fragments observed in the system Au+Au at 250 A MeV. Only the forward hemisphere was measured and the data were then reflected at midrapidity. The contours are separated by factors 1.5. The three panels from bottom to top are for the selections PM200, ERAT200 and ERAT200D.

Fig. 9. Invariant cross section $d^2\sigma/u_t du_t dy$ contour plots (scaled units) for Li ($Z=3$) fragments observed in the system Au+Au at 150, 250 and 400 A MeV for the selection ERAT200D. See text and the caption fig. 8 for further details.

Fig. 10. Invariant cross section $d^2\sigma/u_t du_t dy$ contour plots (scaled units) for Li ($Z=3$) fragments observed in the system Au+Au at 150, 250 and 400 A MeV for the selection PM200. See text and the caption fig. 8 for further details.

Fig. 11. Blast model spectra for a scenario with 50% collectivity. The spectra for three different flow-velocity profiles *Shell*, *Box*, *WS2*, explained in the text, are shown. Lower left panel: rapidity distribution for mass $A = 8$ fragments. Upper left panel: Same, but with a transverse 4-velocity cut $u_t < 0.6$. Upper right panel: same cut but for mass $A = 1$. Lower right panel: transverse 4-velocity spectrum for mass $A = 8$ with a rapidity cut $0 < y < 0.5$.

Fig. 12. Measured rapidity distributions of fragments with nuclear charge $Z=4$ (left) and $Z=5$ or 6 (right) at 250 A MeV incident energy. The data (symbols) are compared with the global fits using the blast model with flow profiles *Shell* (bottom), *Box* (middle) and *WS2* (top). A transverse 4-velocity cut $u_t < 0.6$ was done. Only the forward-hemisphere contribution was measured, the backward contribution is obtained by reflection.

Fig. 13. Measured charge-separated rapidity distributions for Au+Au at 150 A MeV. The various nuclear charges are given in the figure. The smooth curves are blast model fits with the profile WS2.

Fig. 14. Same as Fig. 13, but at 400 A MeV incident energy.

Fig. 15. Average kinetic energy as function of mass in the polar angle range $25-45^\circ$ for the three indicated energies. Open symbols: selection ERAT200D; full triangles: selection ERAT50. The solid lines are blast model fits with the velocity profile WS2. The dashed line holds for profile *Box*, the dotted line for profile *Shell*, both shown only for 250 A MeV.

Fig. 16. Variation of the deduced collectivity with increasingly dilute flow profiles.

Fig. 17. Average kinetic energies for hydrogen and helium isotopes at polar angles $60-90^\circ$. The data are from ref. [26]. The solid line represents the mass dependence inferred from the global fit of the blast model with velocity profile WS2.

Fig. 18. Kinetic energy spectra at center-of-mass polar angles $(25-45)^\circ$ for fragments with nuclear charge $Z=1, 2(\times 0.1), 3(\times 0.01), 4(\times 0.001),$ and $5+6(\times 0.0001)$. The system is Au+Au at 250 A MeV, the event sample is ERAT200D. The smooth curves are blast model descriptions.

Fig. 19. Kinetic energy spectra of light charged particles (indicated in the figure) at polar angles $(60 - 90)^\circ$ for Au on Au at 250 A MeV. The data (symbols) are from reference [26], the smooth curves are predictions of the blast model. The event sample is approximately ERAT200.

Fig. 20. Invariant transverse four-velocity spectra for Au on Au at 150 (left panels) and 400 A MeV for fragments with nuclear charges $Z=1, 2, 3$ and 4 (bottom to top). The spectra are shown for two indicated rapidity intervals. The data are represented by symbols, smooth curves were calculated with the blast model. The event sample is ERAT200D.

Fig. 21. Polar angular distributions for Au on Au at 400 A MeV for fragments with nuclear charges $Z=1$ to 6. The smooth curves are blast model calculations. The deviations from a flat distribution in the model are due to the apparatus filter. The event sample is ERAT200D.

Fig. 22. Polar angular distributions of intermediate mass fragments for Au on Au at 400 A MeV. A scaled four-velocity cut $u < 0.5$ is applied. The distributions are shown for various indicated event samples.

Fig. 23. Measured multiplicities for Au on Au at 250 A MeV as function of nuclear charge for various event selections described in the text.

Fig. 24. Measured 4π -integrated multiplicities for Au on Au at 150, 250 and 400 A MeV as function of nuclear charge. The straight lines are exponential fits excluding $Z=1, 2$ and 4 fragments.

Fig. 25. Clusterization in experiment (EXP) and theory (IQMD) versus incident energy. Left panel: IMF multiplicity in 4π geometry. Right panel: percent of protons bound in any cluster (left ordinate, EXP and IQMD) and protons bound in IMF's (right ordinate, triangles, EXP only). In both panels the height of the hatched area indicates the span when switching from soft (higher values) to hard EOS.

Fig. 26. Fluctuations and correlations of multiplicities. The histograms are measurements, the crosses are blast model simulations. Lower left panel: External Wall multiplicity (M) distribution. Upper left panel: IMF multiplicity distribution. Lower right panel: average IMF multiplicity versus light-particle multiplicity.

Fig. 27. Comparison of measured (FOPI) charged particle multiplicities with calculations using three different statistical models, QSM, WIX, SMMM for three indicated incident energies. The predictions of IQMD (SM) are indicated as dashed lines. The upper right panel gives the ratio of measured oxygen yields to predictions of the QSM (triangles joined by solid lines). The dotted line in the panel is a calculation for the maximum collective energy allowed by the blast model fits.

Fig. 28. Left panel: measured (crosses) charged particle multiplicities at 250 A MeV (together with the exponential fit to guide the eye) and various calculations with the code WIX. Full squares: $C_{\text{cut}} = 2$, open squares: $C_{\text{cut}} = 8$, open circles: $C_{\text{cut}} = 8$ and no evaporation. Right panel: known level distribution for ^{16}O (histogram), left (right) arrow: average excitation energy of ^{16}O predicted by WIX for $C_{\text{cut}} = 2$ (8).

Fig. 29. Variation of the average value of ERAT with incident energy in the IQMD model. The dependences are shown for the hard (*HM*) and the soft (*SM*) momentum dependent EOS. The Au on Au collisions are restricted to impact parameters < 1 fm. ERAT is calculated from charged particles only, but using full 4π geometry.

Fig. 30. ERAT for Au on Au at 250 A MeV. Top panel: predicted dependence on the impact parameter in 4π geometry, using charged particles only. Two different codes, VUU [71] and IQMD [55] were used. The solid (dashed) curves are for the hard (soft) EOS. Bottom panel: measured ERAT distribution (histogram) and filtered theoretical simulations. Triangles: Blast Model normalized to 31 mb ($b \leq 1$ fm). Open circles: IQMD hard momentum dependent EOS. The other symbols are for the VUU calculation with hard (H) or soft (S) EOS.

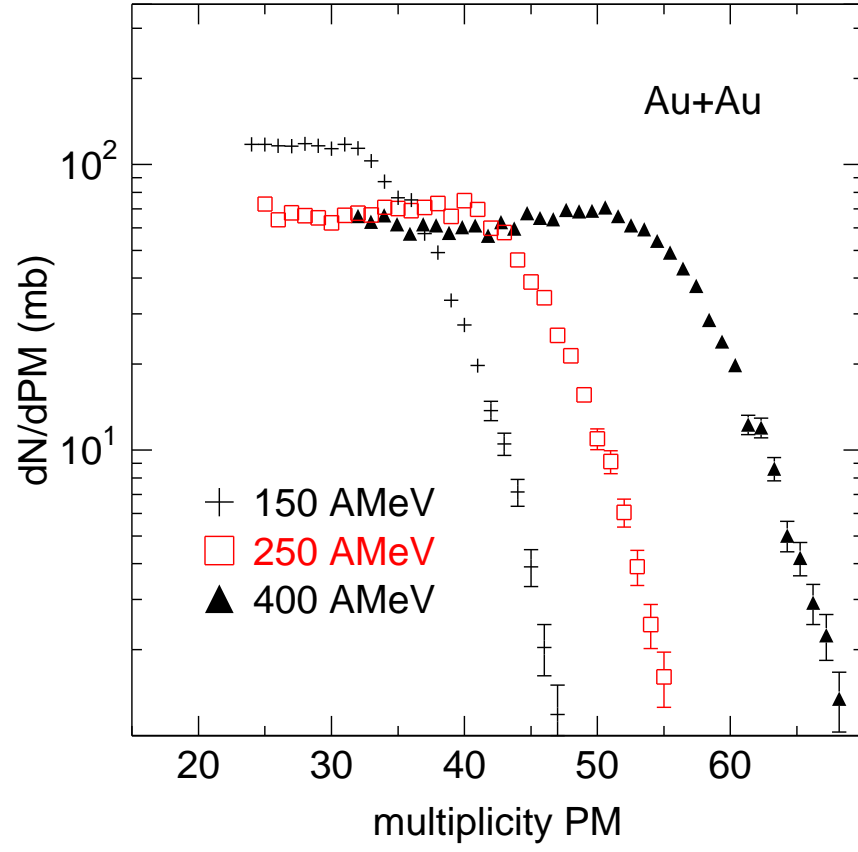
Fig. 31. Scaled sideflow in semicentral Au on Au collisions. Lower panel: filtered IQMD calculations for p_x^{dir} with the soft momentum-dependent EOS (SM) and for 400 A MeV incident energy. Solid curve: binning with the true impact parameter. Squares: binning with ERAT. Dotted: binning with PM. Crosses: binning with ERAT, but for 150 A MeV incident energy. Middle panel: FOPI data for p_x^{dir} binned with ERAT and for the three indicated energies. Upper panel: same as middle panel, but for the alternate sideflow observable F_{DO} .

Fig. 32. Comparison of the centrality dependence of the IMF multiplicity in experiment (triangles) and theory. Open symbols: multiplicity binning, closed symbols: ERAT binning, crosses: impact parameter binning.

Fig. 33. Equation of state and impact parameter dependence of the degree of clusterization in the IQMD simulation. Lower panel: IMF multiplicity, upper panel: He/H ratio. S (H) stands for soft (hard) EOS, M indicates inclusion of momentum dependence. The curves are to guide the eye. For comparison, the experimental He/H ratio for central collisions is 0.26. All data are for Au on Au at 400 A MeV.

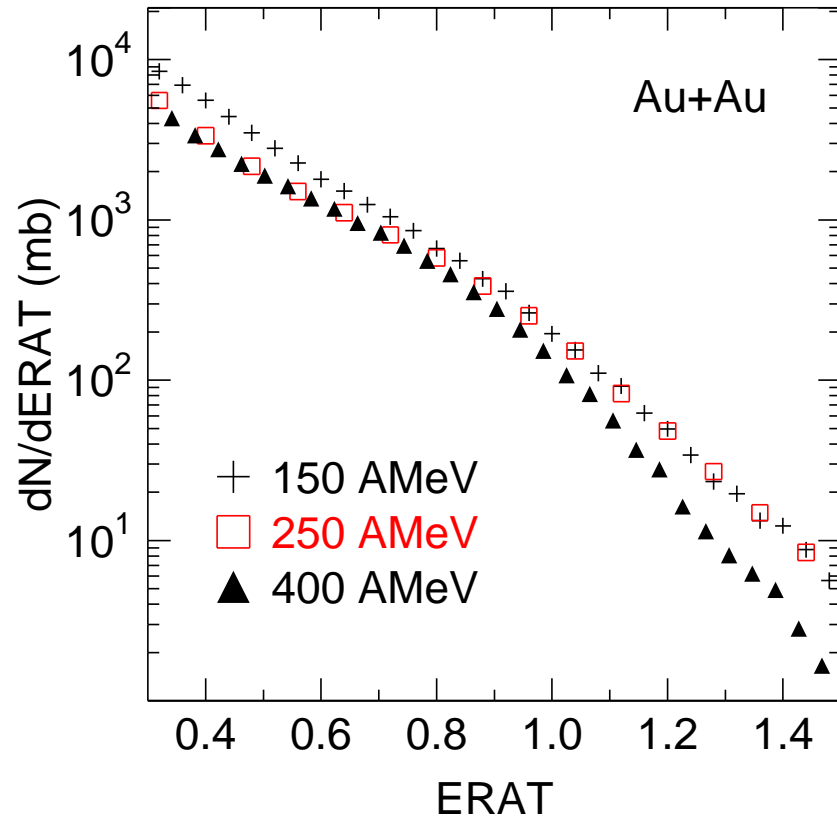
Fig. 34. IQMD predictions (soft momentum dependent EOS) for average kinetic energies as function of mass. The straight lines are linear least squares fits in the mass range $A = 1 - 10$. The simulations are for Au on Au collisions at 150 (left) and 400 (right) A MeV with impact parameters up to 1 fm and for particles emitted with polar angles $45 - 135^\circ$.

FIG.1 Measured External Wall multiplicity (PM) distributions for Au on Au at three indicated energies.



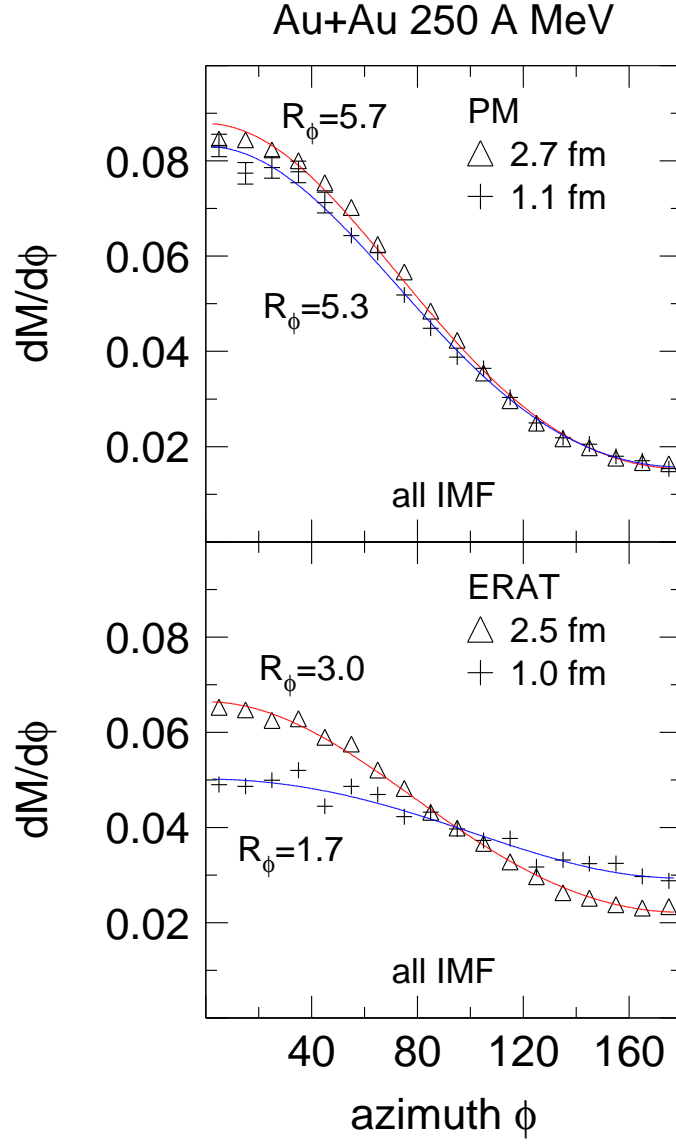
imggloba.data

FIG.2 Measured distributions of the ratio of transverse to longitudinal kinetic energies (ERAT) for Au on Au at three indicated energies.



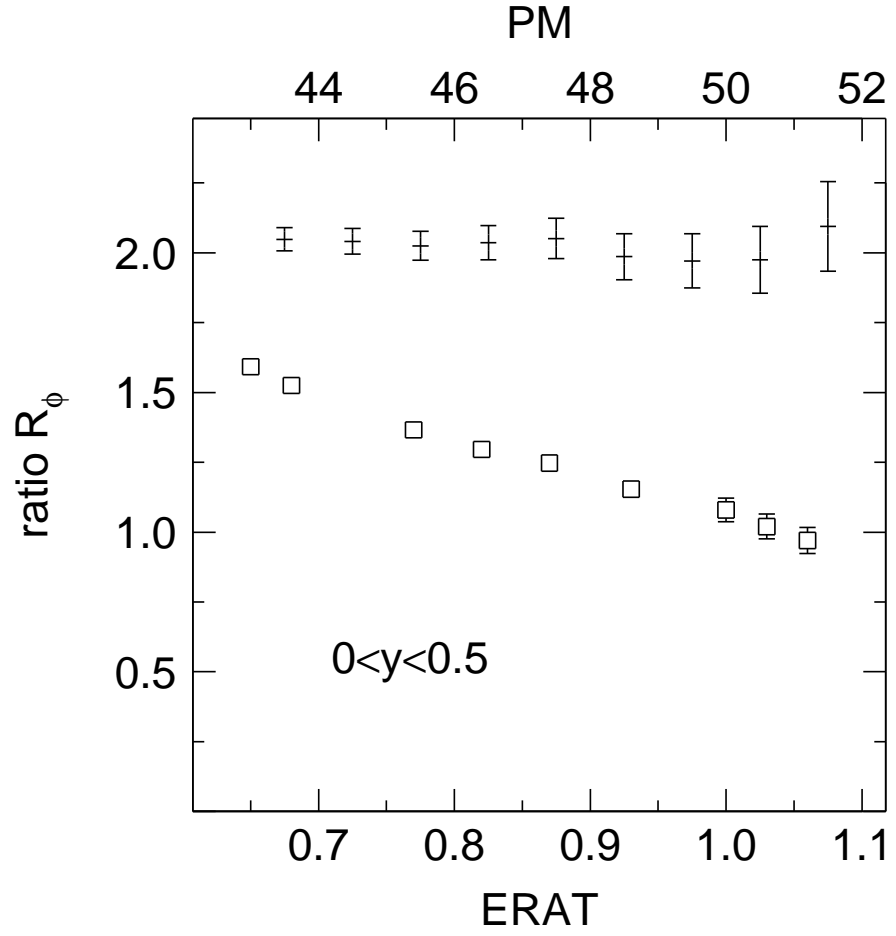
erats.data

FIG.3 Azimuthal angle distributions of intermediate mass fragments for multiplicity (PM) and transverse energy (ERAT) selections corresponding to the indicated geometrical cuts. The intensity ratios $R_\phi(0^\circ/180^\circ)$ obtained by least square fits (see text) are also indicated.



imfphia250.data

FIG.4 Azimuthal asymmetry variation of intermediate mass fragments with multiplicity (upper abscissa) and with ERAT (lower abscissa, open squares). An additional constraint on the scaled rapidity, indicated in the figure, was applied.



imfphia250.data

FIG.5 Directivity and in-plane flow for Au on Au at 250 A MeV. The upper panels show the directivity distribution (left) and the distribution of average in-plane transverse momenta for a cross section sample of 200 mb cut off from the tail of the ERAT distribution. An azimuthally randomized directivity distribution (open symbols) is also shown for comparison in the left panel. The lower panels show the corresponding variation of the first moments with the cross section interval (reduced to an effective impact parameter) obtained by binning with the multiplicity PM (open symbols) or with the ERAT (full symbols).

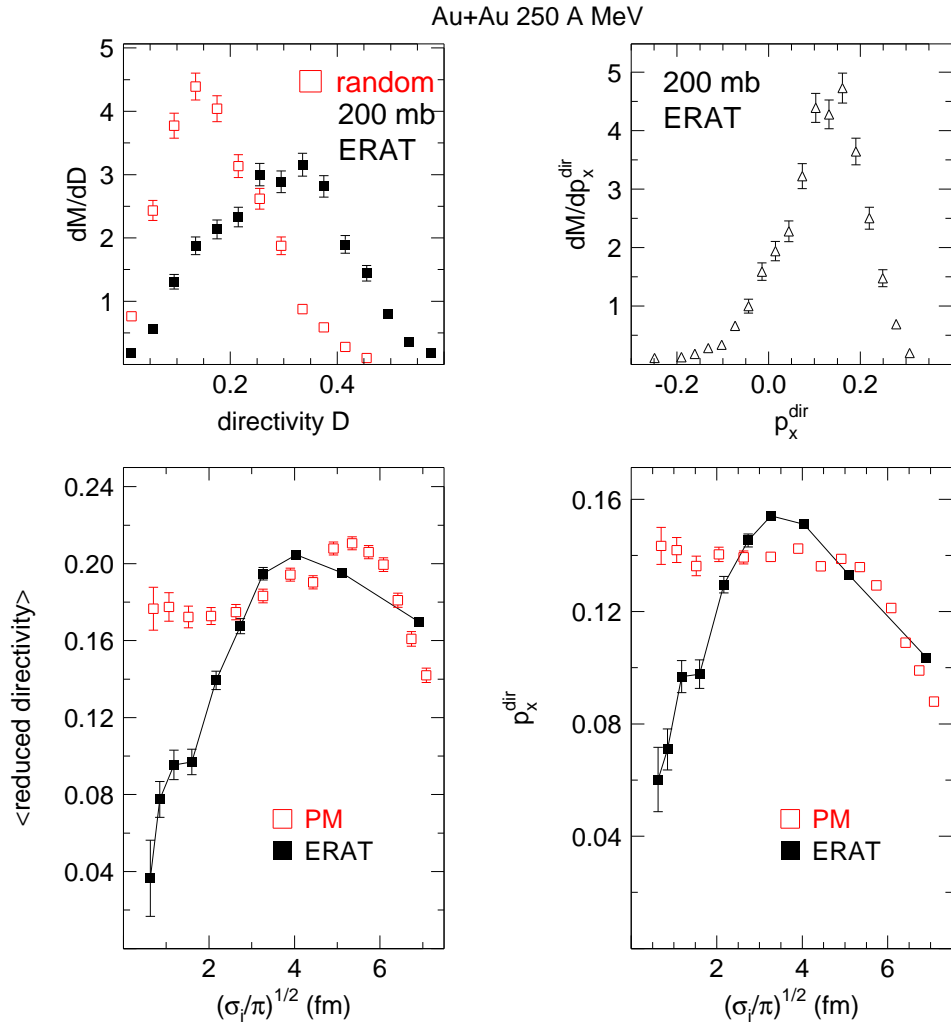
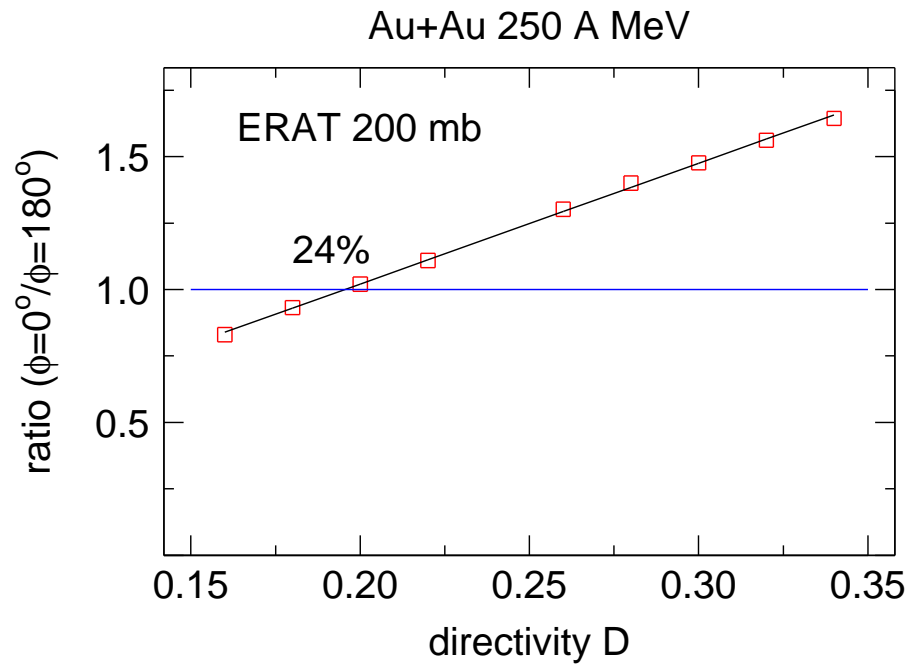
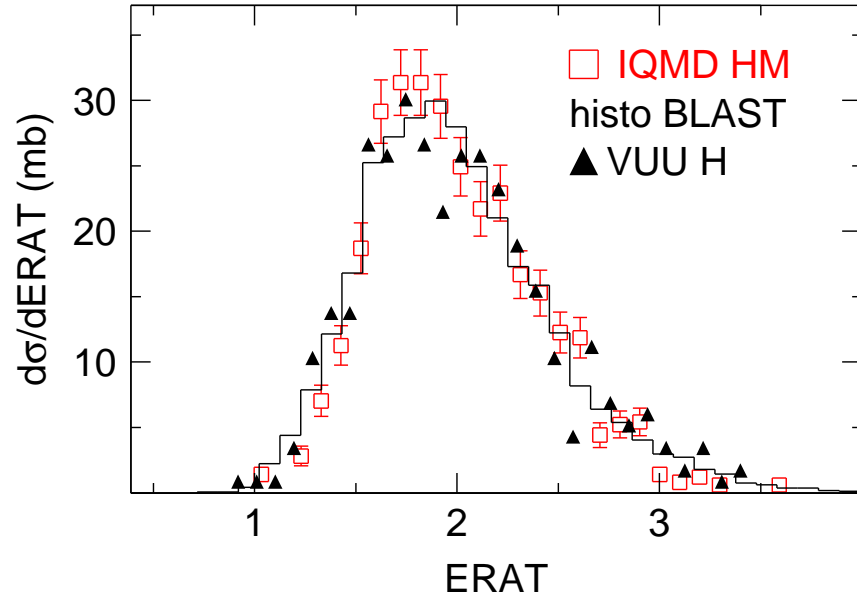


FIG.6 Azimuthal asymmetry as function of the directivity cut for Au+Au events (250 A MeV) from the ERAT 200 mb sample.



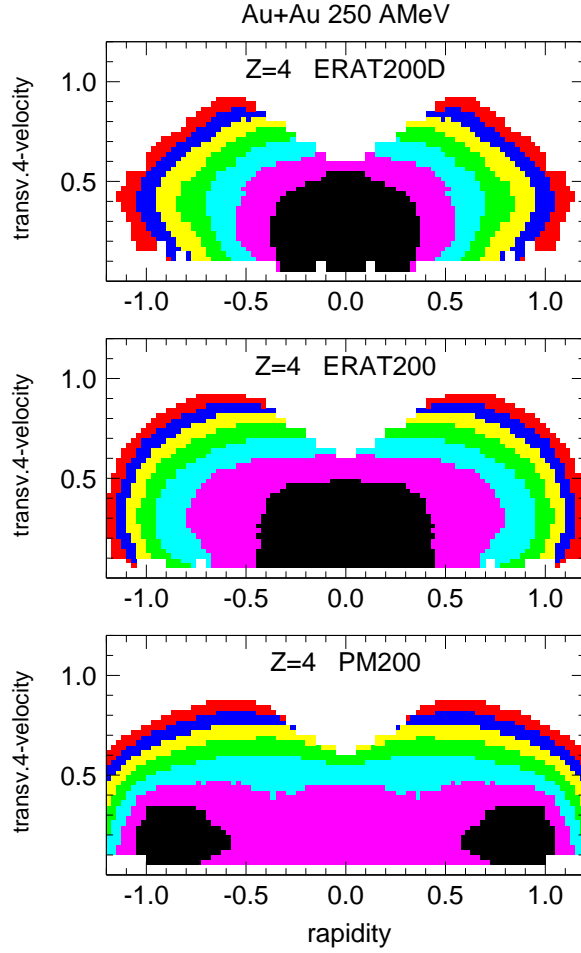
imfphia250.data

FIG.7 ERAT distributions (charged particles only) for central Au on Au collisions in 4π geometry at 250 A MeV. Histogram: isotropic blast model. Open square symbols: IQMD [55,56] prediction for the hard momentum-dependent equation of state. Full triangles: VUU calculation [71] with finite-number fluctuations added and with abscissa rescaled to give an average value of two.



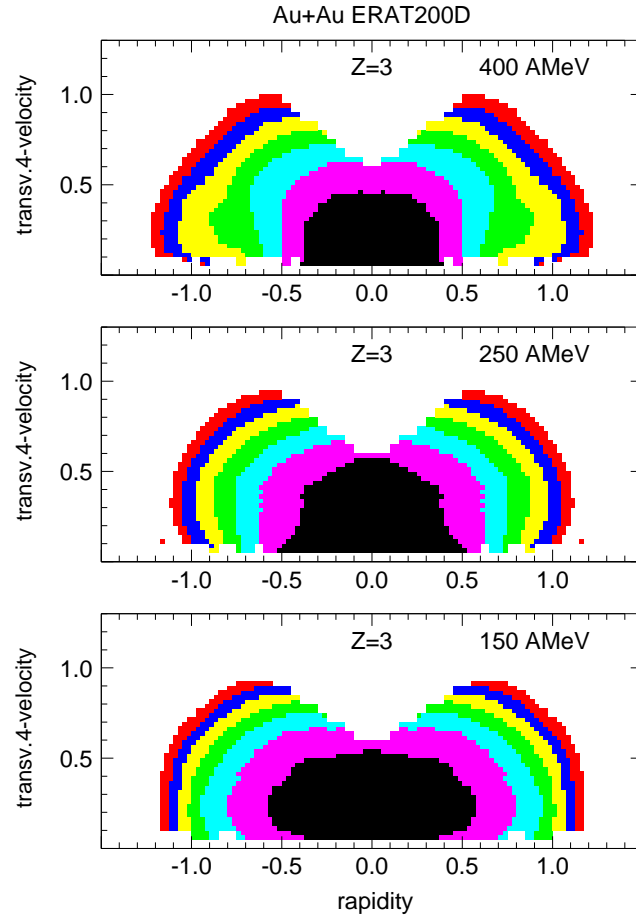
qmdglob250.data

FIG.8 Invariant cross section $d^2\sigma/u_t du_t dy$ contour plots (scaled units) for Be ($Z=4$) fragments observed in the system Au+Au at 250 A MeV. Only the forward hemisphere was measured and the data were then reflected at midrapidity. The contours are separated by factors 1.5. The three panels from bottom to top are for the selections PM200, ERAT200 and ERAT200D.



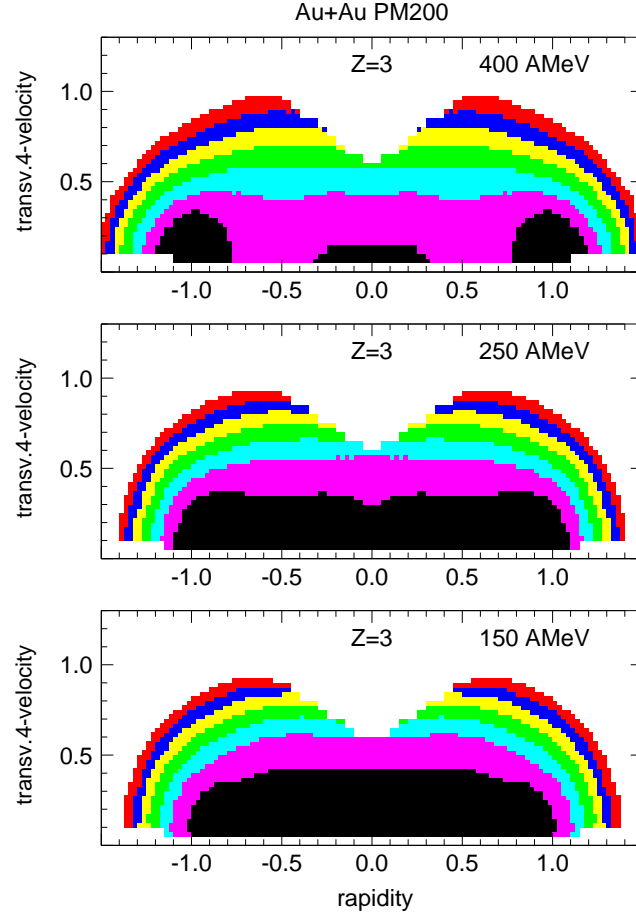
imfptyc.kumac

FIG.9 Invariant cross section $d^2\sigma/u_t du_t dy$ contour plots (scaled units) for Li ($Z=3$) fragments observed in the system Au+Au at 150, 250 and 400 A MeV for the selection ERAT200D. See text and the caption fig. 8 for further details.



imfptye.kumac

FIG.10 Invariant cross section $d^2\sigma/u_t du_t dy$ contour plots (scaled units) for Li ($Z=3$) fragments observed in the system Au+Au at 150, 250 and 400 A MeV for the selection PM200. See text and the caption fig. 8 for further details.



imfptye.kumac

FIG.11 Blast model spectra for a scenario with 50% collectivity. The spectra for three different flow-velocity profiles Shell, Box, WS2, explained in the text, are shown. Lower left panel: rapidity distribution for mass $A = 8$ fragments. Upper left panel: Same, but with a transverse 4-velocity cut $u_t < 0.6$. Upper right panel: same cut but for mass $A = 1$. Lower right panel: transverse 4-velocity spectrum for mass $A = 8$ with a rapidity cut $0 < y < 0.5$.

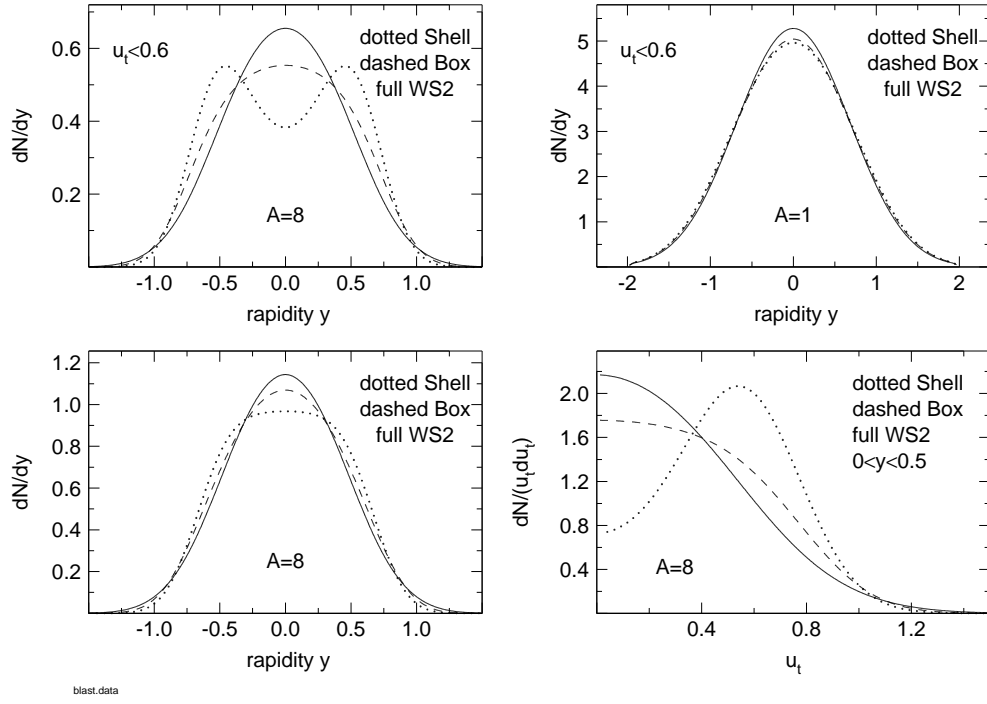


FIG.12 Measured rapidity distributions of fragments with nuclear charge $Z=4$ (left) and $Z=5$ or 6 (right) at 250 A MeV incident energy. The data (symbols) are compared with the global fits using the blast model with flow profiles *Shell* (bottom), *Box* (middle) and *WS2* (top). A transverse 4-velocity cut $u_t < 0.6$ was done. Only the forward-hemisphere contribution was measured, the backward contribution is obtained by reflection.

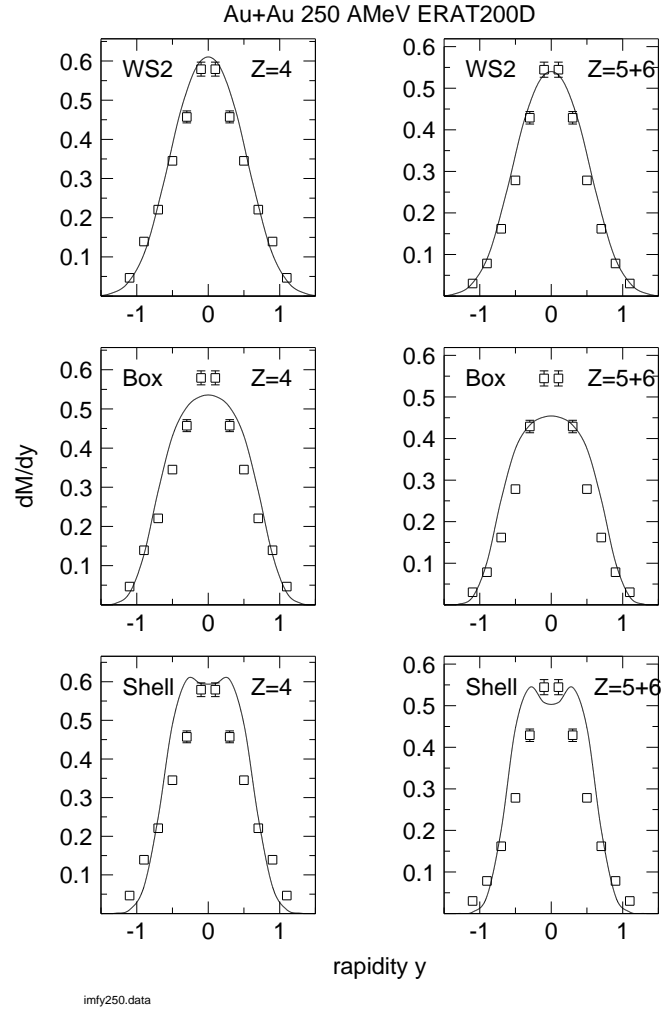


FIG.13 Measured charge-separated rapidity distributions for Au+Au at 150 A MeV. The various nuclear charges are given in the figure. The smooth curves are blast model fits with the profile WS2.

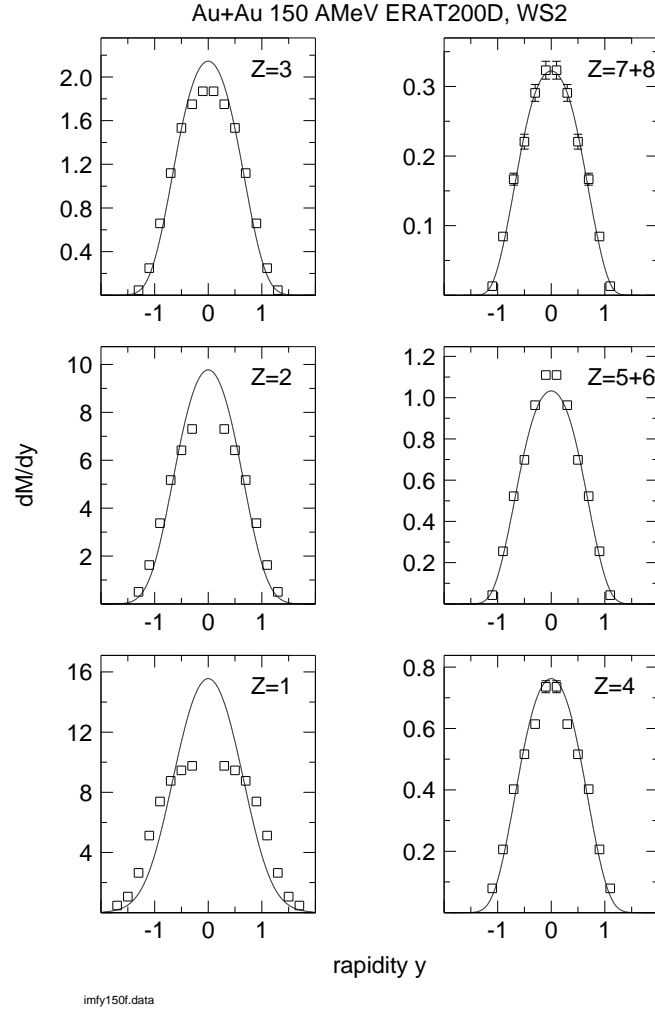


FIG.14 Same as Fig.13, but at 400 A MeV incident energy.

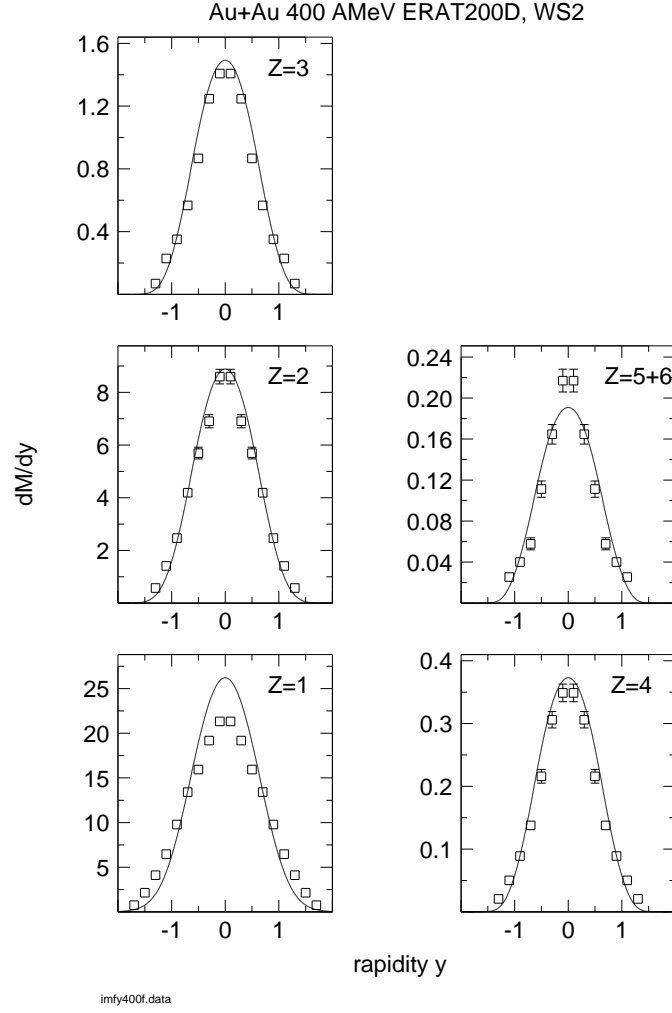


FIG.15 Average kinetic energy as function of mass in ther polar angle range $25 - 45^\circ$ for the three indicated energies. Open symbols: selection ERAT200D; full triangles: selection ERAT50. The solid lines are blast model fits with the velocity profile *WS2*. The dashed line holds for profile *Box*, the dotted line for profile *Shell*, both shown only for 250 A MeV.

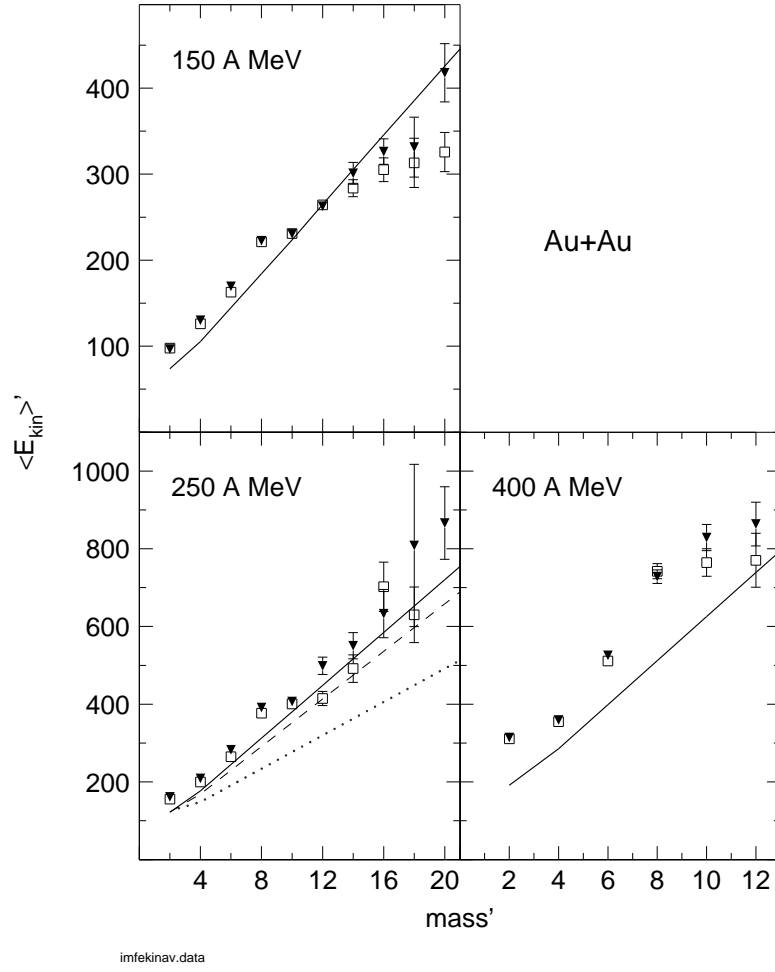


FIG.16 Average kinetic energies for hydrogen and helium isotopes at polar angles $60 - 90^\circ$. The data are from ref. [25]. The solid line represents the mass dependence inferred from the global fit of the blast model with velocity profile *WS2*.

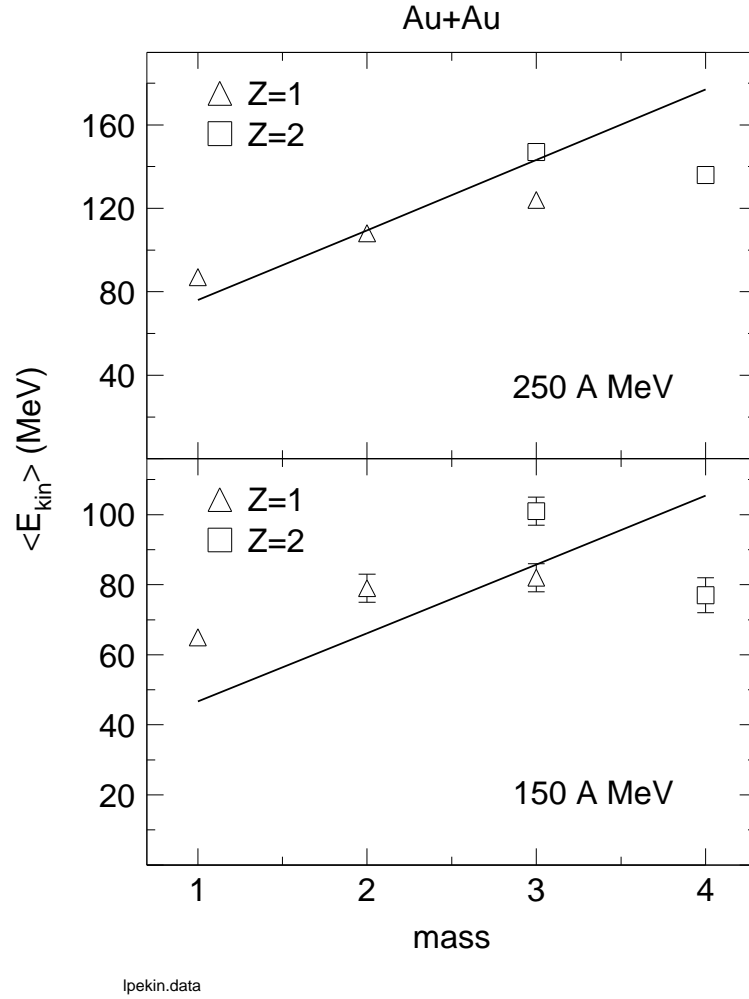


FIG.17 Variation of the deduced collectivity with increasingly dilute flow profiles.

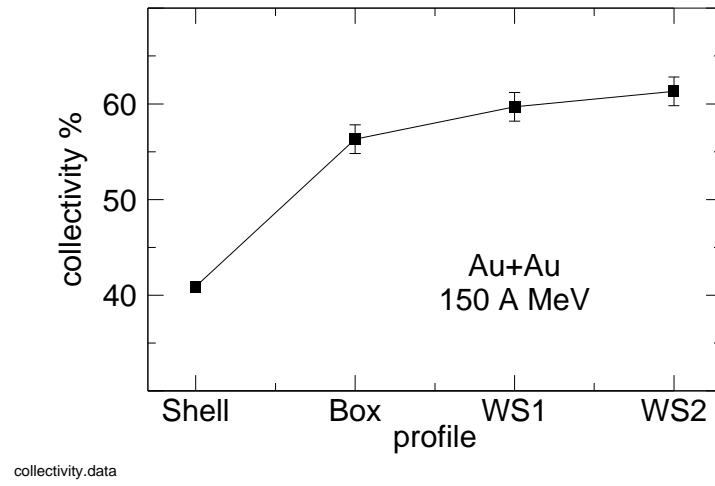
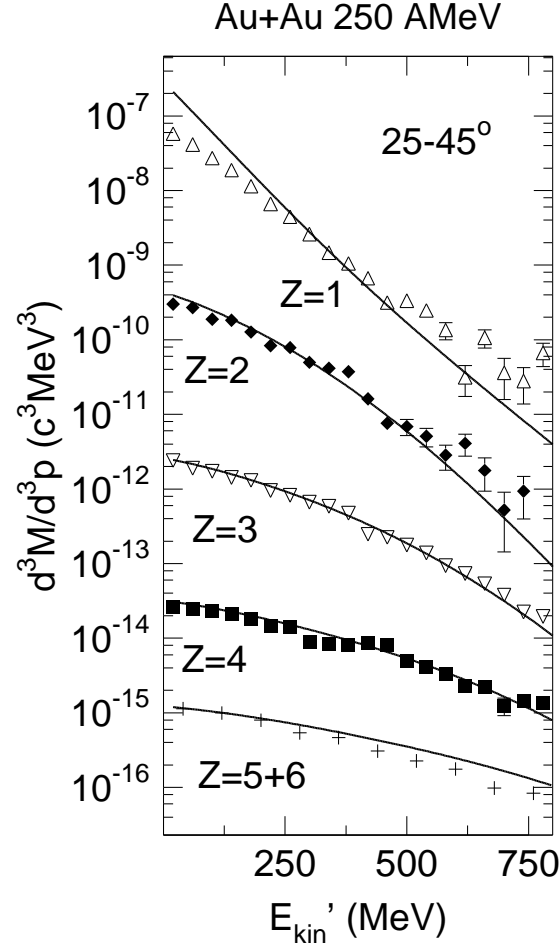
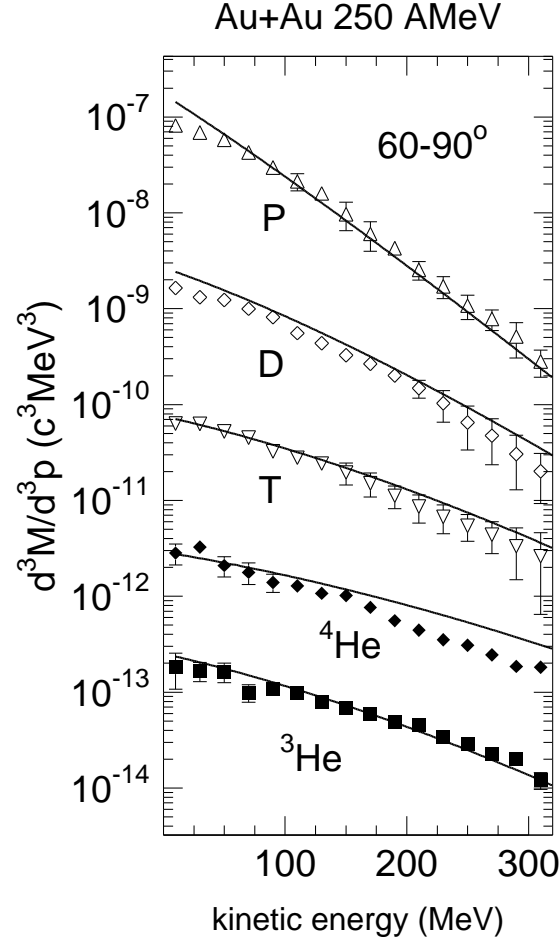


FIG.18 Kinetic energy spectra at center-of-mass polar angles $(25-45)^\circ$ for fragments with nuclear charge $Z=1, 2(\times 0.1), 3(\times 0.01), 4(\times 0.001),$ and $5+6(\times 0.0001)$. The system is Au+Au at 250 A MeV, the event sample is ERAT200D. The smooth curves are blast model descriptions.



imfekin250f.data

FIG.19 Kinetic energy spectra of light charged particles (indicated in the figure) at polar angles $(60 - 90)^\circ$ for Au on Au at 250 A MeV. The data (symbols) are from reference [30], the smooth curves are predictions of the blast model. The event sample is approximately ERAT200.



imfekin250p.data

FIG.20 Invariant transverse four-velocity spectra for Au on Au at 150 (left panels) and 400 A MeV for fragments with nuclear charges $Z=1, 2, 3$ and 4 (bottom to top). The spectra are shown for two indicated rapidity intervals. The data are represented by symbols, smooth curves were calculated with the blast model. The event sample is ERAT200D.

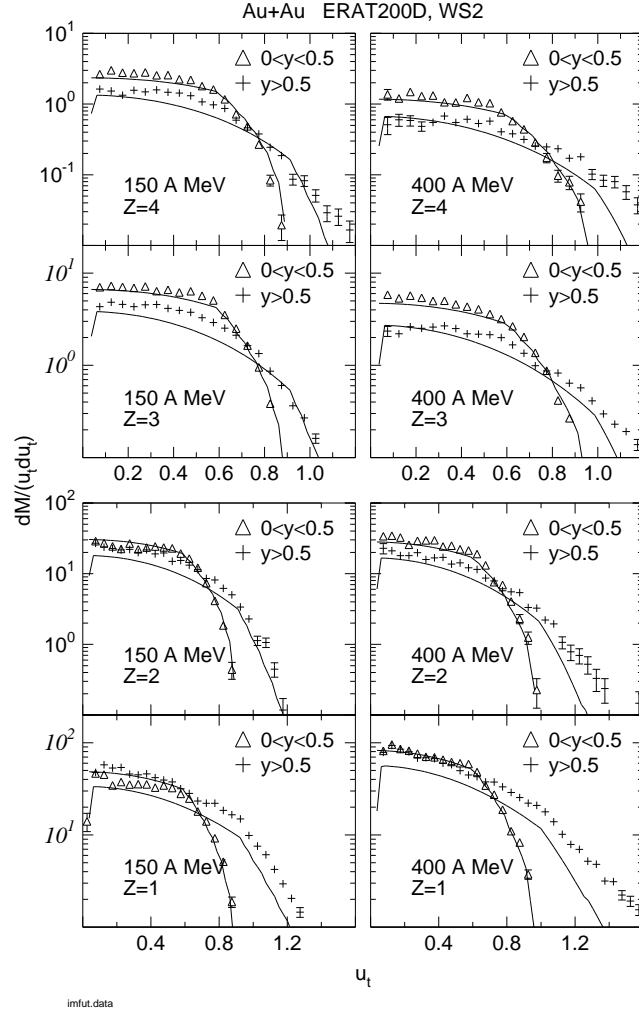


FIG.21 Polar angular distributions for Au on Au at 400 A MeV for fragments with nuclear charges $Z=1$ to 6. The smooth curves are blast model calculations. The deviations from a flat distribution in the model are due to the apparatus filter. The event sample is ERAT200D.

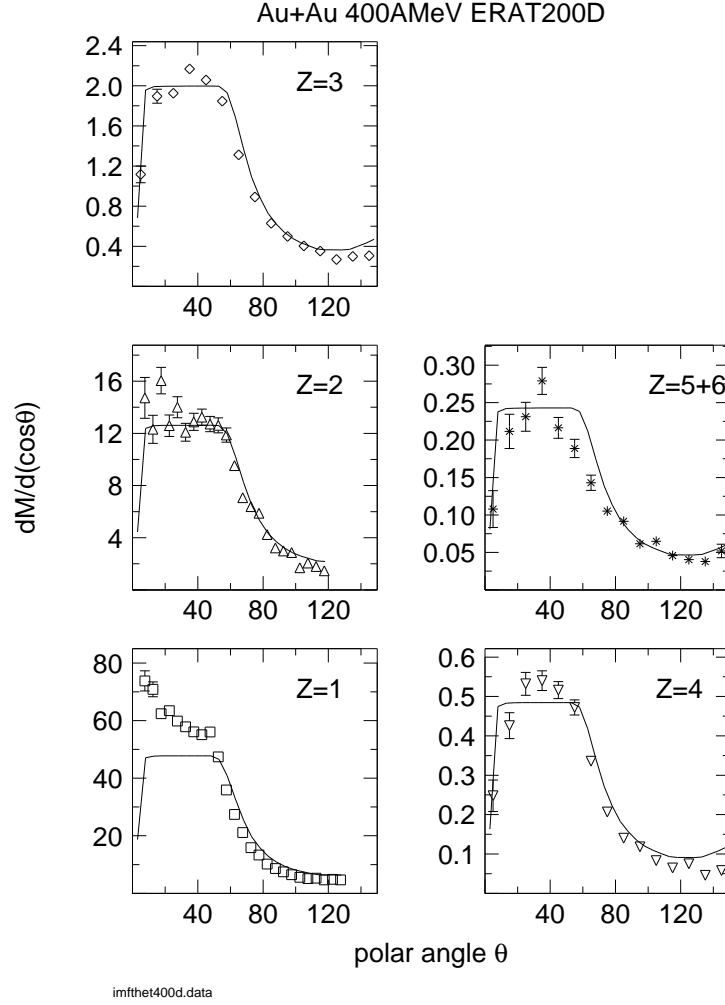


FIG.22 Polar angular distributions of intermediate mass fragments for Au on Au at 400 A MeV. A scaled four-velocity cut $u < 0.5$ is applied. The distributions are shown for various indicated event samples.

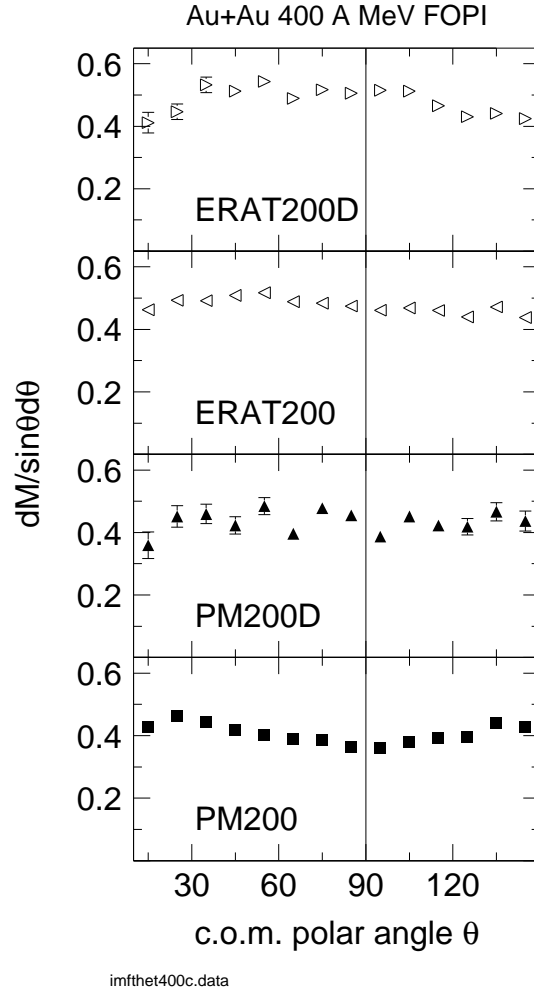
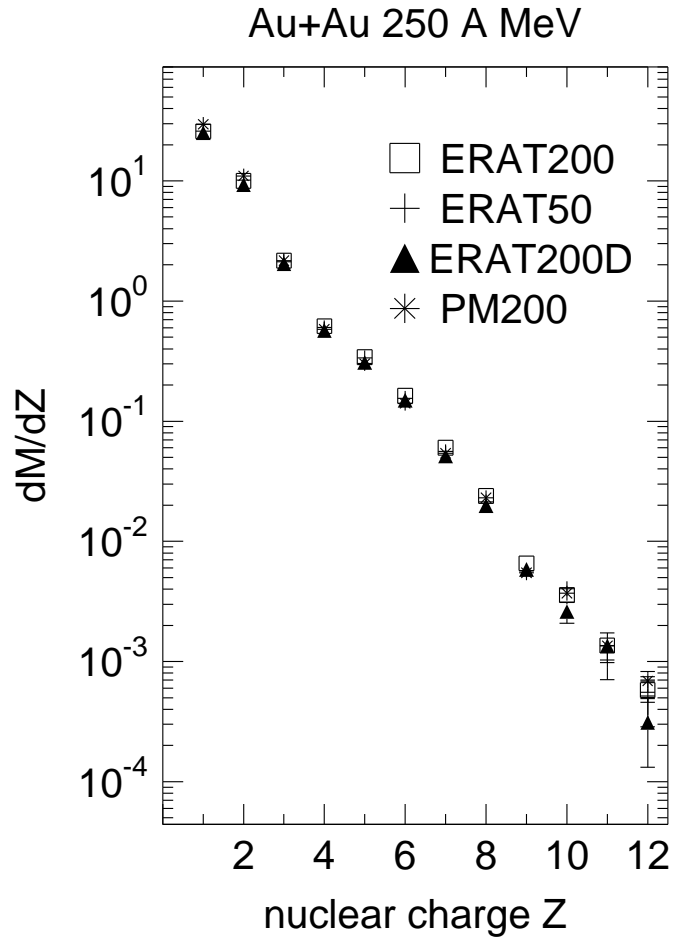
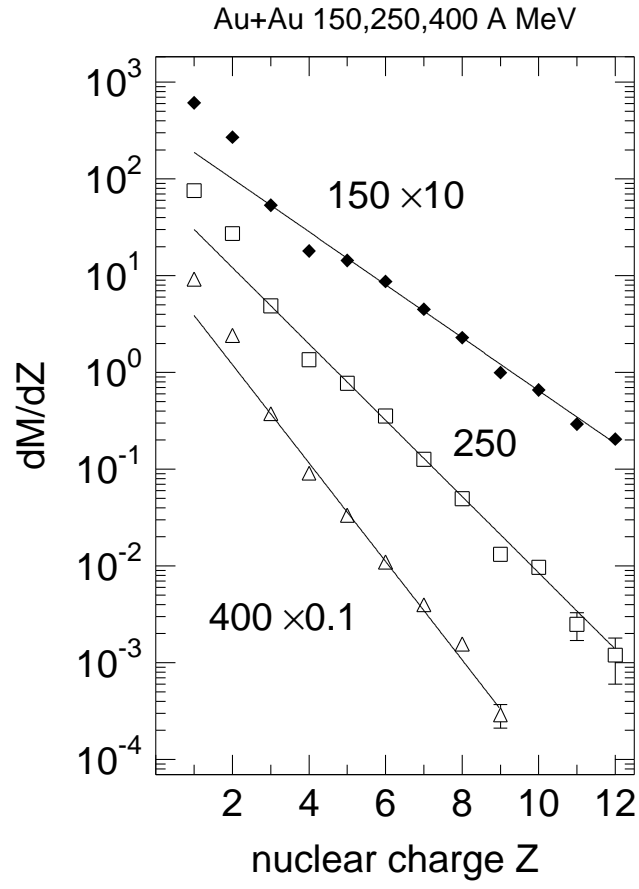


FIG.23 Measured multiplicities for Au on Au at 250 A MeV as function of nuclear charge for various event selections described in the text.



imfz250f.data

FIG.24 Measured 4π -integrated multiplicities for Au on Au at 150, 250 and 400 A MeV as function of nuclear charge. The straight lines are exponential fits excluding $Z=1, 2$ and 4 fragments.



imfzf.data

FIG.25 Clusterization in experiment (EXP) and theory (IQMD) versus incident energy. Left panel: IMF multiplicity in 4π geometry. Right panel: percent of protons bound in any cluster (left ordinate, EXP and IQMD) and protons bound in IMF's (right ordinate, triangles, EXP only). In both panels the height of the hatched area indicates the span when switching from soft (higher values) to hard EOS.

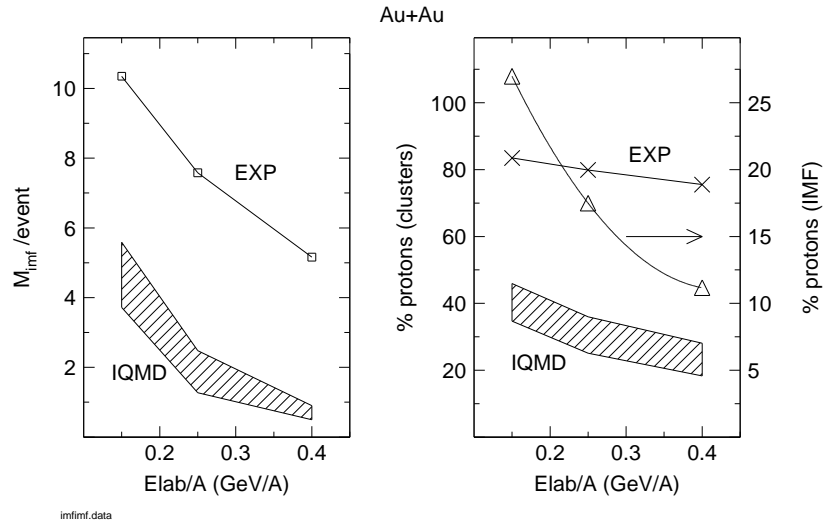


FIG.26 Fluctuations and correlations of multiplicities. The histograms are measurements, the crosses are blast model simulations. Lower left panel: External Wall multiplicity (M) distribution. Upper left panel: IMF multiplicity distribution. Lower right panel: average IMF multiplicity versus light-particle multiplicity.

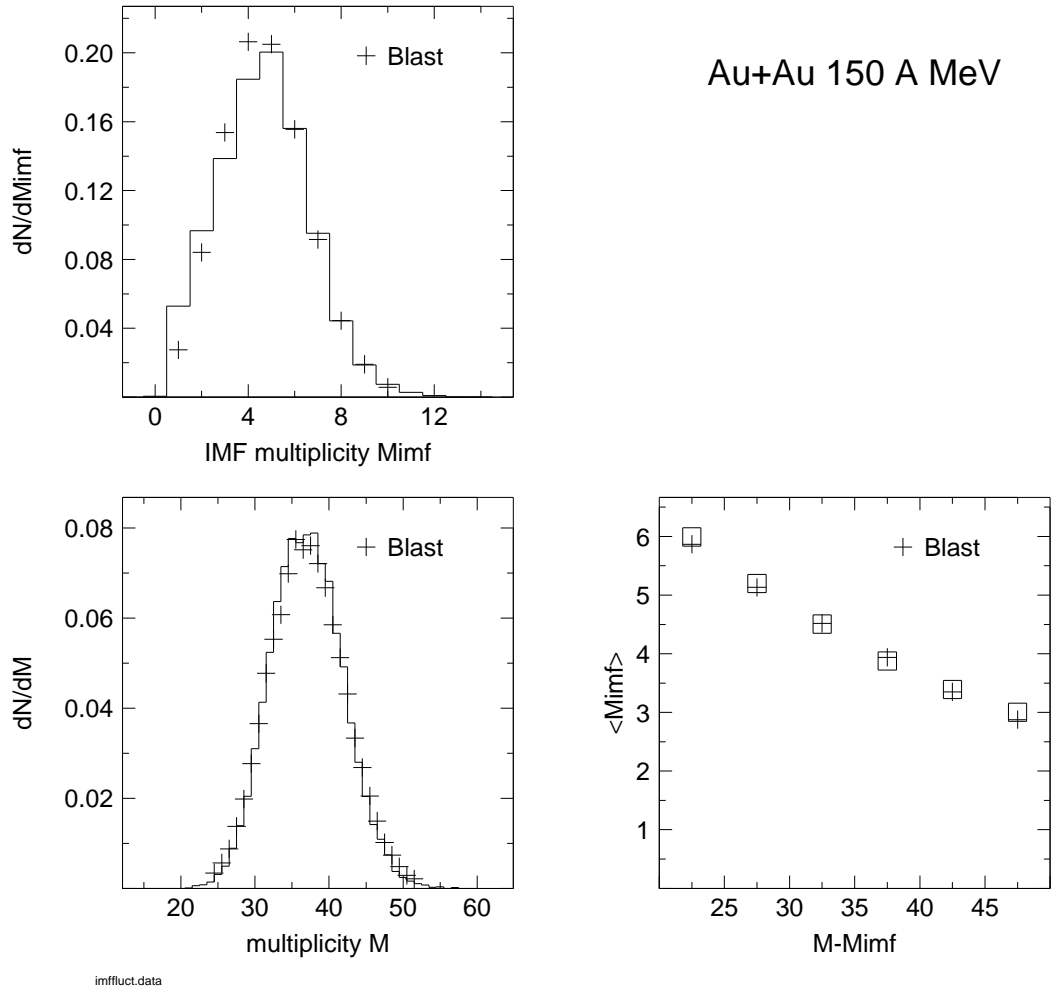


FIG.27 Comparison of measured (FOPI) charged particle multiplicities with calculations using three different statistical models, QSM, WIX, SMMM for three indicated incident energies. The predictions of IQMD (SM) are indicated as dashed lines. The upper right panel gives the ratio of measured oxygen yields to predictions of the QSM (triangles joined by solid lines). The dotted line in the panel is a calculation for the maximum collective energy allowed by the blast model fits.

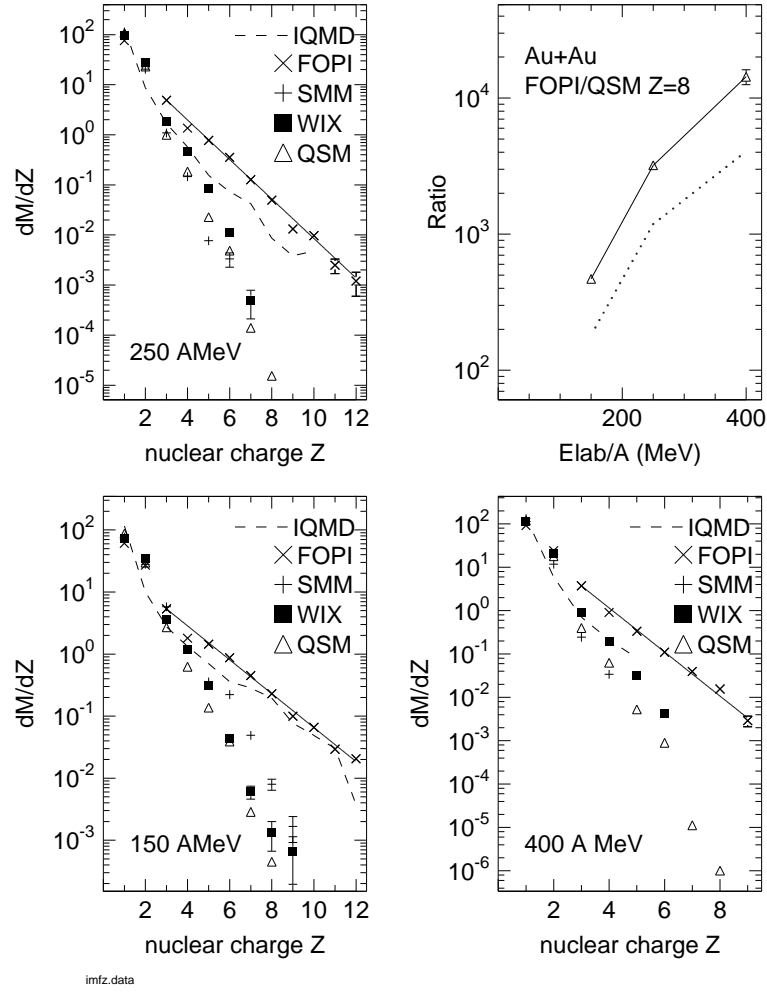


FIG.28 Left panel: measured (crosses) charged particle multiplicities at 250 A MeV (together with the exponential fit to guide the eye) and various calculations with the code WIX. Full squares: $C_{cut} = 2$, open squares: $C_{cut} = 8$, open circles: $C_{cut} = 8$ and no evaporation. Right panel: known level distribution for ^{16}O (histogram), left (right) arrow: average excitation energy of ^{16}O predicted by WIX for $C_{cut}=2$ (8).

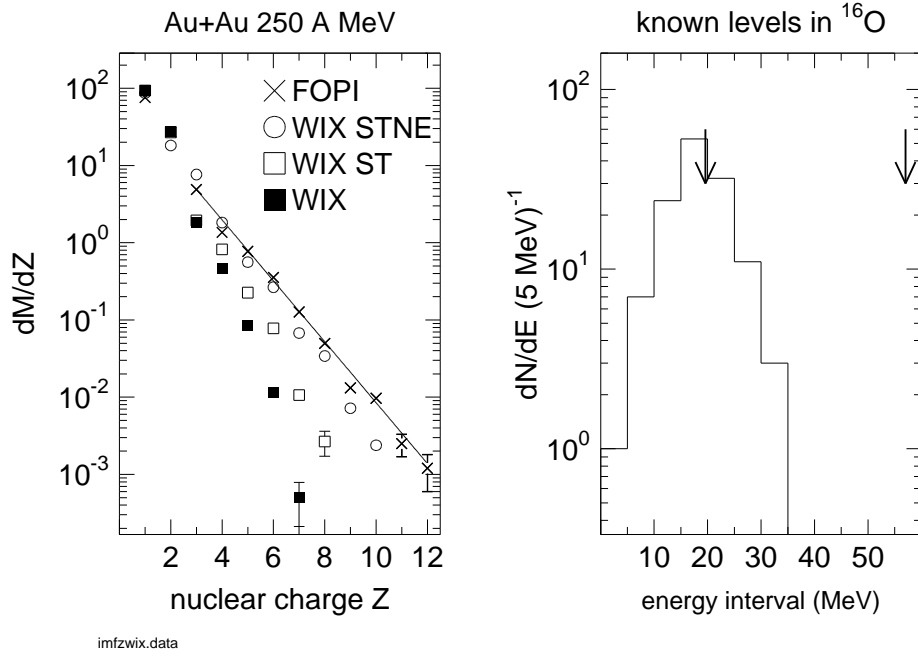
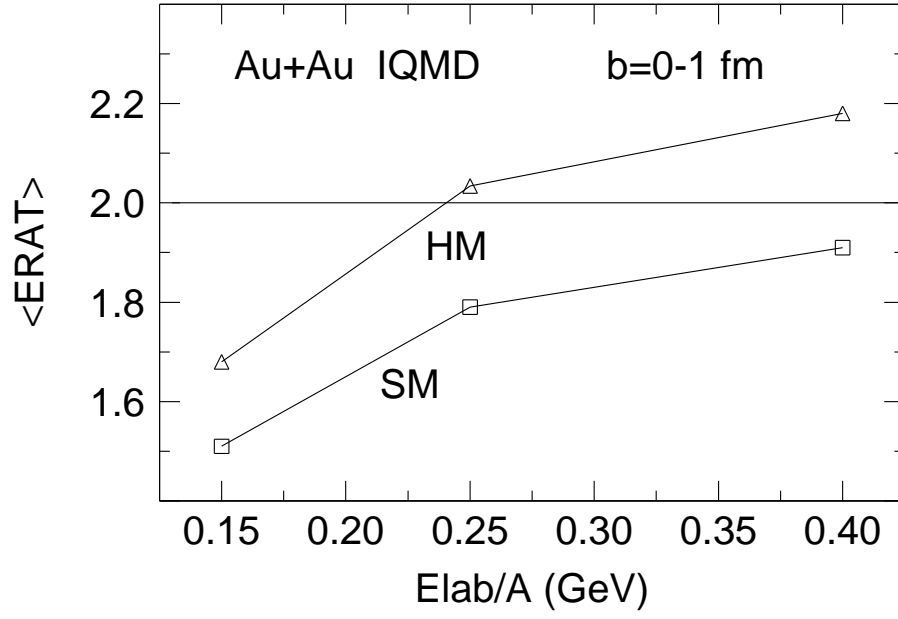
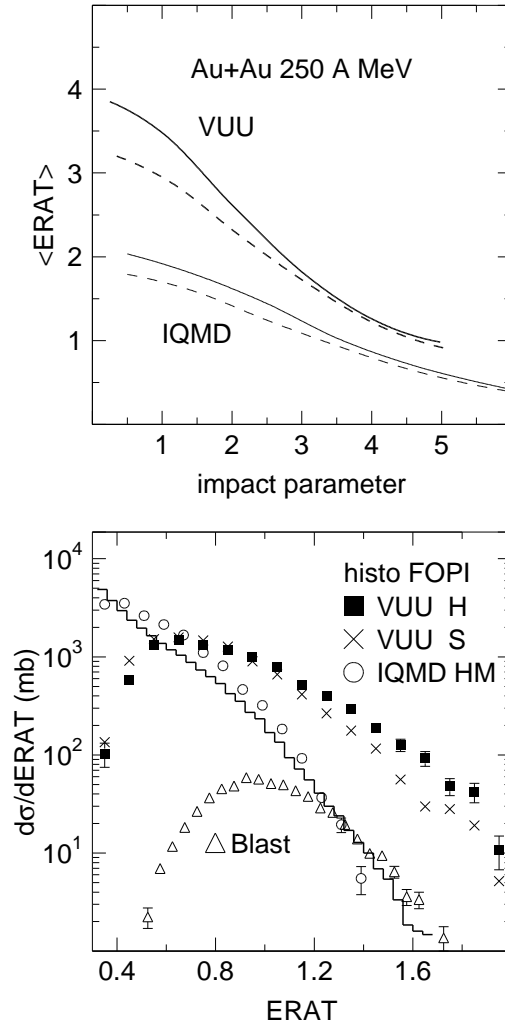


FIG.29 Variation of the average value of ERAT with incident energy in the IQMD model. The dependences are shown for the hard (HM) and the soft (SM) momentum dependent EOS. The Au on Au collisions are restricted to impact parameters < 1 fm. ERAT is calculated from charged particles only, but using full 4π geometry.



eratiqmd.data

FIG.30 ERAT for Au on Au at 250 A MeV. Top panel: predicted dependence on the impact parameter in 4π geometry, using charged particles only. Two different codes, VUU [71] and IQMD [54] were used. The solid (dashed) curves are for the hard (soft) EOS. Bottom panel: measured ERAT distribution (histogram) and filtered theoretical simulations. Triangles: Blast Model normalized to 31 mb ($b \leq 1\text{fm}$). Open circles: IQMD hard momentum dependent EOS. The other symbols are for the VUU calculation with hard (H) or soft (S) EOS.



erat250dan.data

FIG.31 Scaled sideflow in semicentral Au on Au collisions. Lower panel: filtered IQMD calculations for p_x^{dir} with the soft momentum-dependent EOS (SM) and for 400 A MeV incident energy. Solid curve: binning with the true impact parameter. Squares: binning with ERAT. Dotted: binning with PM. Crosses: binning with ERAT, but for 150 A MeV incident energy. Middle panel: FOPI data for p_x^{dir} binned with ERAT and for the three indicated energies. Upper panel: same as middle panel, but for the alternate sideflow observable F_{DO} .

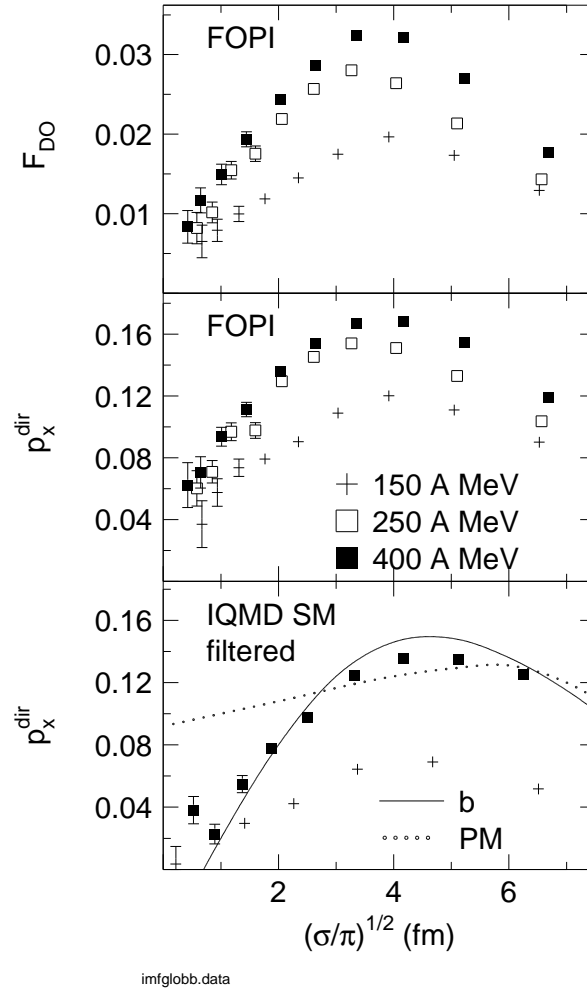
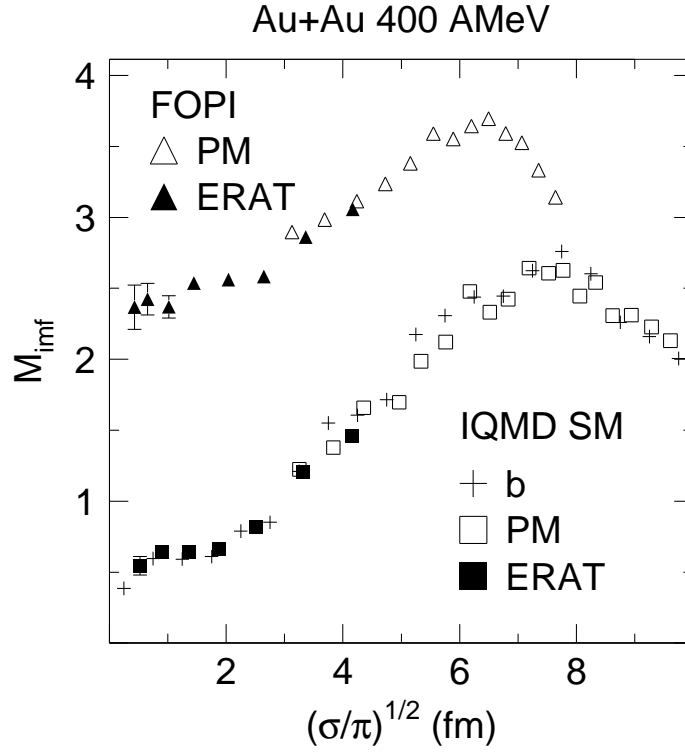


FIG.32 Comparison of the centrality dependence of the IMF multiplicity in experiment (triangles) and theory. Open symbols: multiplicity binning, closed symbols: ERAT binning, crosses: impact parameter binning.



qmdglob400.data

FIG.33 Equation of state and impact parameter dependence of the degree of clusterization in the IQMD simulation. Lower panel: IMF multiplicity, upper panel: He/H ratio. S (H) stands for soft (hard) EOS, M indicates inclusion of momentum dependence. The curves are to guide the eye. For comparison, the experimental He/H ratio for central collisions is 0.26. All data are for Au on Au at 400 A MeV.

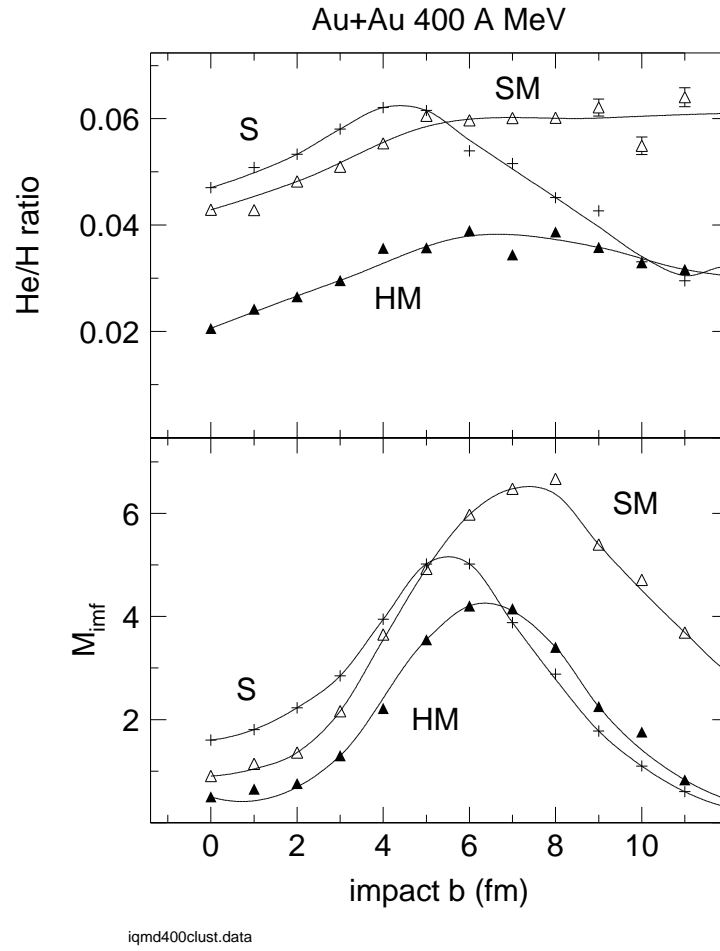


FIG.34 IQMD predictions (soft momentum dependent EOS) for average kinetic energies as function of mass. The straight lines are linear least squares fits in the mass range $A = 1 - 10$. The simulations are for Au on Au collisions at 150 (left) and 400 (right) A MeV with impact parameters up to 1 fm and for particles emitted with polar angles $45 - 135^\circ$.

